

CHAPTER-III

Section A

Copper Borate (CuB₄O₇) catalyzed multi-component green synthesis of 2,4,5 Tri-aryl imidazole derivatives

3.A.1 Background of the present investigation

Recent trend in synthetic organic chemistry research focuses on the design and development of the reaction methodology in an environmentally benign greener and sustainable way to reduce the use of the hazardous chemicals and to explore the alternative reaction conditions or reaction media to bring about the desired chemical transformations by minimizing the by-products or waste and exclusion of the conventional organic solvents¹⁻¹⁰. Multi-Component Reactions (MCRs) serve as a good example to meet the requirements for the green chemical processes and it may be viewed as an art of performing efficient chemical transformation by coupling three or more reactants in a single pot in single operation avoiding toxic reagents, solvents and expensive purification techniques. MCRs also have an advantage in the development of novel and cost-effective approaches in synthetic chemistry research leading to environmental protection and have emerged as powerful tools for drug discovery¹¹⁻¹⁵. The Multi-Component Reaction technique has gained special attention and drawn great interest in modern synthetic chemistry and pharmaceutical chemistry because one pot Multi-Component Reactions (MCRs) has many advantages such as high atom-economy, high selectivity, operational simplicity, structural diversity, short reaction time, low cost, low energy consumption, high yield and easy purification process¹⁶⁻²⁰. Among many Nitrogen containing heterocyclic compounds, imidazole scaffold is an important heterocyclic scaffold due to their richness in various natural products and their widespread use in the medicinal field²¹⁻²². Imidazole ring system possesses variety of pharmaceutical properties and plays a fundamental role in numerous biochemical processes²³. Over the past few years, highly substituted imidazole has gained a lot of interest due to their biological relevance in many natural products and their extensive applications in the area of material science²⁴ and their potential use as herbicide²⁵, fungicide²⁶, inhibitors of P38 MAP kinase²⁷, B-Rafkinase²⁸, anti-inflammatory²⁹, anti-tumor³⁰, and anti-thrombotic³¹agents. In addition, some of the highly substituted imidazole compounds serve as a photosensitive material in photography³². Highly substituted imidazoles such as clemizole (antihistaminic agent)³³ (94), nocodazole (antinematodal)³⁴ (95), azathioprine (anti-rheumatoid arthritis)³⁵ (96), dacarbazine (anticancer)³⁶⁻³⁷ (97) are commercially available drugs for the treatment of different diseases (Fig.3.1).

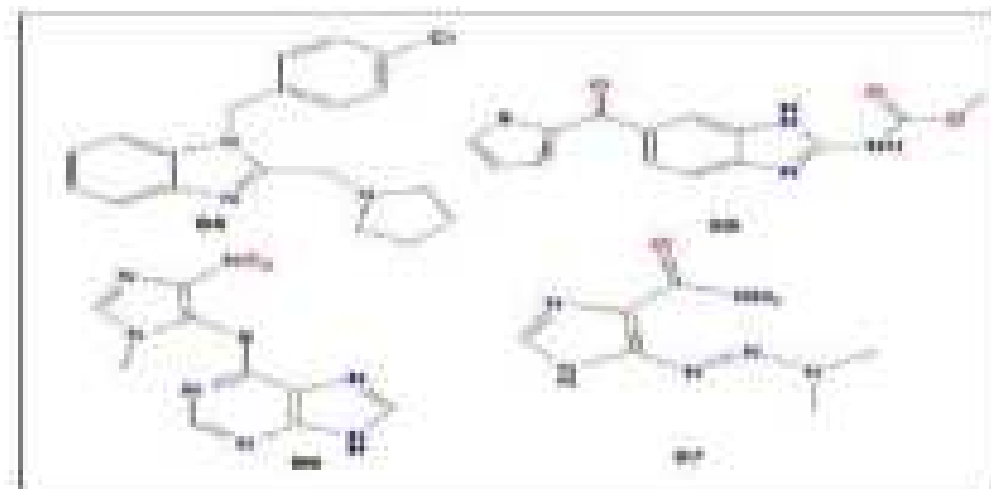
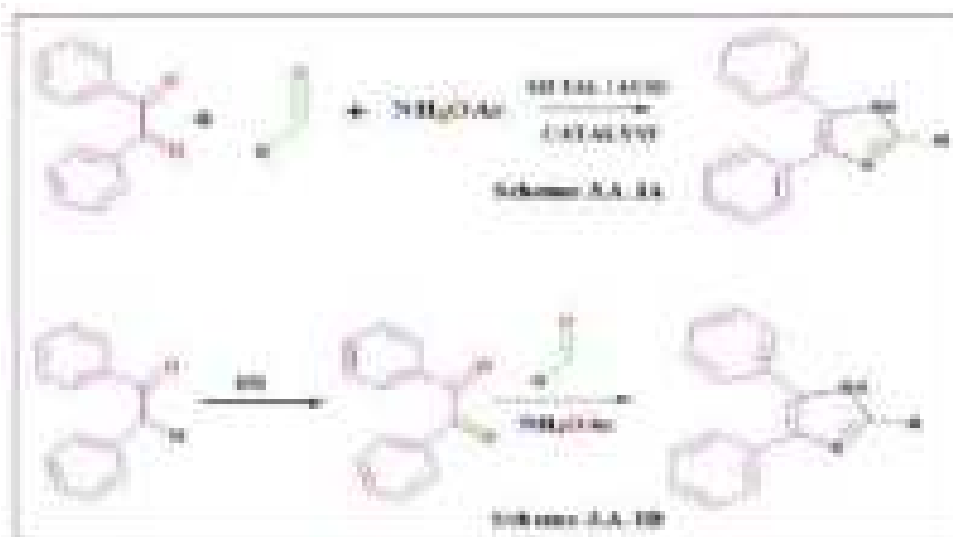


Fig. 3.A.1. Structures of commercially available drugs containing imidazole core

In view of the diverse properties and applications of imidazole core, numerous synthetic methodologies have been formulated using various catalytic systems under different reaction conditions for the efficient and rapid synthesis of substituted imidazole derivatives by three-component cyclocondensation of a 1,2-diketone, α -hydroxyketone or α -ketomoxime with an aldehyde and ammonium acetate³⁸⁻⁵⁰ (Scheme 3.A.1A). Apart from the conventional use of 1, 2-diketone, α -hydroxyketone or α -ketomoxime, several reports on the synthesis of substituted imidazoles have been documented using α -methylene ketone⁵¹⁻⁵² (Scheme 3.A.1B).

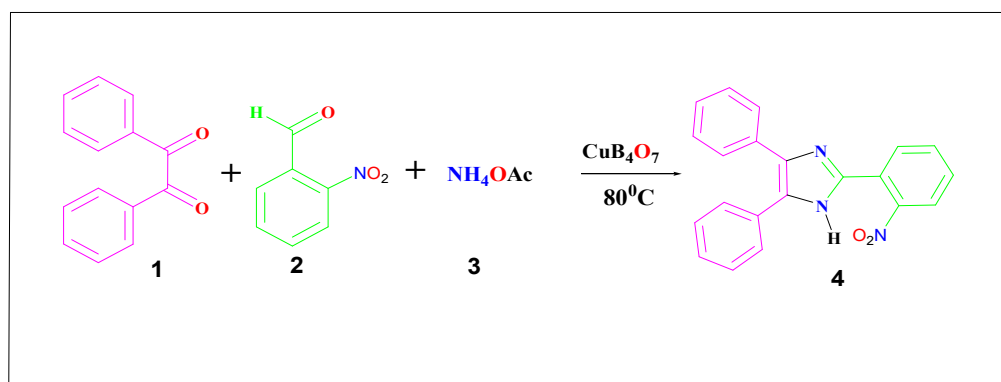


Scheme. 3.A.1A. Debus-Radziszewski imidazole synthesis and **Scheme. 3.A.1B.** Synthesis of tri-substituted imidazole using α -hydroxyketone.

Although, these documented procedures offer several beneficial features, yet most of them have serious drawbacks such as use of expensive catalyst, lower yield, use of the toxic solvent, harsh reaction condition, longer reaction time and tedious work-up procedures⁵³⁻⁵⁶. All these facts have encouraged us to find an eco-friendly, environmentally benign greener and sustainable method for the synthesis of substituted imidazole and stimulated us to employ copper (II)borate (CuB_4O_7) as a catalyst for the one-pot three-component synthesis of 2, 4, 5 triarylimidazole derivatives by condensation of benzil, NH_4OAc and aromatic aldehydes in solvent free condition.

3.A.2 Results and discussion

Interestingly, there are several reports on the synthesis of 2, 4, 5 tri-substituted imidazole using different copper salts as a catalyst⁵⁷⁻⁶¹ but there are no reports on the study of catalytic activities of copper borate (CuB_4O_7) so far. While going through the literature review for the organic transformation reactions catalyzed by transition metal salts, our research group encountered that there are no reports on the catalytic activities of transition metal borates for such reactions. Therefore, it was thought worthwhile to explore the catalytic efficiency of copper (II) borate salt (CuB_4O_7) for the green synthesis of 2, 4, 5- triaryl imidazole derivatives. Initially, for a model reaction, we screened Benzil (1), 2 Nitrobenzaldehyde (2) and NH_4OAc (3) as model compounds in different environmentally friendly conditions at 80°C (Scheme 3.A.2) for 2 hours using different mol % (0.5, 1.0, 1.5, 2.0, 2.5, 3.0) of copper borate catalyst to synthesize 2, 4, 5 tri-substituted imidazole (4).



Scheme. 3.A.2. Model reaction for the synthesis of 2,4,5 triaryl imidazole, Benzil (1) 1mmol, 2-Nitrobenzaldehyde (2) 1mmol and NH_4OAc (3) 2.5 mmol.

We screened the catalytic efficiency of the studied catalyst with the model reactants in different solvents under different reaction conditions and the result is summarized in table 3.1. We found that in more polar solvents like alcohol and DMF, the yield of the products were good (Table 3.A.1, entry 1, 2, 3) but the

reaction needed more time (2 hour) to go for completion. Due to this drawback, we focused our study on the solid phase synthesis using silica gel as a reaction medium but in this case also we encountered problems during work-up of the desired product.

Table 3.A.1. Screening of the solvent for model reaction

Entry	Solvent ^a	Yield % ^b
1	Ethanol	84
2	Methanol	80
3	DMF	88
4	DMSO	82
5	Water	32
6	Silica gel	85
7	Neat	96

^aThe reaction was performed with benzil 1 (1mmol), 2-nitrobenzaldehyde 2 (1mmol) and ammonium acetate 3 (2.5mmol) and a catalyst under different solvent. ^b isolated yields

Therefore, these drawbacks prompted us to carry out the desired reaction in neat condition without using any organic solvents. The results of the model reaction for different mol% of catalyst loading under optimized condition are summarized in Table 3.A.2. Encouragingly, the desired product 2, 4, 5 triaryl imidazole (4) was obtained in satisfactory yield in less time (8-10 minutes) at 80 °C and the maximum yield was obtained for 2 mol% of the catalyst loading (Table 3.A.2, entry 5).

Table 3.A.2. Screening of the amount of the catalyst for the model reaction

Entry	Catalyst mol % ^a	Temperature (°C)	Time (Mins)	Yield ^b (%)
1	0	80	10	20
2	0.5	80	10	70
3	1.0	80	10	76
4	1.5	80	10	85
5	2	80	10	96
6	2.5	80	10	96
7	3.0	80	10	95

^aThe reaction was performed with benzil 1 (1mmol), 2-nitrobenzaldehyde 2 (1mmol) and ammonium acetate 3 (2.5mmol) and a catalyst under different solvent at 80 °C with different mol% of the catalyst. ^b isolated yields.

Also, we observed that the yield of the product is maximum when the ratio of amount of NH₄OAc is 2.5 mmol with respect to other substrate and with decrease or increase in the amount of NH₄OAc, the yield of the product (4) decreases. A control experiment without catalyst has showed a low overall yield of products (Table 3.A.2 entry 1). Moreover, having recognized the optimized reaction condition, we subsequently, examined the catalytic efficiency and applicability of this protocol by extending this protocol to other substituted benzaldehydes and other aromatic aldehydes to prepare 2, 4, 5-triaryl imidazole derivatives (Fig 3.A.2) and we observed that all the reactions proceeded smoothly in very short reaction time to afford the desired imidazoles (4a-4w) in good to excellent yields (88-98%) (Table 3.A.3).

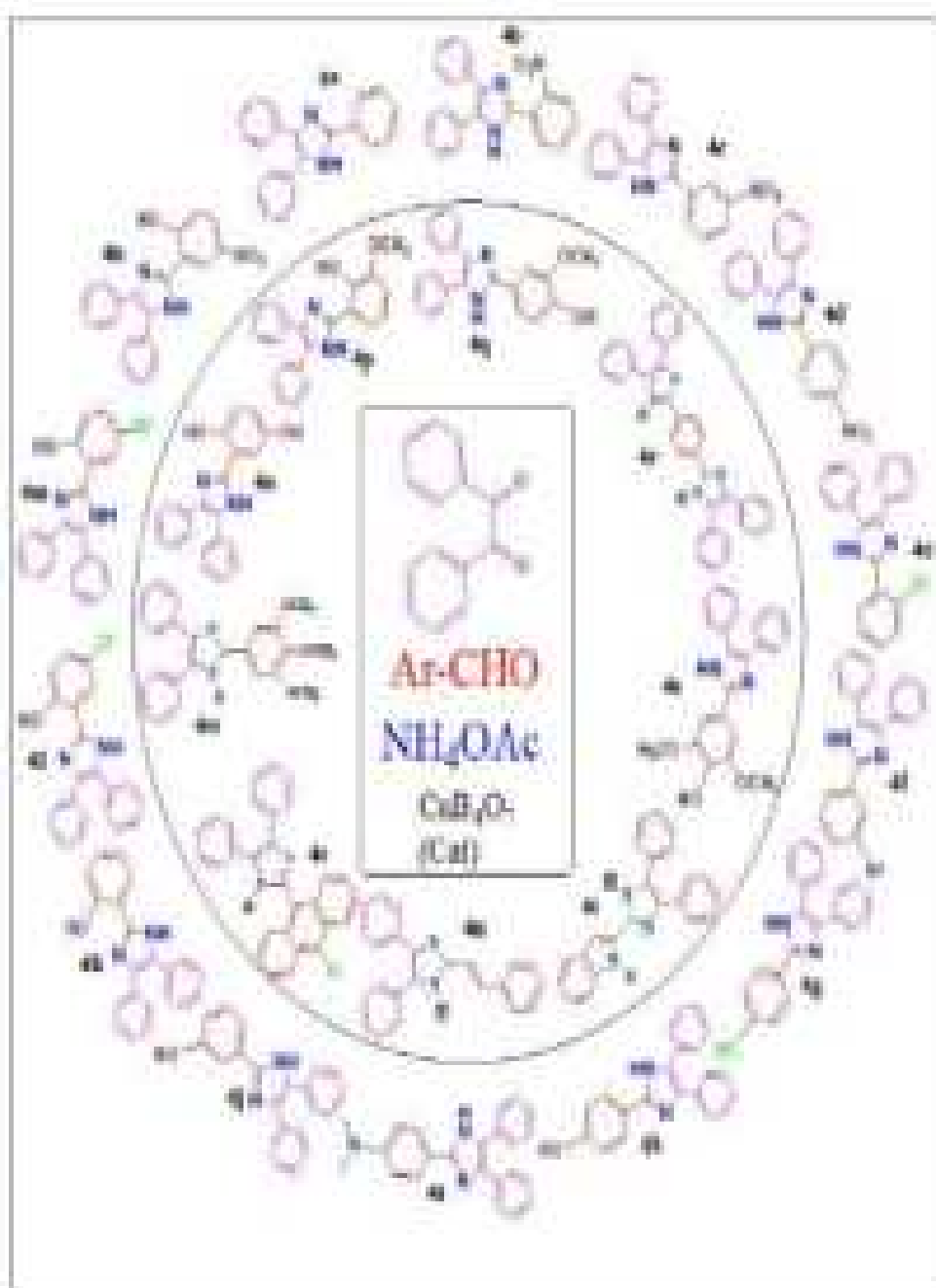


Fig. 3.A.2. 2, 4, 5 triaryl imidazole derivatives (4a-4w)

Table. 3.A.3. CuB₄O₇ catalyzed solvent free synthesis of 2,4,5-triarylimidazole derivatives (4a-4w)

Entry	1,2 diketone	Aldehyde substrate	product	Yield(%) ^b
1	Benzil	Benzaldehyde	4a	98
2	Benzil	2-nitrobenzaldehyde	4b	96
3	Benzil	3-nitrobenzaldehyde	4c	95
4	Benzil	4-nitrobenzaldehyde	4d	97
5	Benzil	2-Chlorobenzaldehyde	4e	96
6	Benzil	3-bromobenzaldehyde	4f	93
7	Benzil	4-cyanobenzaldehyde	4g	95
8	Benzil	4-hydroxybenzaldehyde	4h	89
9	Benzil	4-N, N-dimethylbenzaldehyde	4i	97
10	Benzil	3-hydroxybenzaldehyde	4j	98
11	Benzil	2-hydroxybenzaldehyde	4k	97
12	Benzil	5-chloro 2-hydroxybenzaldehyde	4l	94
13	Benzil	5-bromo 2-hydroxybenzaldehyde	4m	96
14	Benzil	5-nitro 2-hydroxybenzaldehyde	4n	96
15	Benzil	2,4-dihydroxybenzaldehyde	4o	97
16	Benzil	2-hydroxy-3-methoxybenzaldehyde	4p	95
17	Benzil	4-Hydroxy-3-methoxybenzaldehyde	4q	94
18	Benzil	Benzene-1,4-dicarboxaldehyde	4r	86
19	Benzil	4-Hydroxy-3,5- dimethoxybenzaldehyde	4s	94
20	Benzil	Indole-2-carboxaldehyde	4t	96
21	Benzil	Cinnamaldehyde	4u	92
22	Benzil	10-Chloro-9-anthraldehyde	4v	93
23	Benzil	3,4,5-trimethoxybenzaldehyde	4w	98

^bisolated yield

It was observed that para substituted benzaldehyde with electron withdrawing group successfully afforded the corresponding imidazoles in excellent yield under optimized condition compared to the Para substituent benzaldehyde with electron releasing group. Ortho substituent benzaldehyde and other aromatic aldehydes also afforded the corresponding imidazoles in good yield but they

Table. 3.A.4. Comparison of Catalytic efficacy of CuB₄O₇ with other reported Catalysts:

Entry	Catalyst	Solvent ^a	Temperature	Time	Yield (%) ^b
1	L-Proline	MeOH	60 °C	9 Hours	90 [lit ⁶²]
2	Zeolite ZSM-11	Neat	Reflux	60 Minutes	80 [lit ⁶³]
3	Zr(acac) ₄	EtOH	Reflux	2.5 Hours	90 [lit ⁶⁴]
4	Yb(OTf) ₃	OHAc	70 °C	2 Hours	92 [lit ⁶⁵]
5	ZnO Nano rod	H ₂ O	Reflux	1.45 Hours	83 [lit ⁶⁶]
6	I ₂	Neat	RT	15 Minutes	90 [lit ⁶⁷]
7	Fe ₃ O ₄ nano particle	Neat	80 °C	20 Minutes	96 [lit ⁶⁸]
8	Nano TiCl ₄ .SiO ₂	Neat	110 °C	1 Hour	90 [lit ⁶⁹]
9	Nano MgO	Neat	100 °C	0.6 Hours	94 [lit ⁷⁰]
10	InF ₃	Neat	60 °C	0.3 Hours	90 [lit ⁵⁰]
11	CoFe ₂ O ₄ Nps	EtOH	40 °C	20 Minutes	95 [lit ⁷¹]
12	Y(TFA) ₃	Neat	100 °C	3 Hours	97 [lit ⁷²]
13	Boric Acid	H ₂ O	Ultrasound	30 Minutes	98 [lit ⁷³]
14	ZSM-5-SO ₃ H	Neat	110 °C	90 Minutes	90 [lit ⁷⁴]
15	Trichloro melamine	Neat	110 °C	1 Hour	92 [lit ⁷⁵]
16	TiO ₂	Neat	120 °C	2.5 Hours	92 [lit ⁷⁶]
17	H ₂ SO ₄ .SiO ₂	Neat	110 °C	60 Minutes	94 [lit ⁷⁷]
18	Copper Nano particles	Neat	RT	60 Minutes	94 [lit ⁷⁸]
19	HMDS	Neat	120 °C	3 Hours	96 [lit ⁷⁹]

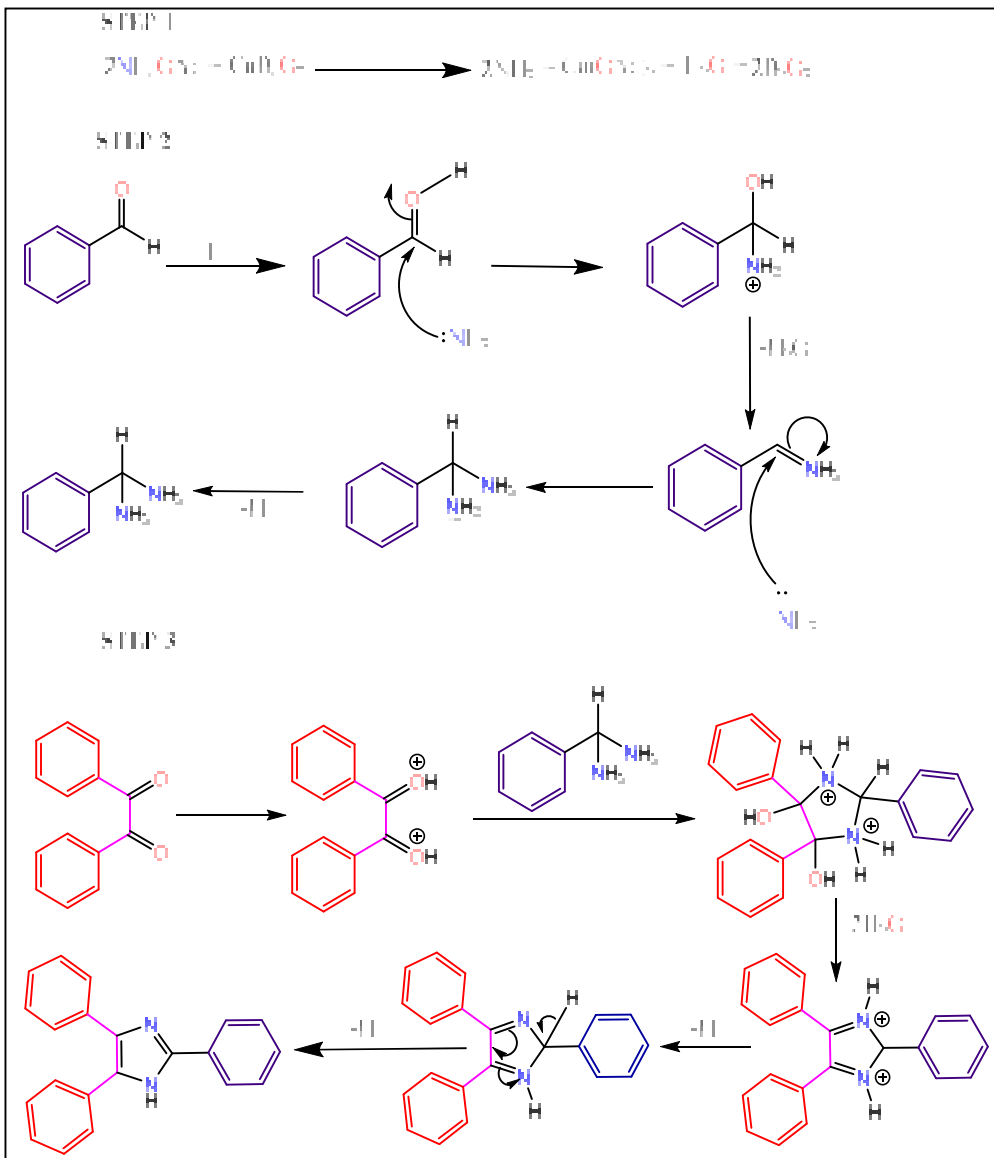
20	KMnO ₄ /CuSO ₄	EtOH	Reflux	70 Minutes	85 [lit ⁵⁷]
21	SiO ₂ -NaHSO ₄	Neat	120 °C	30 Minutes	95 [lit ⁸⁰]
22	Zeolite HY/ Silica Gel	Neat	M.W	6 Minutes	89 [lit ⁸¹]
23	CuB₄O₇ [this work]	Neat	80 °C	10 minutes	98

^aComparison of catalytic efficacy of CuB₄O₇ with other reported catalyst for the synthesis of 2,4,5-triaryl-imidazole derivatives using benzil, aromatic aldehyde and ammonium acetate under different reaction conditions. ^b isolated yields.

required more time for the reaction to complete. Also, we compared the catalytic efficiency of CuB₄O₇ for the synthesis of 2,4,5-triarylimidazole derivatives with other reported catalyst and we observed that CuB₄O₇ has high catalytic efficiency and need less reaction time for the reaction to go for completion. The comparative data of CuB₄O₇ with other reported catalyst is listed in Table 3.A.3.

3.A.3 Plausible Mechanism

A proposed mechanism for the synthesis of 2,4,5-triarylimidazole catalyzed by CuB_4O_7 is depicted below in Scheme 3.A.3.



Scheme. 3.A.3. Proposed mechanism for the synthesis of 2,4,5 - triarylimidazole

3.A.4 Experimental section:

3.A.4.1 Materials:

All starting materials of high-purity for the aforementioned synthesis were purchased commercially and were used as received. The FT-IR spectra of the prepared compound were recorded in Bruker Alpha III spectrophotometer operating in the wave number region 4000 to 400 cm^{-1} in dry KBr. The melting point of the synthesized compounds was determined by open capillary method. ^1H -NMR spectra of the synthesized tri-aryl imidazole derivatives were recorded at room temperature on a FT-NMR (Bruker Advance-II 400 MHz) spectrometer by using $\text{DMSO-}d_6$ as solvents and chemical shifts are quoted in ppm downfield of internal standard tetramethylsilane (TMS).

3.A.4.2 General procedure for synthesis of 2, 4, 5-tri-aryl imidazole:

In a typical procedure a mixture of benzil (1.0 mmol), substituted benzaldehyde (1.0 mmol), ammonium acetate (2.5 mmol), copper borate (2 mol %) thoroughly ground and mixed in a mortar and pestle to make a homogenous mixture. The mixture was then transferred to a test tube. The reaction was heated at 80°C for 10 minutes. The progress of the reaction was monitored by TLC using hexane/ethyl acetate (80:20) solvent. After completion of the reaction, the reaction mixture was dissolved in methanol and filtered. The filtrate was evaporated under vacuum and subsequently dried to afford desired product. All the synthesized compounds (4a-4w) were recrystallized from ethanol and have been characterized by their analytical (yield and melting point) and spectroscopic data (FT-IR and ^1H NMR) and compared with the literature value.

3.A.5 Conclusion

Herein, we have successfully developed a simple, environmentally benign and efficient green methodology for a synthesis of 2, 4, 5-triarylimidazole derivatives using unconventional CuB_4O_7 as a catalyst utilizing one pot three component reaction. This environmentally green approach provides access to substituted imidazole derivatives in good to excellent yield using an unconventional and inexpensive CuB_4O_7 catalyst. The developed catalytic procedure was found to be operative for a wide range of the aromatic aldehyde substrates.

3.A.6 Analytical and Spectroscopic data:

3.A.6.1 2,4,5-triphenyl-1H-imidazole (4a): White solid, yield=98%, melting point found (°C)=273-275, IR (KBr, cm^{-1}) ν_{max} : 3453 (NH), 1636 (C=C), 1503(C=N), ^1H NMR (400 MHz, DMSO- d_6): δ_{ppm} = 12.69 (s,1H, NH), 7.22 -7.55 (m, Ar H, 13H), 8.09 (d, 2H) J = 7.2 Hz.

3.A.6.2 2-(2-nitrophenyl)-4,5-diphenyl-1H-imidazole (4b): pale yellow solid, yield=96%, melting point (°C)=231-233, IR (KBr, cm^{-1}) ν_{max} : 3444(NH), 1619(C=C), 1602(C=N), ^1H NMR (400 MHz, DMSO- d_6): δ_{ppm} = 12.98 (s,1H, NH), 7.21 -7.97 (m, Ar H, 12H), 8.01 (d, 2H) J = 8.0 Hz.

3.A.6.3 2-(3-nitrophenyl)-4,5-diphenyl-1H-imidazole (4c): pale yellow solid, yield=95%, melting point (°C)=316-318, IR (KBr, cm^{-1}) ν_{max} =3443(NH), 3056-3026 (Aromatic C-H) 1660(C=C), 1598(C=N), ^1H NMR (400 MHz, DMSO- d_6): δ_{ppm} = 12.56 (s,1H, NH), 7.61 -8.37 (m, , 12H, Ar H), 8.62-8.68 (d, 2H, Ar H).

3.A.6.4 2-(4-nitrophenyl)-4,5-diphenyl-1H-imidazole (4d): yellow solid, yield: 97%, melting point (°C)= 235-237, IR (KBr, cm^{-1}) ν_{max} =3422 (NH), 3057 (Aromatic C-H),1660 (C=C), 1600 (C=N), ^1H NMR (400 MHz, DMSO- d_6): δ_{ppm} = 12.60 (s,1H, NH), 7.24- 8.45 (m, Ar H, 14H).

3.A.6.5 2-(2-chlorophenyl)-4,5-diphenyl-1H-imidazole (4e): off white solid, yield: 96%, melting point (°C)= 194-196, IR (KBr, cm^{-1}) ν_{max} =3426(NH), 3060(Aromatic C-H), 1665 (C=C), 1602(C=N), ^1H NMR (400 MHz, DMSO- d_6): δ_{ppm} = 12.66 (s,1H, NH), 7.21 -7.93 (m, Ar H, 14H).

3.A.6.6 2-(3-bromophenyl)-4,5-diphenyl-1H-imidazole (4f): Off white solid, yield=93%, melting point (°C)= 290-293, IR (KBr, cm^{-1}) ν_{max} =3451(NH), 3062, 3027 (Aromatic C-H),1694 (C=C), 1601(C=N), ^1H NMR (400 MHz, DMSO- d_6): δ_{ppm} = 12.83 (s,1H, NH), 8.30 (s, Ar H, 1H), 7.24-8.10 (m, Ar H, 13H)

3.A.6.7 4-(4,5-diphenyl-1H-imidazol-2-yl)benzotrile(4g): White solid, yield: 95%, melting point (°C)=186-188, IR (KBr, cm^{-1}) ν_{max} =3449 (NH), 3081, 3053 (Aromatic C-H), 1636 (C=C), 1610(C=N), ^1H NMR (400 MHz, DMSO- d_6): δ_{ppm} = 13.03 (s,1H, NH), 7.23-7.96 (m, Ar H, 12H), 8.26 (d, 2H, J = 8.2 Hz).

3.A.6.8 4-(4,5-diphenyl-1H-imidazol-2-yl)phenol (4h): White solid, yield=89%, melting point (°C)= 232-234, IR (KBr, cm^{-1}) ν_{max} =3448(NH), 3178 (Aromatic C-H), 1641, (C=C), 1612(C=N), ^1H NMR (400 MHz, DMSO- d_6): δ_{ppm} = 12.41 (s,1H, NH), 9.73 (s, 1H, OH), 6.86-8.31 (m, Ar H, 14H).

3.A.6.9 4-(4,5-diphenyl-1H-imidazol-2-yl)-N,N-dimethylaniline (4i): Brown solid, yield=97%, melting point (°C)= 257-260, IR (KBr, cm^{-1}) ν_{max} = 3427(NH),3060 (Aromatic C-H),1615(C=C), 1552(C=N), ^1H NMR (400 MHz, DMSO- d_6): δ_{ppm} = 13.03(s,1H, NH), 8.26 (d, 2H), 7.96 (d, 2H), 7.25-7.56 (m,

Ar H, 10H).

3.A.6.10 3-(4,5-diphenyl-1H-imidazol-2-yl)phenol (4j): White solid, yield =98%, melting point (°C)= 270-274, IR (KBr, cm^{-1}) ν_{max} =3423(NH), 3061(Aromatic C-H), 1593(C=N), ^1H NMR (400 MHz, DMSO- d_6): δ ppm =13.51 (s,1H, NH), 9.75 (s, 1H, OH), 6.87 (d, 2H, Ar-H), 7.30-7.93 (m, Ar H, 12H).

3.A.6.11 2-(4,5-diphenyl-1H-imidazol-2-yl)phenol (4k): White solid, yield=97%, melting point(°C)= 205-207, IR (KBr, cm^{-1}) ν_{max} =3443(NH), 3060 (Aromatic C-H), 1621(C=C), 1603(C=N), ^1H NMR (400 MHz, DMSO- d_6): δ ppm = 12.97(s,1H, NH), 12.7(s,1H,OH), 6.95-8.13 (m, Ar H, 14H).

3.A.6.12 4-chloro-2-(4,5-diphenyl-1H-imidazol-2-yl)phenol (4l): White solid, yield=94%, melting point (°C)= >300, IR (KBr, cm^{-1}) ν_{max} = 3443(NH), 3060 (Aromatic C-H), 1644(C=C), 1595(C=N), ^1H NMR (400 MHz, DMSO- d_6): δ ppm = 13.13(s,1H, NH), 10.27(s,1H,OH), 6.95-8.23(m, Ar H, 13H).

3.A.6.13 4-bromo-2-(4,5-diphenyl-1H-imidazol-2-yl)phenol (4m): White solid, yield=96%, melting point (°C)=179-181, IR (KBr, cm^{-1}) ν_{max} =3449(NH), 3053 (Aromatic C-H), 1636(C=C), 1610(C=N), ^1H NMR (400 MHz, DMSO- d_6): δ ppm = 13.15(s,1H, NH), 13.09(s,1H,OH), 6.91-8.31(m, Ar H, 13H).

3.A.6.14 2-(4,5-diphenyl-1H-imidazol-2-yl)-4-nitrophenol (4n): yellow solid, yield=96%, melting point (°C)= 262-264, IR (KBr, cm^{-1}) ν_{max} =3443(NH), 2958, 1633(C=C),(C=N), ^1H NMR (400 MHz, DMSO- d_6): δ ppm = 13.3(s,1H, NH), 8.6 (s,1H,OH), 7.20-7.50(m, Ar H, 13H).

3.A.6.15 4-(4,5-diphenyl-1H-imidazol-2-yl)benzene-1,3-diol (4o): Black solid, yield=97%, melting point (°C)= 270-273, IR KBr, (cm^{-1}) ν_{max} =3443(NH), 3063 (Aromatic C-H), 1619(C=C), 1606(C=N), ^1H NMR (400 MHz, DMSO- d_6): δ ppm = 12.943(s,1H, NH), 9.73(s,1H, OH), 6.18-8.11(m, Ar H, 13H), 4.049 (s,1H, OH).

3.A.6.16 2-methoxy-6-(4,5-diphenyl-1H-imidazol-2-yl)phenol (4p): White solid, yield=95%, melting point (°C)=168-172, IR (KBr, cm^{-1}) ν_{max} =3464(NH), 3050, 1632(C=C), 1604(C=N), ^1H NMR (400 MHz, DMSO- d_6): δ ppm = 12.97(s,1H, NH), 6.86-7.67(m, Ar H, 13H), 4.28(s,1H, OH),3.87(s,3H, OCH₃).

3.A.6.17 4-(4,5-diphenyl-1H-imidazol-2-yl)-2-methoxyphenol (4q): White solid, yield= 94%, melting point (°C)=258-262, IR (KBr, cm^{-1}) ν_{max} =3447(NH), 2970 Aromatic C-H), 1647(C=C), 1606(C=N), ^1H NMR (400 MHz, DMSO- d_6): δ ppm = 12.41(s,1H, NH), 6.83-7.67(m, Ar H, 13H), 4.03 (s,1H, OH),3.90(s,3H, OCH₃).

3.A.6.18 2-(4-(4,5-diphenyl-1H-imidazol-2-yl)phenyl)-5,6-diphenyl-1H-benzo[d]imidazole (4r): yellow solid, yield=86%, melting point (°C)=210-212, IR (KBr, cm^{-1}) ν_{max} =3443, 3424(NH), 3048 (Aromatic C-H), 1654(C=C), 1605, 1531(C=N), ^1H NMR (400 MHz, DMSO- d_6): δ ppm = 12.72(s,1H, NH), 8.21 (d,

2H),7.25-7.55(m, Ar H, 14H).

3.A.6.19 4-(4,5-diphenyl-1H-imidazol-2-yl)-2,6-dimethoxyphenol (4s): white solid, yield: 94%, melting point (°C)=190-192, IR (KBr, cm^{-1}) ν_{max} =3511(NH), 3027 (Aromatic C-H), 1615(C=C), 1543(C=N), ^1H NMR (400 MHz, DMSO-d₆): δ_{ppm} = 13.97(s,1H, NH), 9.15(s,1H, OH), 7.19-8.18(m, Ar H, 12H), 3.36 (s, OCH₃, 6H).

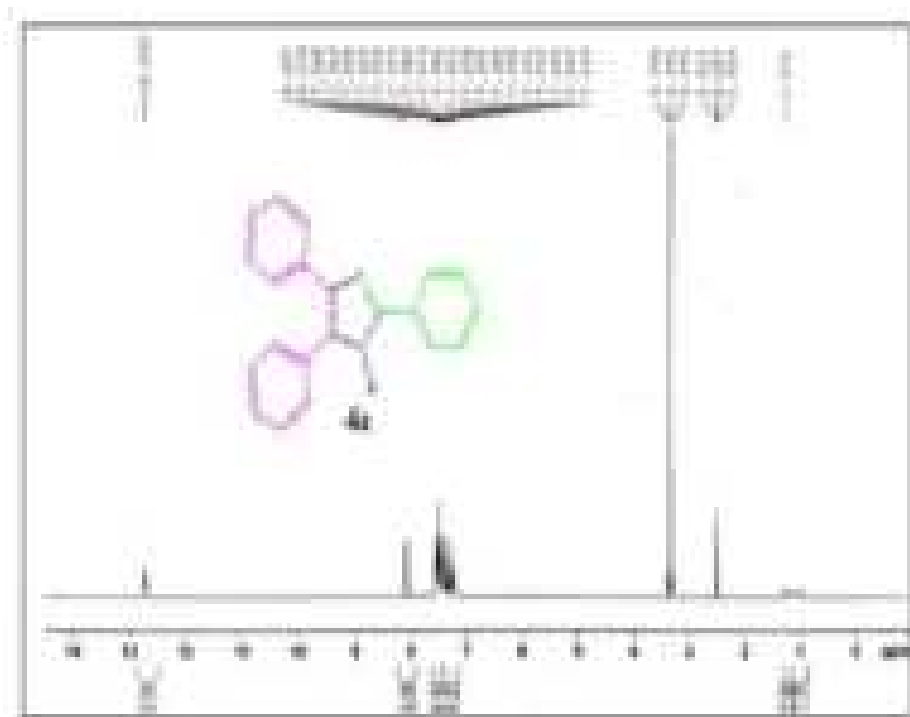
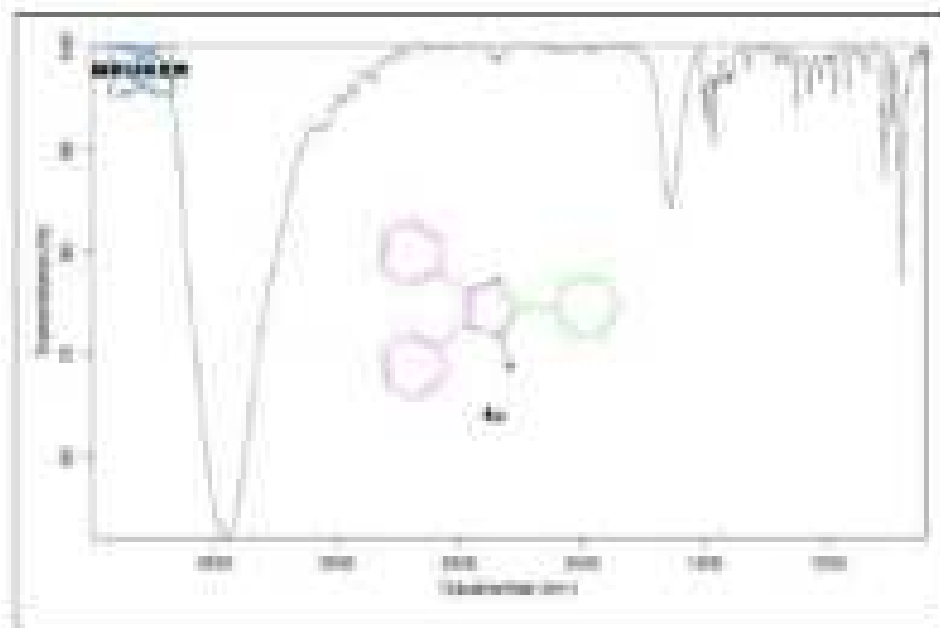
3.A.6.20 2-(4,5-diphenyl-1H-imidazol-2-yl)-1H-indole (4t):yellow solid, yield=96%, melting point (°C)= 306-308, IR (KBr, cm^{-1}) ν_{max} =3413(NH), 3056 (Aromatic C-H), 1622(C=C), 1598(C=N), ^1H NMR (400 MHz, DMSO-d₆): δ_{ppm} = 12.31(s,1H, NH), 11.40(s,1H, NH), 7.13-8.50(m, Ar H, 15H).

3.A.6.21 4,5-diphenyl-2-styryl-1H-imidazole (4u): White solid, yield=92%, melting point (°C)=140-143, IR (KBr, cm^{-1}) ν_{max} =3449(NH), 3060 (Aromatic C-H), 1646(C=C), 1600(C=N), ^1H NMR (400 MHz, DMSO-d₆): δ_{ppm} = 12.6(s,1H, NH), 7.58-7.92(m, Ar H, 15H), 6.52(d,2H, CH=CH).

3.A.6.22 2-(10-chloroanthracen-9-yl)-4,5-diphenyl-1H-imidazole (4v): yellow solid, yield= 93%, melting point (°C)>300, IR (KBr, cm^{-1}) ν_{max} = 3465(NH), 3428(Ar C-H stretch), 3048, 1654(C=C), 1605(C=N), ^1H NMR (400 MHz, DMSO-d₆): δ_{ppm} = 13.07(s,1H, NH), 8.56 (d 2H Ar-H J=8.0 Hz), 7.29-8.51(m, Ar H, 16H).

3.A.6.23 4,5-diphenyl-2-(3,4,5-trimethoxyphenyl)-1H-imidazole (4w): white solid, yield=98%, melting point (°C)= 162-166, IR (KBr, cm^{-1}) ν_{max} =3354(NH), 2930 (Aromatic C-H), 1625(C=C), 1590(C=N), ^1H NMR (400 MHz, DMSO-d₆): δ_{ppm} = 12.3(s,1H, NH),7.20-7.62(m, Ar H, 12H), 3.89(s,9H,OCH₃).

3.A.7 Supporting spectra:

**Fig. 3.A.7.1.** ¹H NMR spectra of 2,4,5-triphenyl-1H-imidazole (4a)**Fig. 3.A.7.2.** FT-IR spectra of 2,4,5-triphenyl-1H-imidazole (4a)

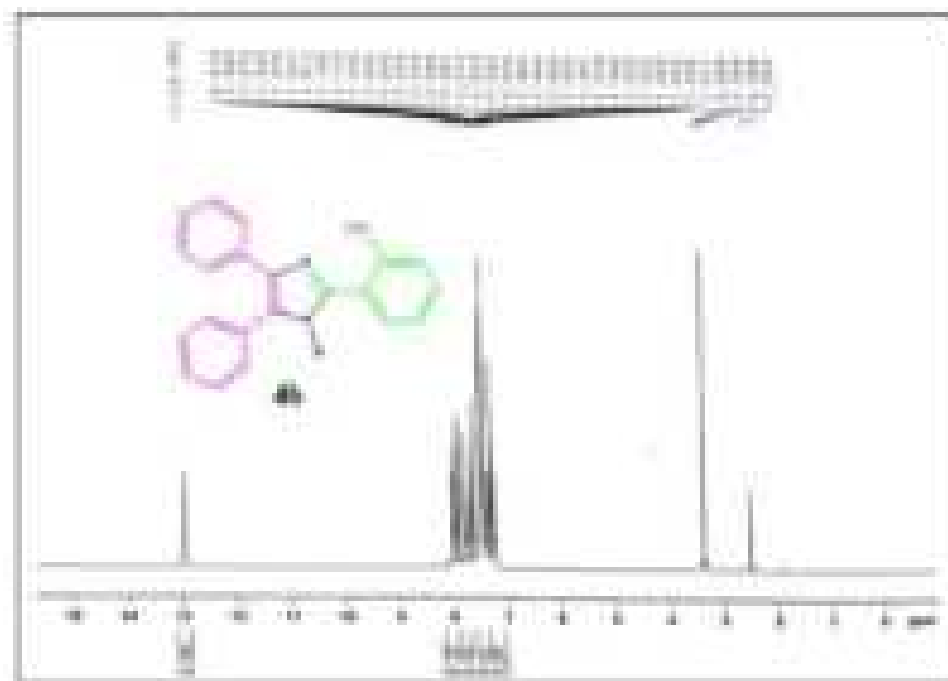


Fig. 3.A.7.3. ^1H NMR spectra of 2-(2-nitrophenyl)-4,5-diphenyl-1H-imidazole (4b)

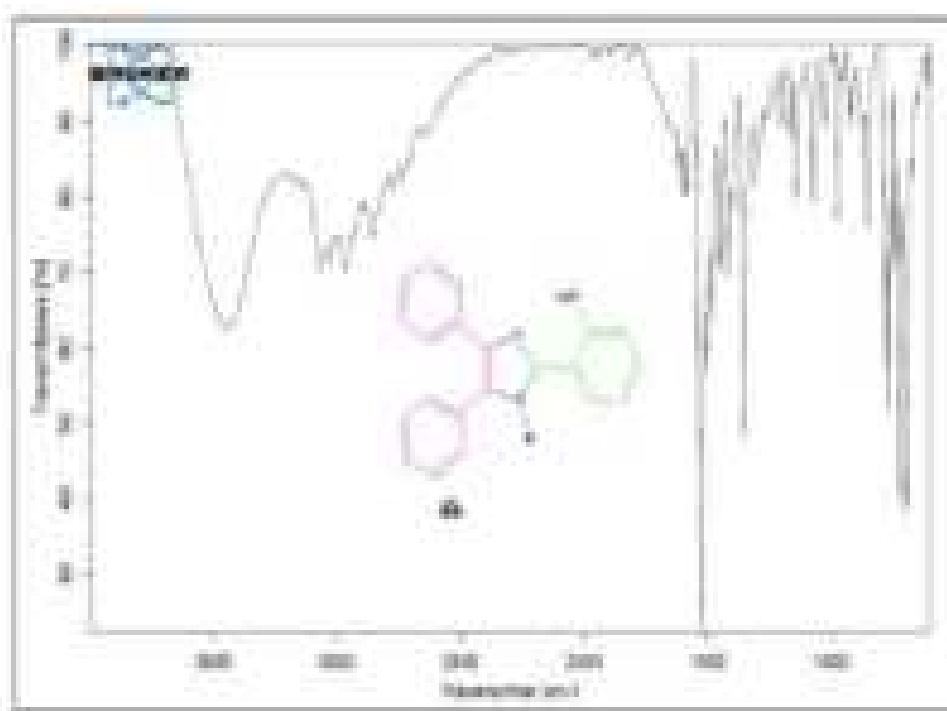


Fig. 3.A.7.4. FT-IR spectra of 2-(2-nitrophenyl)-4,5-diphenyl-1H-imidazole (4b)

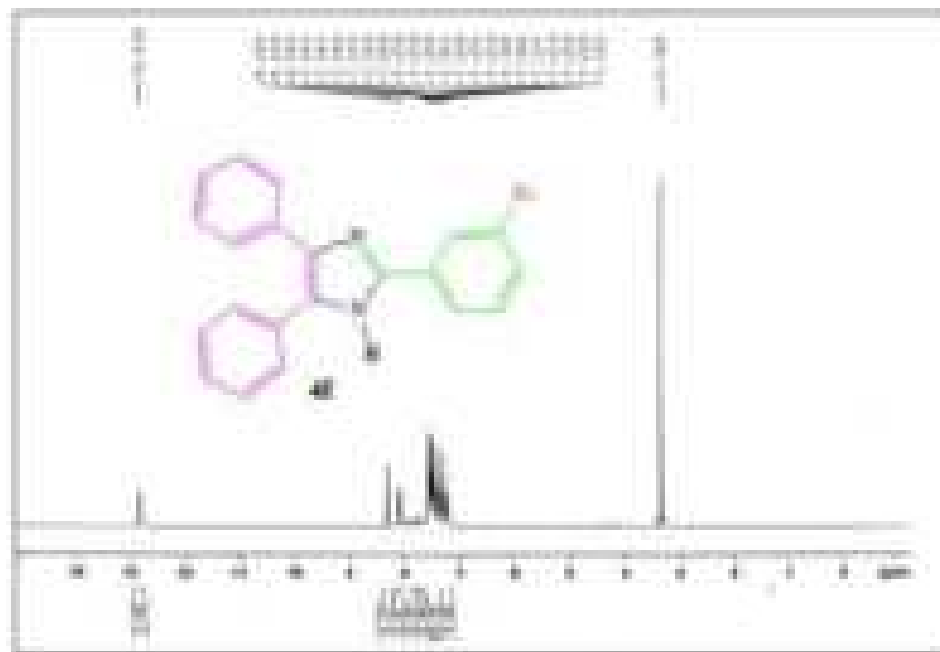


Fig. 3.A.7.5. ¹H NMR of 2-(3-bromophenyl)-4,5-diphenyl-1H-imidazole(4f)

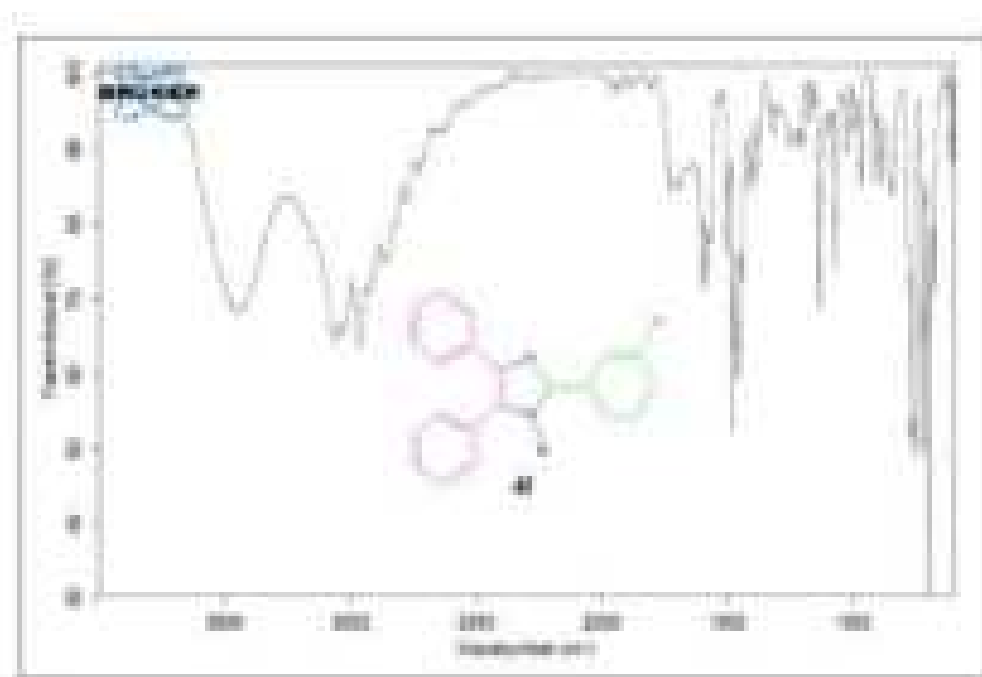


Fig. 3.A.7.6. FT-IR spectra of 2-(3-bromophenyl)-4,5-diphenyl-1H-imidazole (4f)

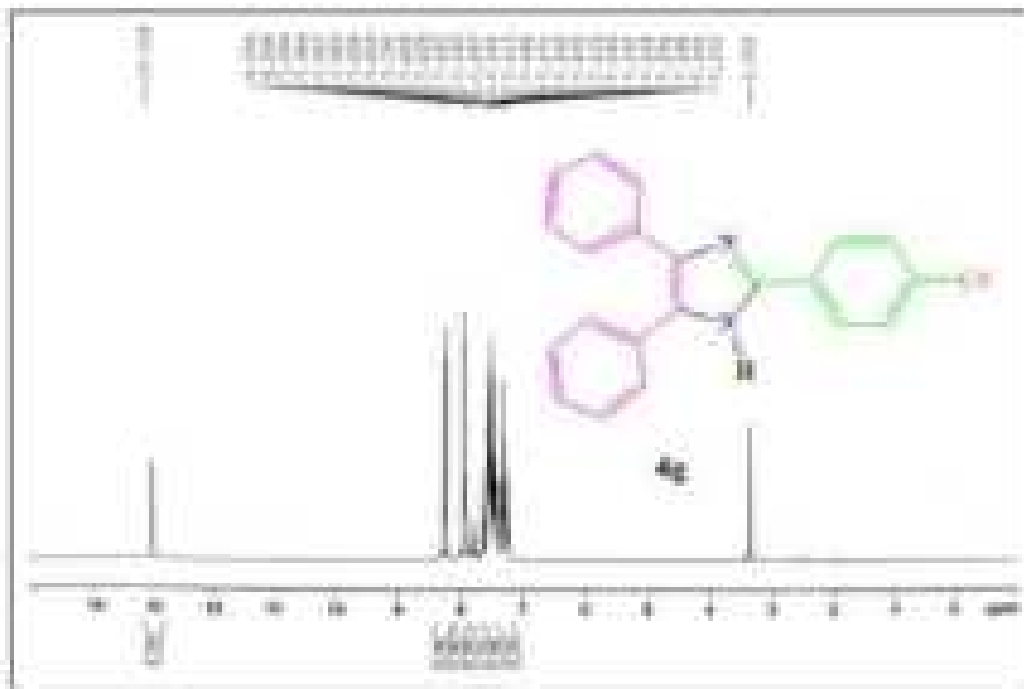


Fig. 3.A.7.7. ¹H NMR of 4-(4,5-diphenyl-1H-imidazol-2-yl)benzonitrile(4g)

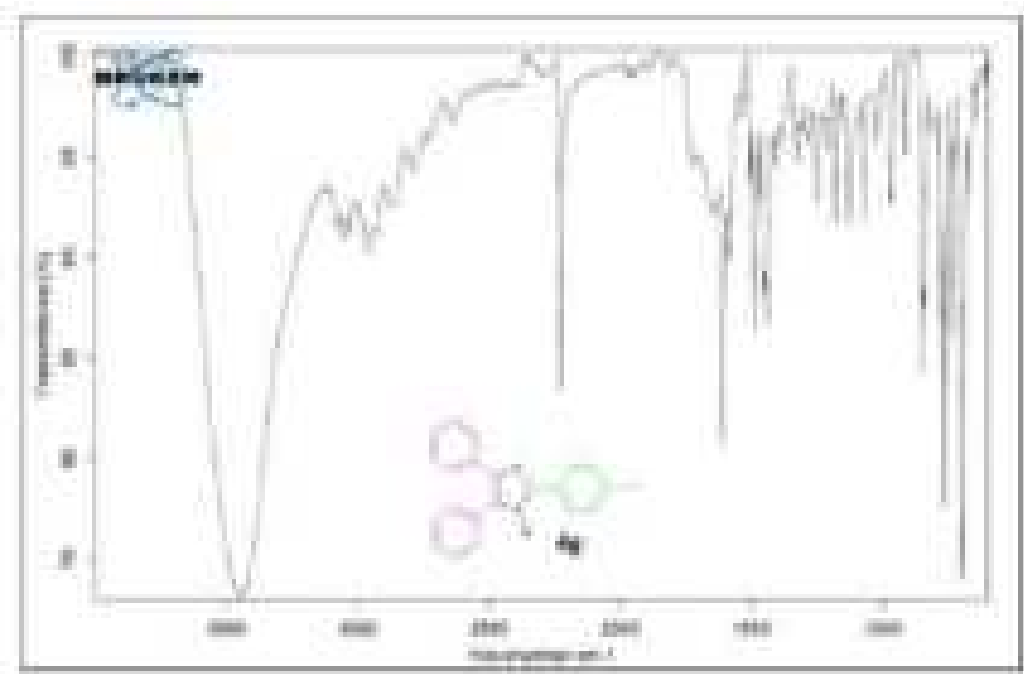


Fig. 3.A.7.8 FT-IR spectra of 4-(4,5-diphenyl-1H-imidazol-2-yl)benzonitrile(4g)

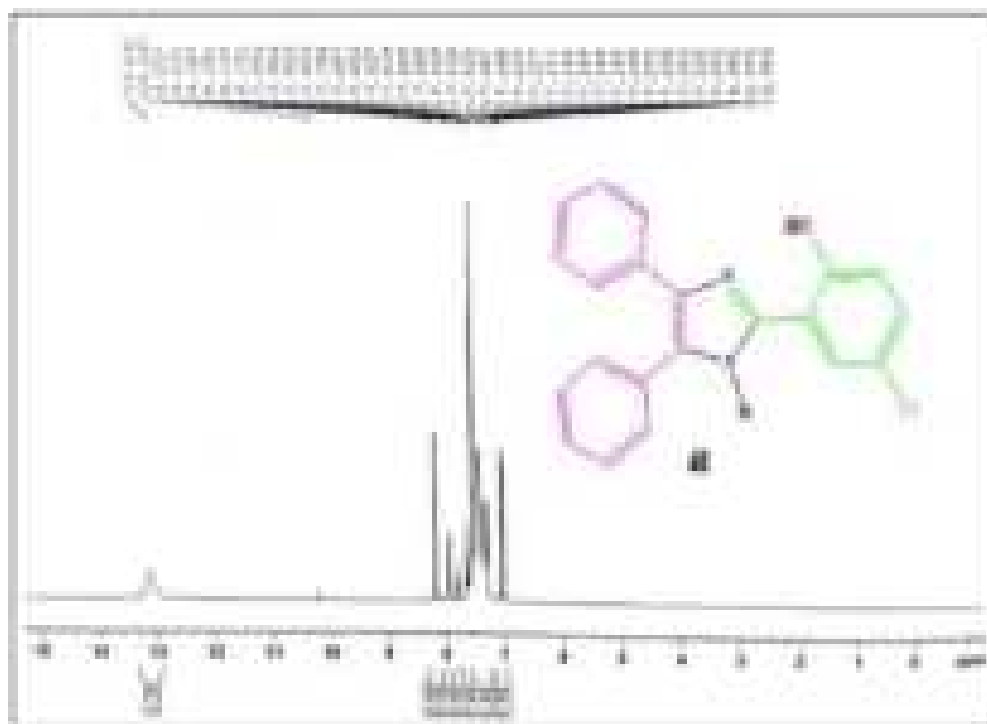


Fig. 3.A.7.9. ¹H NMR of 4-chloro-2-(4,5-diphenyl-1H-imidazol-2-yl)phenol (4l)

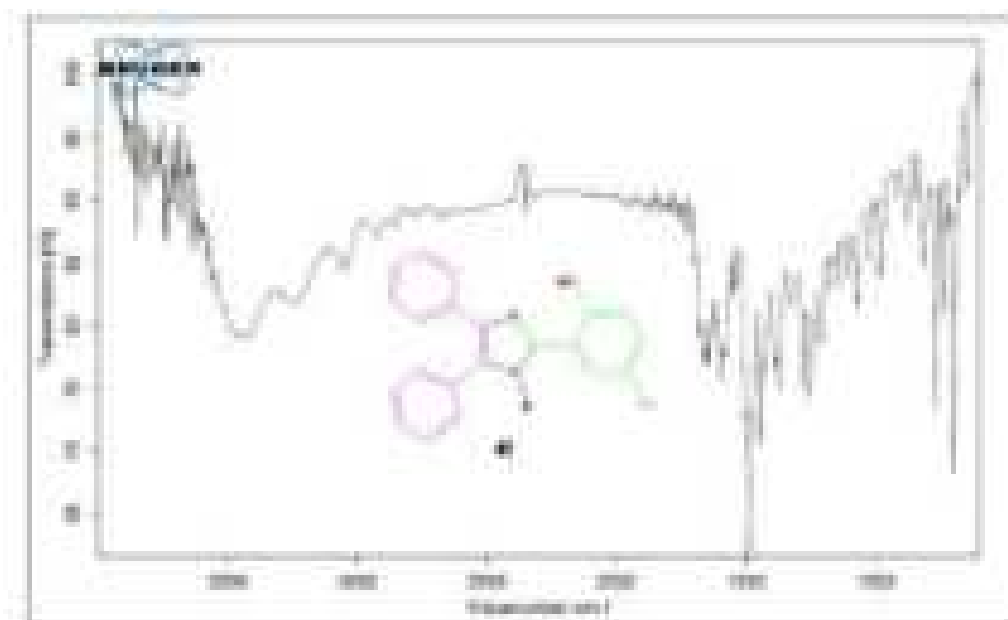


Fig. 3.A.7.10. FT-IR spectra of 4-chloro-2-(4,5-diphenyl-1H-imidazol-2-yl)phenol (4l)

****Rest of the spectras are given in Appendix-I****

3.A.8 References

- (1) P. T. Anastas, T. C. Williamson., *Green Chemistry : Frontiers in Benign Chemical Syntheses and Processes*; Oxford Science Publications: New York, **1998**.
- (2) M. Poliakoff, P. Anastas., *Nature*, **2001**, *413* (6853).
- (3) J. M. DeSimone., *Science (1979)*, **2002**, *297* (5582), 799–803.
- (4) R. A. Sheldon., *Green Chemistry*, **2016**, *18* (11), 3180–3183.
- (5) R. A. Sheldon., *Green Chemistry*, **2017**, *19* (1), 18–43.
- (6) P. Gupta, A. Mahajan., *RSC Advances*, **2015**, *5* (34), 26686–26705.
- (7) R. R. Magar, S. S. Choudhare, S. V. Padghan., *International Journal of Multidisciplinary Research (Epitome Journals)*, **2015**, *1* (7), 1–9.
- (8) E. Ezzatzadeh, F. Z. Hargalani, F. Shafaei., *Polycyclic Aromatic Compounds*, **2021**, *0* (0), 1–16.
- (9) T. Welton., *Green Chemistry*, **2011**, *13* (2), 225.
- (10) G. Centi, S. Perathoner., *Catalysis Today*, **2003**, *77* (4), 287–297.
- (11) P. T. Anastas, M. M. Kirchhoff, T. C. Williamson., *Applied Catalysis A: General*, **2001**, *221* (1–2), 3–13.
- (12) A. Dömling, U. Ivar., *Angewandte Chemie International Edition*, **2000**, *39* (18), 3168–3210.
- (13) J. E. Biggs-Houck, A. Younai, J. T. Shaw., *Current Opinion in Chemical Biology*, **2010**, *14* (3), 371–382.
- (14) B. Jiang, T. Rajale, W. Wever, S. J. Tu, G. Li., *Chemistry – An Asian Journal*, **2010**, *5* (11), 2318–2335.
- (15) S. Brauch, S. S. van Berkel, B. Westermann., *Chemical Society Reviews*, **2013**, *42* (12), 4948–4962.
- (16) C. de Graaff, E. Ruijter, R. V. A. Orru., *Chemical Society Reviews*, **2012**, *41* (10), 3969–4009.
- (17) M. C. Pirrung, K. das Sarma., *Tetrahedron*, **2005**, *61* (48), 11456–11472.
- (18) C. G. Neochoritis, T. Zarganes-Tzitzikas, K. Katsampoxaki-Hodgetts, A. Dömling., *Journal of Chemical Education*, **2020**, *97* (10), 3739–3745.
- (19) S. Garbarino, D. Ravelli, S. Protti, A. Basso., *Angewandte Chemie International Edition*, **2016**, *55* (50), 15476–15484.

- (20) G. van der Heijden, E. Ruijter, R. V. A. Orru., *Synlett*, **2013**, 24 (6), 666–685.
- (21) D. Insuasty, J. Castillo, D. Becerra, H. Rojas, R. Abonia., *Molecules*, **2020**, 25 (3), 576.
- (22) J. G. Lombardino, E. H. Wiseman., *Journal of Medicinal Chemistry*, **1974**, 17 (11), 1182–1188.
- (23) A. Chawla, A. Sharma, A. Kumar Sharma., *Der Pharma Chemica*, **2012**, 4 (1), 116–140.
- (24) R. Breslow., *Accounts of Chemical Research*, **1995**, 28 (3), 146–153.
- (25) A. P. Kulkarni, C. J. Tonzola, A. Babel, S. A. Jenekhe., *Chemistry of Materials*, **2004**, 16 (23), 4556–4573.
- (26) L. Streit, M. Moreau, J. Gaudin, E. Ebert, H. vanden Bossche., *Pesticide Biochemistry and Physiology*, **1991**, 40 (2), 162–168.
- (27) A. Husain, S. Drabu, N. Kumar, M. M. Alam, S. Bawa., *Journal of Pharmacy And Bioallied Sciences*, **2013**, 5 (2), 161.
- (28) T. Scior, D. M. Domeyer, K. Cuanalo-Contreras, S. A. Laufer., *Current Medicinal Chemistry*, **2011**, 18 (10), 1526–1539.
- (29) A. K. Takle, M. J. B. Brown, S. Davies, D. K. Dean, G. Francis, A. Gaiba, A. W. Hird, F. D. King, P. J. Lovell, A. Naylor, A. D. Reith, J. G. Steadman, D. M. Wilson., *Bioorganic & Medicinal Chemistry Letters*, **2006**, 16 (2), 378–381.
- (30) L. Wang, K. W. Woods, Q. Li, K. J. Barr, R. W. McCroskey, S. M. Hannick, L. Gherke, R. B. Credo, Y. H. Hui, K. Marsh, R. Warner, J. Y. Lee, N. Zielinski-Mozng, D. Frost, S. H. Rosenberg, H. L. Sham., *J Med Chem*, **2002**, 45 (8), 1697–1711.
- (31) A. R. Phillips, H. L. White, S. Rosen., European Patent Application EP 58 8901; Chemical Abstracts, 98, 53894z; **1982**.
- (32) R. A. Turner, C. F. Huebner, C. R. Scholz., *J Am Chem Soc*, **1949**, 71 (8), 2801–2803.
- (33) J. Miller., *Annals of Allergy*, **1963**, 21, 692–697.
- (34) A. Goyal, J. Singh, D. P. Pathak., *Journal of Pharmaceutical Technology, Research and Management*, **2013**, 1 (1), 69–79.
- (35) K. Gaffney, D. G. I. Scott., *British Journal of Rheumatology*, **1998**, 37 (8), 824–836.
- (36) J. Baharara, E. Amini, N. Nikdel, F. Salek-Abdollahi., *Avicenna Journal of Medical Biotechnology*, **2016**, 8 (3), 119.

- (37) J.-B. Tagne, S. Kakumanu, R. J. Nicolosi., *Molecular Pharmaceutics*, **2008**, 5 (6), 1055–1063.
- (38) R. S. Joshi, P. G. Mandhane, M. U. Shaikh, R. P. Kale, C. H. Gill., *Chinese Chemical Letters*, **2010**, 21 (4), 429–432.
- (39) C. Yu, M. Lei, W. Su, Y. Xie., *Synthetic Communications*, **2007**, 37 (19), 3301–3309.
- (40) S. D. Sharma, P. Hazarika, D. Konwar., *Tetrahedron Letters*, **2008**, 49 (14), 2216–2220.
- (41) J. N. Sangshetti, N. D. Kokare, S. A. Kotharkara, D. B. Shinde., *Journal of Chemical Sciences*, **2008**, 120 (5), 463–467.
- (42) S. N. Murthy, B. Madhav, Y. V. D. Nageswar., *Tetrahedron Letters*, **2010**, 51 (40), 5252–5257.
- (43) S. Samai, G. C. Nandi, P. Singh, M. S. Singh., *Tetrahedron*, **2009**, 65 (49), 10155–10161.
- (44) A. R. Khosropour., *Ultrasonics Sonochemistry*, **2008**, 15 (5), 659–664.
- (45) R. K. Sharma, C. Sharma., *Catalysis Communications*, **2011**, 12 (5), 327–331.
- (46) M. Kidwai, P. Mothra, V. Bansal, R. K. Somvanshi, A. S. Ethayathulla, S. Dey, T. P. Singh., *Journal of Molecular Catalysis A: Chemical*, **2007**, 265 (1–2), 177–182.
- (47) G. H. Mahdavinia, A. M. Amani, H. Sepehrian., *Chinese Journal of Chemistry*, **2012**, 30 (3), 703–708.
- (48) H. Zang, Q. Su, Y. Mo, B. W. Cheng, S. Jun., *Ultrasonics Sonochemistry*, **2010**, 17 (5), 749–751.
- (49) M. Xia, Y. dong Lu., *Journal of Molecular Catalysis A: Chemical*, **2007**, 265 (1–2), 205–208.
- (50) M. Veerananarayana Reddy, Y. T. Jeong., *Journal of Fluorine Chemistry*, **2012**, 142, 45–51.
- (51) J. Jayram, V. Jeena., *Green Chemistry*, **2017**, 19 (24), 5841–5845.
- (52) J. Jayram, V. Jeena., *RSC Advances*, **2018**, 8 (66), 37557–37563.
- (53) K. Nikoofar, M. Haghghi, M. Lashanizadegan, Z. Ahmadvand., *Journal of Taibah University for Science*, **2015**, 9 (4), 570–578.
- (54) M. Kalhor, Z. Zarnegar., *RSC Advances*, **2019**, 9 (34), 19333–19346.

- (55) M. Kalhor, N. Khodaparast., *Research on Chemical Intermediates*, **2015**, *41* (5), 3235–3242.
- (56) A. Bamoniri, B. B. Fatemeh Mirjalili, S. Saleh., *RSC Advances*, **2018**, *8* (11), 6178–6182.
- (57) A. Khorramabadi-zad, M. Azadmanesh, S. Mohammadi., *South African Journal of Chemistry*, **2013**, *66* (1), 244–247.
- (58) N. V. Gandhare, R. G. Chaudhary, V. P. Meshram, J. A. Tanna, S. Lade, M. P. Gharpure, H. D. Juneja., *Journal of the Chinese Advanced Materials Society*, **2015**, *3* (4), 270–279.
- (59) Z. Varzi, M. S. Esmacili, R. Taheri-Ledari, A. Maleki., *Inorganic Chemistry Communications*, **2021**, *125*, 108465.
- (60) D. Kumar, D. N. Kommi, N. Bollineni, A. R. Patel, A. K. Chakraborti., *Green Chemistry*, **2012**, *14* (7), 2038–2049.
- (61) K. Sivakumar, A. Kathirvel, A. Lalitha., *Tetrahedron Letters*, **2010**, *51* (22), 3018–3021.
- (62) N. V. Shitole, K. F. Shelke, S. S. Sonar, S. A. Sadaphal, B. B. Shingate, M. S. Shingare., *Bull Korean Chem Soc*, **2009**, *30* (9), 1963–1966.
- (63) S. S. Dipake, M. K. Lande, A. S. Rajbhoj, S. T. Gaikwad., *Research on Chemical Intermediates*, **2021**, *47* (6), 2245–2261.
- (64) A. R. Khosropour., *Ultrasonics Sonochemistry*, **2008**, *15* (5), 659–664.
- (65) L. M. Wang, Y. H. Wang, H. Tian, Y. F. Yao, J. H. Shao, B. Liu., *Journal of Fluorine Chemistry*, **2006**, *127* (12), 1570–1573.
- (66) K. Nikoofar, M. Haghighi, M. Lashanizadegan, Z. Ahmadvand., *Journal of Taibah University for Science*, **2015**, *9* (4), 570–578.
- (67) M. Kidwai, P. Mothsra, V. Bansal, R. Goyal., *Monatshefte für Chemie / Chemical Monthly*, **2006**, *137* (9), 1189–1194.
- (68) M. Banazadeh, S. Amirnejat, S. Javanshir., *Frontiers in Chemistry*, **2020**, *8* (Article 596029), 1–15.
- (69) J. Safari, S. D. Khalili, S. H. Banitaba., *Synthetic Communications*, **2011**, *41* (16), 2359–2373.
- (70) J. Safari, S. D. Khalili, M. Rezaei, S. H. Banitaba, F. Meshkani., *Monatshefte für Chemie - Chemical Monthly*, **2010**, *141* (12), 1339–1345.
- (71) E. Eidi, M. Z. Kassae, Z. Nasresfahani., *Applied Organometallic Chemistry*, **2016**, *30* (7), 561–565.

- (72) R. Wang, C. Liu, G. Luo., *Green Chemistry Letters and Reviews*, **2010**, 3 (2), 101–104.
- (73) K. F. Shelke, S. B. Sapkal, S. S. Sonar, B. R. Madje, B. B. Shingate, M. S. Shingare., *Bull Korean Chem Soc*, **2009**, 30 (5), 1057–1060.
- (74) M. Vosoughi, F. Mohebbali, A. P. S. Bonakdar, H. A. Lordegani, A. R. Massah., *Bulgarian Chemical Communications*, **2015**, 47 (2), 607–612.
- (75) B. F. Mirjalili, A. Bamoniri, N. Mohaghegh., *Current Chemistry Letters*, **2013**, 2 (1), 35–42.
- (76) G. Brahmachari, S. Das., *Indian Journal of Chemistry - Section B*, **2013**, 52B, 387–393.
- (77) B. Maleki, H. K. Shirvan, F. Taimazi, E. Akbarzadeh., *International Journal of Organic Chemistry*, **2012**, 2 (1), 93–99.
- (78) N. V. Gandhare, R. G. Chaudhary, V. P. Meshram, J. A. Tanna, S. Lade, M. P. Gharpure, H. D. Juneja., *Journal of the Chinese Advanced Materials Society*, **2015**, 3 (4), 270–279.
- (79) A. Sedrpoushan, Z. Joshani, L. Fatollahi., *Letters in Organic Chemistry*, **2014**, 11 (4), 287–292.
- (80) F. Hatamjafari, H. Khojastehkouhi., *Oriental Journal of Chemistry*, **2014**, 30 (1), 329–331.
- (81) S. Balalaie, A. Arabanian, M. S. Hashtroudi., *Monatshefte für Chemie/Chemical Monthly*, **2000**, 131 (9), 945–948.

CHAPTER-III

Section B

Bis[2-(4,5-diphenyl-1H-imidazol-2-yl)-4-nitro-phenolato] copper (II) dihydrate complex: Synthesis, Hirshfeld surface analysis, Catalytic activity and Evidence of *in-situ* conversion of CuB_4O_7 into $\text{Cu}(\text{OAc})_2 \cdot 2\text{H}_2\text{O}$ in presence of NH_4OAc *

3.B.1 Background of the present investigation

Among many transition metal ions, Copper (II) ion have been studied extensively owing to their versatile coordination geometries, exquisite colors, and numerous applications in the field such as medicine, biochemistry, spectroscopy and fluorescent chemo sensors¹⁻³. Copper ion draws significant consideration due to its very important role in fundamental biochemical processes in living organisms and also serves as a catalytic cofactor for a variety of metalloenzymes taking advantage of its redox and catalytic properties⁴⁻⁶. Interestingly, Imidazole motif being a five-membered nitrogen heterocyclic compound is ubiquitous in wide range of naturally occurring organic molecules and it serves as an important scaffold in various metalloenzymes and non-natural metal complexes⁷⁻¹⁰. Moreover, imidazole scaffold is present in the side chain of amino acid histidine which is present in many proteins, enzymes and metalloenzymes and plays an important role in numerous biochemical processes¹¹. A remarkable and interesting biological activity is observed when copper ion combines with the imidazole motif and one such example is plastocyanin in which Cu (II) binds to histidine residue¹² (Fig. 3.B.1).

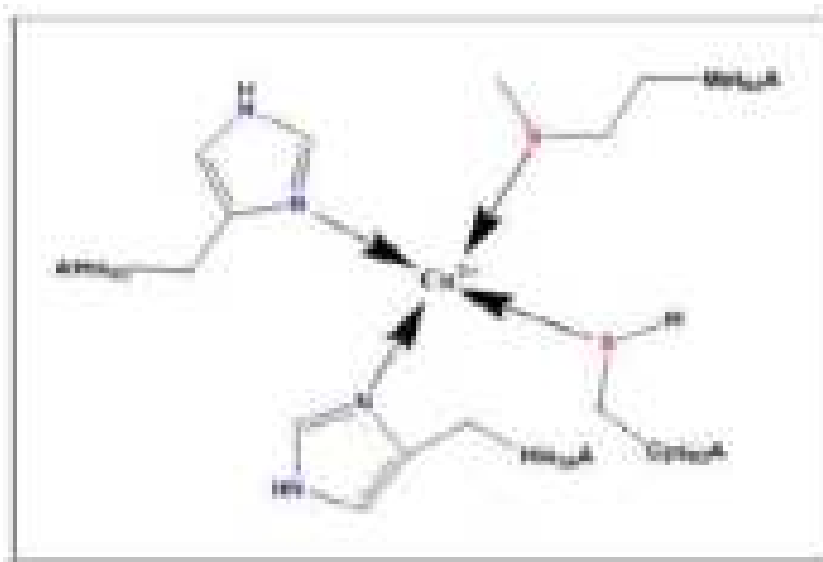


Fig. 3.B.1. Structure of plastocyanin

***Published in Acta Cryst. (2019). E75, 1664–1671**

Apart from the naturally occurring copper-imidazole complex, there is a vast literature on the synthetic copper complex with imidazole ligand^{13,14}. Over the past few decades, synthesis of copper (II) coordination complexes with imidazole and substituted imidazole ligand has been rapidly developing owing to their widespread range of potential applications such as catalysis, gas absorption, photocatalysis, electrocatalytic, magnetic, perovskite solar cell⁷, luminescence, etc and structural diversity¹⁵⁻²⁰.

Interestingly, during our ongoing research for the development of efficient catalyst for the synthesis of 2,4,5-triarylimidazole derivatives under green condition by utilizing copper borate as a catalyst, we encountered an *in-situ* formation of copper (II) complex with synthesized 2,4,5-triarylimidazole ligand and we also observed that during the reaction copper borate was converted into copper acetate in presence of ammonium acetate. Hence, in this chapter we will discuss about the *in-situ* formation of copper complex with synthesized 2,4,5-triarylimidazole and conversion of copper borate and other copper salts to copper acetate in presence of ammonium acetate.

3.B.2 Results and discussion

3.B.2.1 *In-situ* formation of Bis[2-(4,5-diphenyl-1H-imidazol-2-yl)-4-nitrophenolato] copper (II) dihydrate (1)

In chapter III section A, we reported the catalytic efficacy of CuB_4O_7 for the green synthesis of 2,4,5-triarylimidazole derivatives under solvent free condition and during the reaction, interestingly, we encountered that the catalyst could not be recovered after final work up of the product. Since, the catalyst copper borate was insoluble in most of the solvents and also, we carried out the reaction under neat condition and therefore, we were hopeful to recover the catalyst in fair amount but surprisingly, we found that during the addition of catalyst to the reaction mixture, the reaction mixture turned blue and after the work-up of the product, unfortunately the desired catalyst could not be recovered. Therefore, we focused our research to find out the actual reason for non-recovery of the catalyst. Moreover, the catalyst efficiently afforded the desired 2,4,5-triarylimidazole derivatives in good to excellent yield yet still there were some doubts for the non-recyclability of the catalyst. Fortunately, when we used aromatic aldehyde as 2-OH-benzaldehyde derivatives, we encountered that there was formation of some blue colored product in the reaction mixture along with the desired product. We then carefully recrystallized the blue colored compound in N,N-dimethylformamide (DMF) solvent and after 5 days a blue colored crystal suitable for X-ray single crystal diffraction was isolated for the reaction where we used 2-OH-5-NO₂benzaldehyde. After successful X-ray single crystal diffraction study, it was revealed that the desired imidazole product was formed during the reaction but the product itself acted as a bidentate chelating ligand for the copper (II) ion in the reaction mixture thereby forming Bis [2-(4, 5-diphenyl-1H-imidazol-2-

yl)-4-nitro-phenolato] copper (II) dihydrate complex (1)²¹, (Fig. 3.B.2a and Fig. 3B.2b).

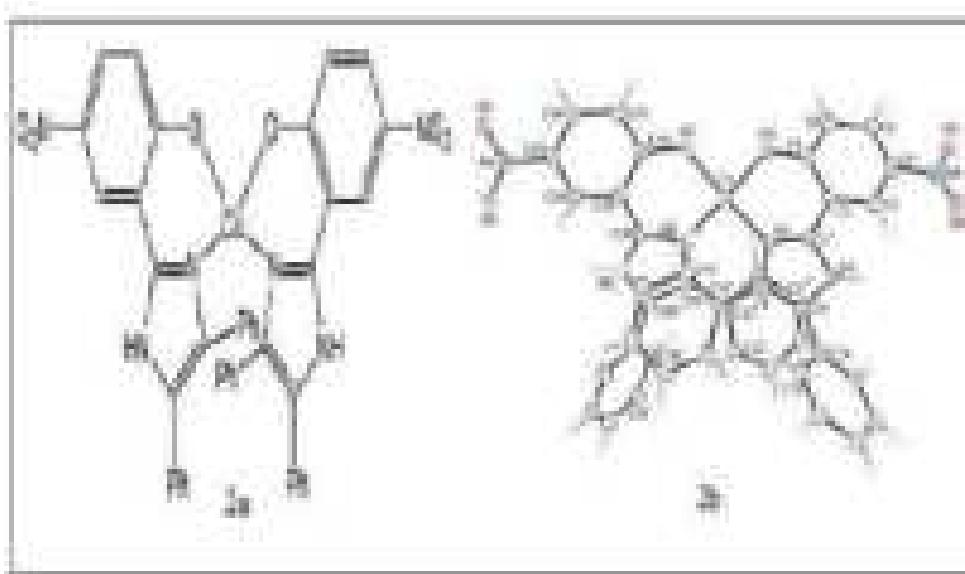


Fig. 3.B.2a-b . 2a) Molecular structure of complex (1) and 2b) Crystal structure of the complex molecule (1), showing the atom-labeling scheme and with displacement ellipsoids drawn at the 70% probability level (1).

3.B.2.2 Detailed study of the formation of Copper complex (1) and (2)

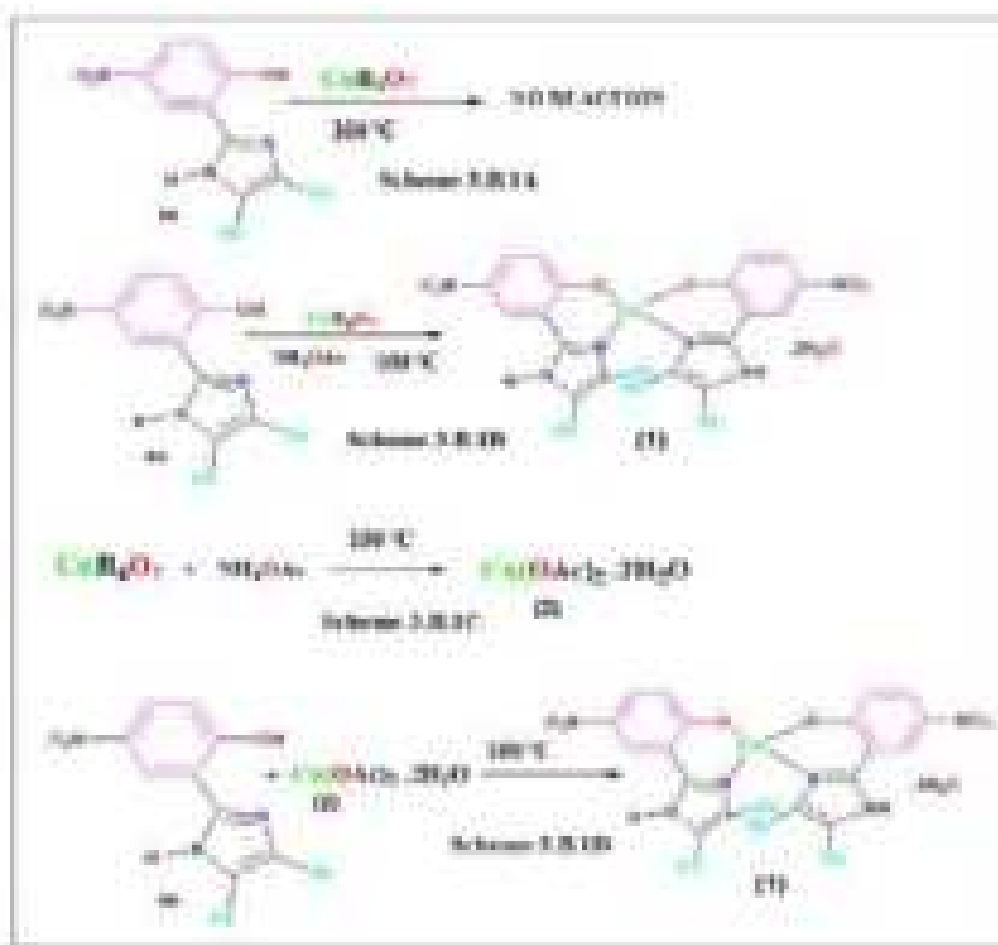
In order to understand the actual reason of *in-situ* formation of complex (1) we carried out the detailed study of transformation of copper borate into other intermediate in the reaction mixture under given condition separately.

Firstly, we synthesized 2-(4,5-diphenyl-1H-imidazol-2-yl)-4-nitrophenol (**4n**) ligand and subsequently reacted with CuB_4O_7 in neat condition at 100°C for 8-10 hours but we failed to get the desired product (1) (Scheme 3.B.1a) but when we added stoichiometric amount of NH_4OAc to the same reaction, the reaction mixture instantaneously turned blue and after reacting for 4 hours, the compound was extracted with DMF and the filtrate was kept for 5-8 days for slow evaporation at room temperature. Surprisingly, we got the same blue colored copper (II) complex (**1**) in excellent yield (60%) (Scheme 3.B.1b).

Secondly, in order to understand the role of NH_4OAc , a separate reaction was set up in which 1mmol of CuB_4O_7 was directly added to 50 ml of water containing 3mmol of NH_4OAc in 100 ml round bottomed flask (Scheme 3.B.1c) and the reaction mixture was allowed to stir at room temperature for 8 hours. It was seen that CuB_4O_7 slowly discharged into the NH_4OAc solution and with the passage of time entire CuB_4O_7 dissolved in the reaction mixture. The reaction mixture was

allowed to evaporate at room temperature and finally after 14 days blue colored single crystal suitable for X-ray single crystal diffraction study was appeared in the solution. After successful X-ray single crystal diffraction of the compound, it was appeared that the blue colored complex was Copper (II) acetate dihydrate²² (2) (Molecular formula $\text{Cu}_2\text{C}_8\text{H}_{16}\text{O}_{10}$) with monoclinic crystal system and (C 2/c) space group having paddle wheel type of structure.

Thus, it was evident from the above reaction that CuB_4O_7 in presence of NH_4OAc is converted to intermediate $\text{Cu}(\text{OAc})_2 \cdot 2\text{H}_2\text{O}$ in the reaction mixture and undergo metallation with the ligand (4n) to give the complex (1) under the given reaction condition. We again set up a reaction directly with the compound 4n employing $\text{Cu}(\text{OAc})_2 \cdot 2\text{H}_2\text{O}$ under the same reaction conditions and we obtained the same compound (1) (Scheme 3.B.1d).



(Scheme. 3.B.1a-3.B.1d). **3.B.1a**) Reaction between ligand 4n and CuB_4O_7 , **3.B.1b**) Reaction between ligand 4n and CuB_4O_7 in presence of NH_4OAc for the synthesis of (1), **3.B.1c**) Reaction between CuB_4O_7 and NH_4OAc to for compound (2) and **3.B.1d**) Reaction between ligand 4n and compound (2) to form compound (1).

Again, this finding prompted us to examine whether other copper salts such as CuO , CuSO_4 and CuCl_2 gets converted to copper acetate dihydrate or not in presence of ammonium acetate during the synthesis of 2, 4, 5-triarylimidazole derivatives and therefore we subsequently carried out the reaction of other copper salts with ammonium acetate under the same reaction condition separately. Interestingly it was observed that all the studied copper salts were converted to copper acetate dihydrate in presence of ammonium acetate as evident from the comparisons of FT-IR spectra of the reaction mixtures with that of the commercially available copper acetate dihydrate (Fig. 3.B.3).

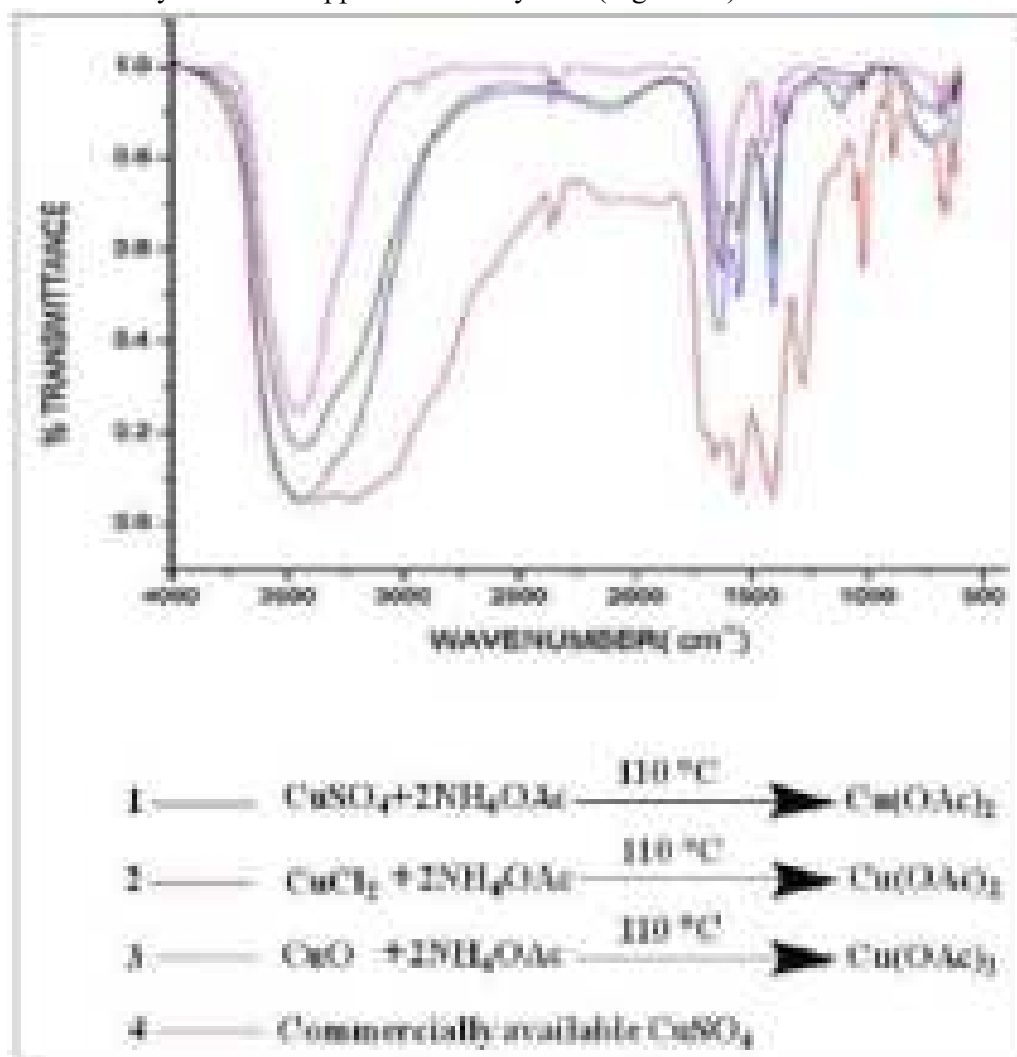


Fig. 3.B.3. (1) FT-IR spectra of the reaction mixture of CuSO_4 and NH_4OAc , (2) FT-IR spectra of the reaction mixture of CuCl_2 and NH_4OAc (3) FT-IR spectra of the reaction mixture of CuO and NH_4OAc and (4) FT-IR spectra of commercially available $\text{Cu(OAc)}_2 \cdot 2\text{H}_2\text{O}$

Thus, it is evident from the above findings that whenever we use Copper (II) salt as a catalyst for the synthesis of 2,4,5-triarylimidazole derivatives in presence of ammonium acetate, these salts are readily converted into copper acetate dihydrate in the reaction mixture. Hence an interesting feature of this finding is that we have been able to trap the acetate ion liberated from ammonium acetate as copper acetate dihydrate.

3.B.2.3 Description of crystal structure of copper complex (1) and (2)

3.B.2.3.1 Bis [2-(4, 5-diphenyl-1H-imidazol-2-yl)-4-nitro-phenolato] copper (II) dihydrate complex (1)

The title copper (II) complex, (1), was isolated during an ongoing research programme on the catalytic activity of copper borate (CuB_4O_7) for the synthesis of 2,4,5-triarylimidazole derivatives. Complex (1) was formed during the attempted synthesis of a triaryl imidazole derivative using benzil and 2-hydroxy 5-nitrobenzaldehyde with copper borate, using ammonium acetate as a nitrogen source. The single-crystal analysis of the synthesized product revealed that in the copper (II) complex, the triaryl imidazole moiety acts as a bidentate ligand for the copper atom. During the successful synthesis of the triaryl imidazole, the desired product formed in good yield at a temperature in the range 80-100°C. However, when the reaction was conducted at 100°C and above, the title copper (II) complex formed instead of the targeted triarylimidazole. The crystal and molecular structures of (1) are described herein, along with a detailed analysis of the molecular packing (Fig.3.B.2a-b). The crystallographic asymmetric unit of (1) comprises a complex molecule and two water molecules of crystallization. The crystallographic parameters and selected geometric parameters of the complex (1) are given in Table 3.B.1 and Table 3.B.2 respectively.

Table 3.B.1. Crystallographic parameters of complex (1)

Crystal data	
Chemical formula	[Cu(C ₂₁ H ₁₄ N ₃ O ₃) ₂].2H ₂ O141
M _r	812.27
Crystal system, space group	Monoclinic, P2 ₁ /c
Temperature (K)	100
a, b, c (Å)	13.2752 (2), 25.1602 (4), 11.1166 (2)
β(°)	141
V (Å ³)	3598.68 (10)
Z	4
Radiation type	Cu Kα
μ (mm ⁻¹)	1.42
Crystal size(mm)	0.14X 0.11X0.07
Data collection diffractometer	XtaLAB Synergy, Dualflex, AtlasS2
Absorption correction	Gaussian (CrysAlis PRO; Rigaku OD, 2018)
Tmin, Tmax	0.757, 1.000
No. Of measured, independent and observed [I > 2σ(I)] reflections	46023, 7490, 6420
R _{int}	0.058
(sin θ/ λ) _{max} (Å ⁻¹)	0.631
Refinement	
R[F ² >2 σ(F ²)], wR(F ²), S	0.047, 0.128, 1.05
No. Of reflections	7490
No. Of parameters	532
No. Of restraints	8
H-atom treatment	H atoms treated by a mixture of independent and constrained refinement
Δ ρ _{max} , Δ ρ _{min} (e Å ⁻³)	0.61, -0.74

Computer programs: CrysAlis PRO (Rigaku OD, 2018), SHELXS (Sheldrick, 2015a), SHELXL2014 (Sheldrick, 2015b), ORTEP-3 for Windows (Farrugia, 2012), DIAMOND (Brandenburg, 2006) and publCIF (Westrip, 2010).

The copper (II) centre in (1) is bis-N,O-chelated by two 2-(4,5-diphenyl-1H-imidazol-2-yl)-4-nitrophenolate monoanions. The resulting N₂O₂ donor set defines highly distorted coordination geometry, as seen in the angles included in Table 3.B.2 and Fig.3.B.4.

Table. 3.B.2. Selected geometric parameters of complex (1)

Selected geometric parameters (Å, °) of complex (1)			
Cu—O1	1.9291 (17)	Cu—N1	1.9586 (19)
Cu—O2	1.9304 (17)	Cu—N2	1.957 (2)
O1—Cu—O2	89.36 (7)	O2—Cu—N1	144.41 (8)
O1—Cu—N2	147.34 (8)	O2—Cu—N2	93.56 (7)
O1—Cu—N1	92.83 (8)	N1—Cu—N2	103.14 (8)

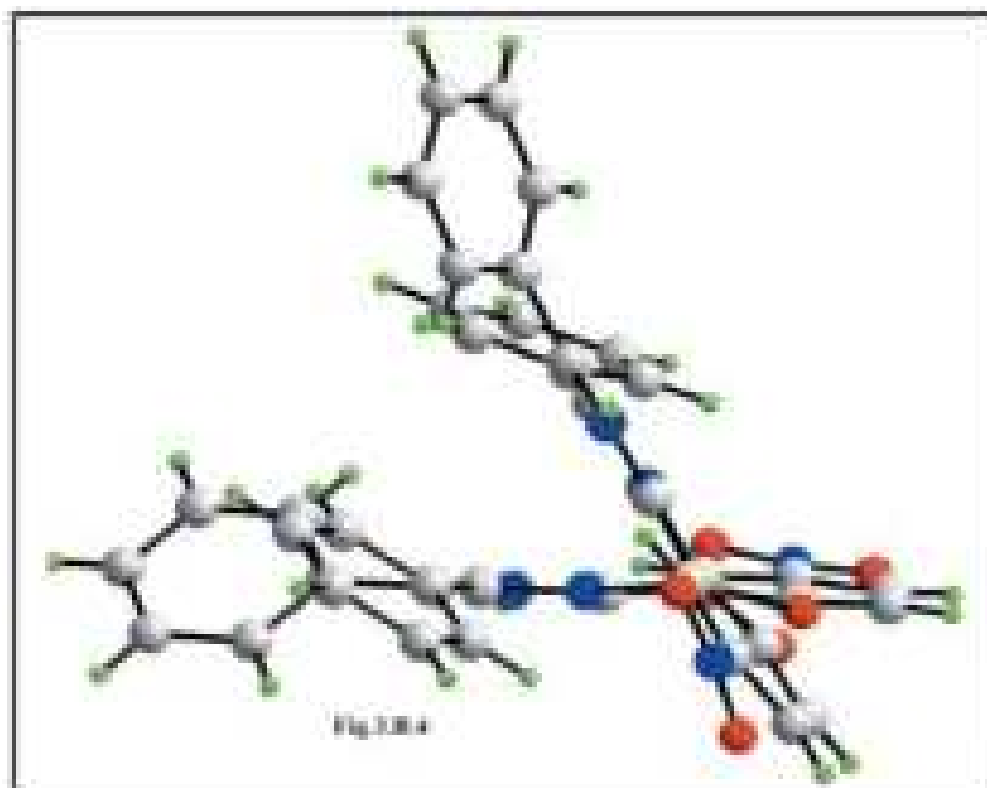


Fig. 3.B.4. A view of the molecular structure of the complex molecule in (1), highlighting the distorted coordination geometry about the copper (II) atom.

The angles range from a narrow 89.36 (7), for O1—Cu—O2, to a wide 147.34 (8), for O1—Cu—N2. The distortion is highlighted in the dihedral angle

between the best planes through the two chelate rings of 49.82 (7). The value of τ_4 is a geometric measure of the distortion of four-coordinate geometry²³. For (1), the value computes as 0.48 which is almost exactly intermediate between the values of $\tau_4 = 0$ for an ideal tetrahedron and $\tau_4 = 1.0$ for an ideal square-planar geometry. In fact, the six-membered chelate rings are not planar, each adopting an envelope conformation with the Cu atom being the flap atom. In this description, the r.m.s. deviation for the least-squares plane through the O1/N1/C1/C2 atoms is 0.036 Å with the Cu atom lying 0.410 (3) Å out of the plane. The comparable parameters for the O2-chelate ring are 0.033 and 0.354 (3) Å, respectively. The dihedral angle formed between the two planar regions of the chelate rings is 49.38 (8). The dihedral angles between the best plane through the O1- chelate ring and each of the fused six- and five-membered rings are 9.18 (12)° and 5.54 (14)°, respectively; the equivalent angles for the O2-chelate rings are 8.44 (8) and 2.71 (9)°, respectively. The N1-imidazol-2-yl ring forms dihedral angles of 41.20 (11) and 37.46 (10)° with the C10- and C16-phenyl substituents, respectively, and the dihedral angle between the 143 phenyl rings is 59.92 (8)°, i.e., all indicating splayed relationships. A similar situation pertains to the N2-imidazol-2-yl ring, where the comparable dihedral angles formed with the C31- and C37-phenyl rings are 38.29 (10)°, 48.5 (9)° and 50.84 (7)°, respectively. Finally, the nitro groups are not strictly coplanar with the benzene rings to which they are connected, as seen in the dihedral angles of 14.2 (4)° for C1–C6/N4/O3/O4 and 5.9(3) for C22–C27/N6/O5/O6.

3. B.2.3.2 Supramolecular features of complex (1)

As each component of the asymmetric unit has hydrogen bonding functionality, conventional hydrogen bonds are found in the crystal of (1); the geometric parameters characterizing the identified intermolecular interactions operating in the crystal of (1) are collated in Table 3.B.3. Each of the imidazolylamine- N—H atoms forms a donor interaction to a water molecule to generate a three-molecule aggregate. The O1W water molecule forms donor interactions to the coordinated O2 atom and to a symmetry-related O2W water molecule. The O2W water molecule connects to the coordinated O1 atom as well as to a nitro-O3 atom. Hence, the O2W water molecule is involved in four hydrogen-bonding interactions. The fourth contact involving the O1W water molecule, a C—H...O acceptor contact, is provided by the nitrobenzene ring. There is also a phenyl-C—H...O (nitro) contact of note, Table 3.B.3. The aforementioned interactions combine to stabilize a supramolecular layer lying parallel to (101), as shown in Fig. 3.B.4a. There are also π - π stacking and C—H...O interactions in the crystal, Fig. 3.B.4b. Within layers, there are π - π interactions occurring between the imidazolyl and nitrobenzene rings [intercentroid distances: Cg(N1/N3/C7–C9)...Cg(C1–C6) = 3.7452 (14) Å and angle of inclination = 9.70 (13)° for symmetry operation (-x + 2, -y + 1, -z + 1); Cg(N2/N5/C28–C30)...Cg(C22–C27) = 3.6647 (13) Å and angle of inclination = 8.15 (12)° for (-x + 1, -y + 1, -z + 1)]. The connections between layers along [010]

are of the type nitrobenzene-C—H...O (nitro) and phenyl-C—H.....(phenyl), as detailed in Table 3.B.3.

Table. 3.B.3. Hydrogen Bond geometry for complex (1)

Hydrogen bond geometry (Å, °)				
Cg1 is the ring centroid of the C16-C21 ring				
D-H...A144	D-H	H...A	D...A	D-H...A
N3—H3N...O1W ⁱ	0.89 (2)	1.91 (2)	2.790 (3)	173 (3)
N5—H5N...O2W144	0.88 (2)	1.95 (2)	2.822 (3)	172 (3)
O1W—H1W...O2144	0.85 (2)	1.92 (2)	2.745 (2)	164 (2)
O1W— H2W...O2W ⁱⁱ¹⁴⁴	0.85 (2)	2.21 (2)	2.868 (2)	134 (2)
O2W—H3W...O1 ⁱⁱ¹⁴⁴	0.84 (2)	2.01 (2)	2.841 (2)	172 (2)
O2W—H4W...O3 ⁱⁱⁱ¹⁴⁴	0.84 (2)	2.27 (2)	2.938 (2)	136 (2)
C3—H3...O1W ⁱ 144	0.95	2.57	3.435 (3)	151
C33—H33...O5 ^{iv}	0.95	2.48	3.345 (3)	151
C5—H5...O6 ^{v144}	0.95	2.50	3.361(3)	151
C34—H34...Cg1 ^{vi144}	0.95	2.49	3.426(3)	168

Symmetry codes: (i) $-x + 2; -y + 1; -z + 1$; (ii) $-x + 1; -y + 1; -z + 1$; (iii) $x - 1, y, z - 1$; (iv) $-x + 1, y + 1/2; -z + 1/2$; (v) $x + 1; y, z + 1$ (vi) $x, -y + 1/2; z - 1/2$.

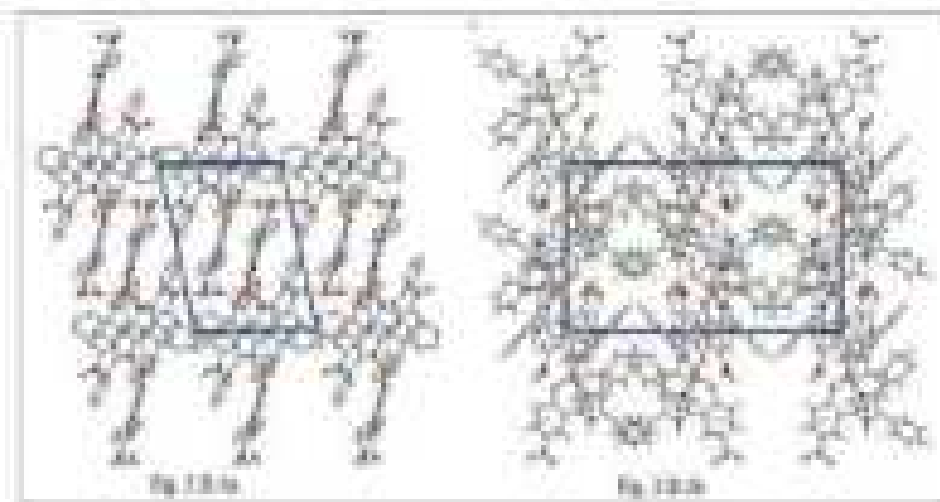


Fig. (3.B.4a-4b). The molecular packing in the crystal of (1): (3.B.4a) a supramolecular layer parallel to (101) sustained by O—H...O, N—H...O and C—H...O interactions shown as orange, blue and green dashed lines, respectively, and (3.B.4b) a view of the unit-cell contents in projection down the c axis, with π - π and C—H... π interactions shown as purple and pink dashed lines, respectively.

3.B.2.3.3 Hirshfeld surface analysis of complex (1)

The Hirshfeld surface calculations for (1) were performed with CrystalExplorer17 and published protocols²⁴ and serve to indicate the significant role of the two water molecules in the supramolecular association in the crystal. The involvement of both the water molecules in hydrogen bonds, Table 3.B.3, is evident as bright-red spots near the respective atoms on the Hirshfeld surfaces mapped over dnorm for the O1W-, Fig. 3B.5a, and O2W-water, Fig. 3B.5b, molecules. In addition, the presence of faint-red spots near the O1W, O2W and H1W atoms in Fig. 3B.5a and Fig. 3B.5b are indicative of the other contacts of these atoms with those of the Cu^{II} complex molecule (Table 3.B.3). The donors and acceptors of the hydrogen bonds involving atoms of the complex molecule are also apparent as bright-red spots near the participating atoms in the views of the Hirshfeld surfaces calculated for the complex molecule shown in Figs. 3B.(5c–5d). The presence of a short interatomic C...C contact between atoms C22 and C28 (Table 3.B.4) arises from π - π stacking between symmetry-related imidazole and nitrobenzene rings, and is observable as the faint-red spots near these atoms on the dnorm-mapped Hirshfeld surface in Fig.3.B.5c.

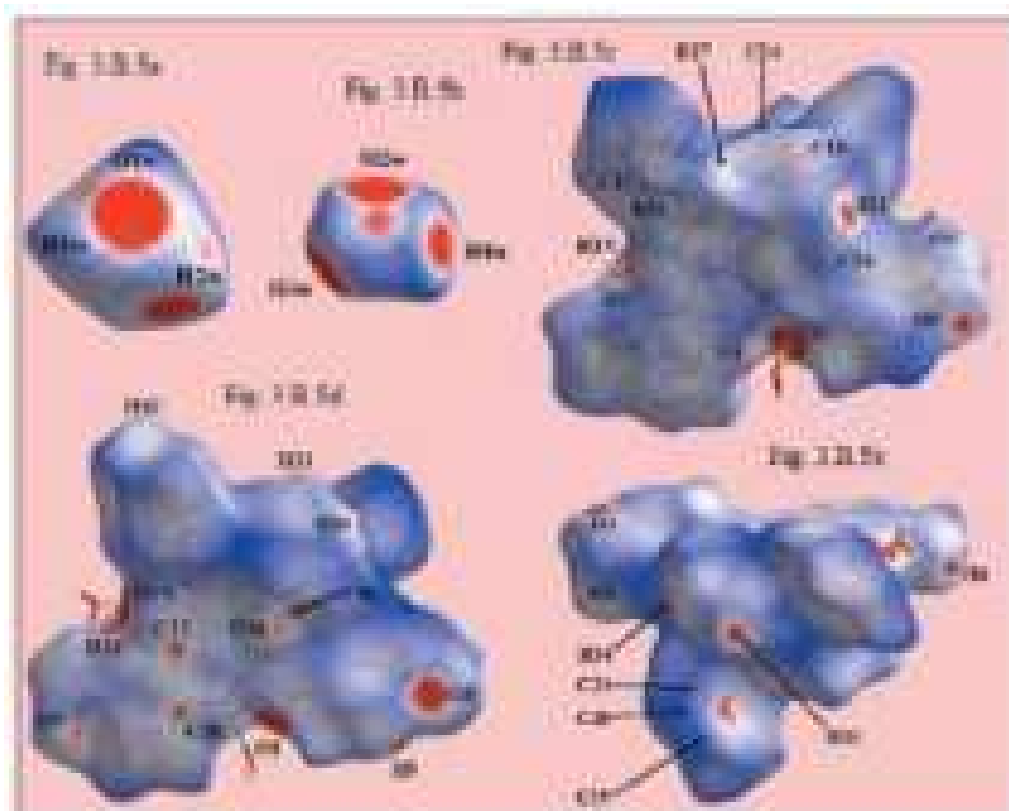


Fig. 3.B.5a-e. Different views of the Hirshfeld surfaces for the constituents of (I) mapped over dnorm for the (5a) water-O1W molecule [in the range -0.2369 to +1.2173 arbitrary units (au)], (5b) water-O2W molecule (-0.2114 to + 0.7500 au) and 5(c)–5(e) complex molecule (-0.1170 to + 1.6287 au).

Table 3.B.4. Summary of short interatomic contacts (Å) in complex (1)^a

Contact	Distance	Symmetry operation
H12...H12	1.92	-x+1, -y+1, -z+1
H1W...H3N	2.22	-x+2, -y+1, -z+1
H2W...H3N	2.26	-x+2, -y+1, -z+1
O4...H4O	2.54	x+1, -y+3/2, z+1/2
C1...H3W	2.74	-x+1, -y+1, -z+1
C6...O6	3.206(3)	-x+1, -y+1, -z+1
C12...H12	2.55	-x+1, -y+1, -z
C13...C25	3.347(3)	-x+1, -y+1, -z
C14...O5	3.197(3)	-x+1, -y+1, -z
H17...O6	2.55	-x+1, -y+1, -z
C19...H34	2.68	x, -y+3/2, z-1/2
C20...H34	2.60	x, -y+3/2, z-1/2
C21...H34	2.67	x, -y+3/2, z-1/2
C21...H2W	2.64	-x+2, -y+1, -z+1
C21...O1W	3.161(3)	-x+2, -y+1, -z+1
C22...C28	3.267(3)	-x+1, -y+1, -z+1
C36...O5	3.146(3)	-x+1, -y+1, -z+1
H36...O5	2.49	-x+1, -y+1, -z+1
C41...H20	2.76	-x+1, y, z

Notes: (a) the interatomic distances are calculated in CrystalExplorer17 whereby the X-H bond lengths are adjusted to their neutron values.

The pair of faint-red spots appearing near the phenyl-C36 and H36 atoms, and also near the nitro-O5 atom on the surface indicating short interatomic contacts that characterize the weak C—H...O interaction, (Table 3.B.4). The influence of the C—H... π contact on the molecular packing is recognized from the three faint-red spots in the phenyl-(C16–C21) ring and another near atom H34 in Fig.3.B.5e. The donors and acceptors of this interaction are also evident as the blue bump and a bright orange spot enclosed within the black circle on the Hirshfeld surface mapped with the shape-index property in Fig. 3.B.6a. The bright-orange region enclosed within a black circle in Fig.3.B.6b is also an indication of the O2W—H4W...Cg(C16–C21) contact. The Hirshfeld surfaces mapped over the calculated electrostatic potential for the water and complex molecules in Fig.3.B.7a-7c also illustrate the donors and acceptors of intermolecular interactions through blue and red regions corresponding to positive and negative electrostatic potentials, respectively. The π – π stacking between symmetry-related imidazolyl and nitrobenzene rings are viewed as the flat regions enclosing them on the Hirshfeld surfaces mapped over curvedness in Fig.3.B.8a-8b.

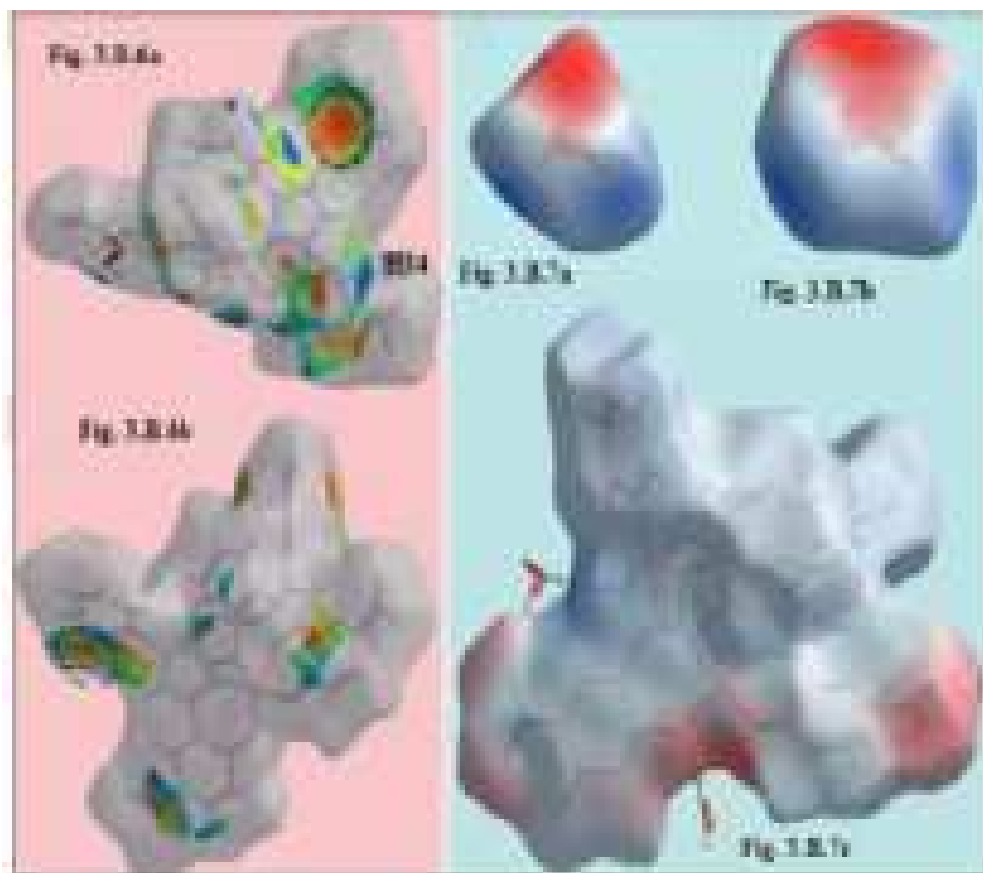


Fig. 3.B.6a-b. Two views of the Hirshfeld surface mapped with the shape-index property for the complex molecule in (1) from -1.0 to $+1.0$ arbitrary units highlighting (a) the donor and acceptor atoms of the C—H... π interaction through a blue bump near the H34 atom and bright-orange curvature, enclosed within the black circle, and (b) the O2W—H4W... π interaction by the bright-orange region enclosed within the black circle.

Fig. 3.B.7a-c. Different views of the Hirshfeld surfaces for the constituents of (1) mapped over the electrostatic potential (the red and blue regions represent negative and positive electrostatic potentials, respectively) for the (a) water-O1W molecule [in the range -0.1001 to $+0.1943$ atomic units (a.u.)], (b) water-O2W molecule (-0.1013 to $+0.1751$ a.u.) and (c) complex molecule (-0.1209 to $+0.2076$ a.u.). The hydrogen bonds involving water molecules in (c) are indicated by green dashed lines.

On the Hirshfeld surfaces mapped over d_{norm} illustrated in Figs. 3.B.5c–5e, faint-red spots also appear near other atoms indicating their involvement in other short interatomic contacts, as summarized in (Table 3.B.4). The Hirshfeld surfaces also provide an insight into the distortion in the coordination geometry

formed by the N_2O_4 donor set about the copper(II) centre in the complex molecule. This is performed by considering the Hirshfeld surface about the metal centre alone²⁵. The distortion in the coordination geometry is observed on the Hirshfeld surface mapped with the shape-index property as the bright orange patches of irregular shape covering a major region for the Cu—O bonds in Fig. 3.B.9a and the small orange regions on the surface relatively far from the Cu—N bonds in Fig. 3.B.9b. The different curvature of the Hirshfeld surfaces coordinated by the N_2O_4 donor set in Figs. 3.B.9c and 3.B.9d also support this observation.

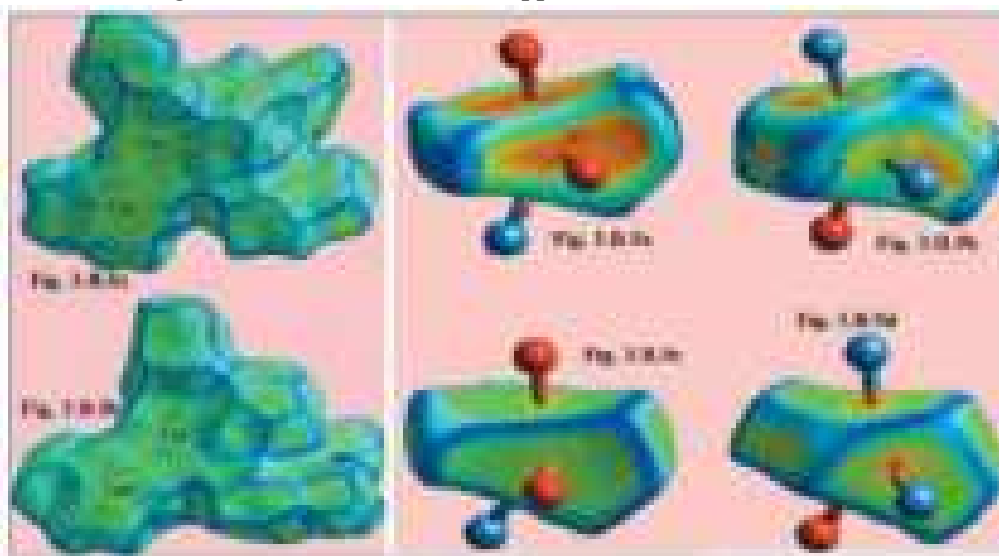


Fig. 3.B.8a-b. Two views of the Hirshfeld surface mapped over curvedness for the complex molecule in (1), highlighting flat regions enclosing symmetry related imidazole and nitrobenzene rings involved in π - π stacking, labelled Cg1 and Cg3 for one pair of rings in (a), and Cg2 and Cg4 for the other pair in (b).

Fig. 3.B.9a-d: Different views of the Hirshfeld surfaces calculated for the copper(II) centre in (I) highlighting the coordination by the N_2O_4 donor set mapped over (a)/(b) shape-index in the range -1.0 to +1.0 arbitrary units and (c)/(d) curvedness in the range -4.0 to +0.4 arbitrary units.

The Cu—O and Cu—N bonds are rationalized in the two-dimensional fingerprint plot taking into account only the Hirshfeld surface for the copper atom shown in **Fig. 3.B.10**. The distribution of points in the fingerprint plot through the pair of aligned red points at different inclinations from $d_e + d_i \approx 2.0 \text{ \AA}$ for the Cu—N bonds (upper region) and the Cu—O bonds (lower region) are indicative of the distorted geometry.

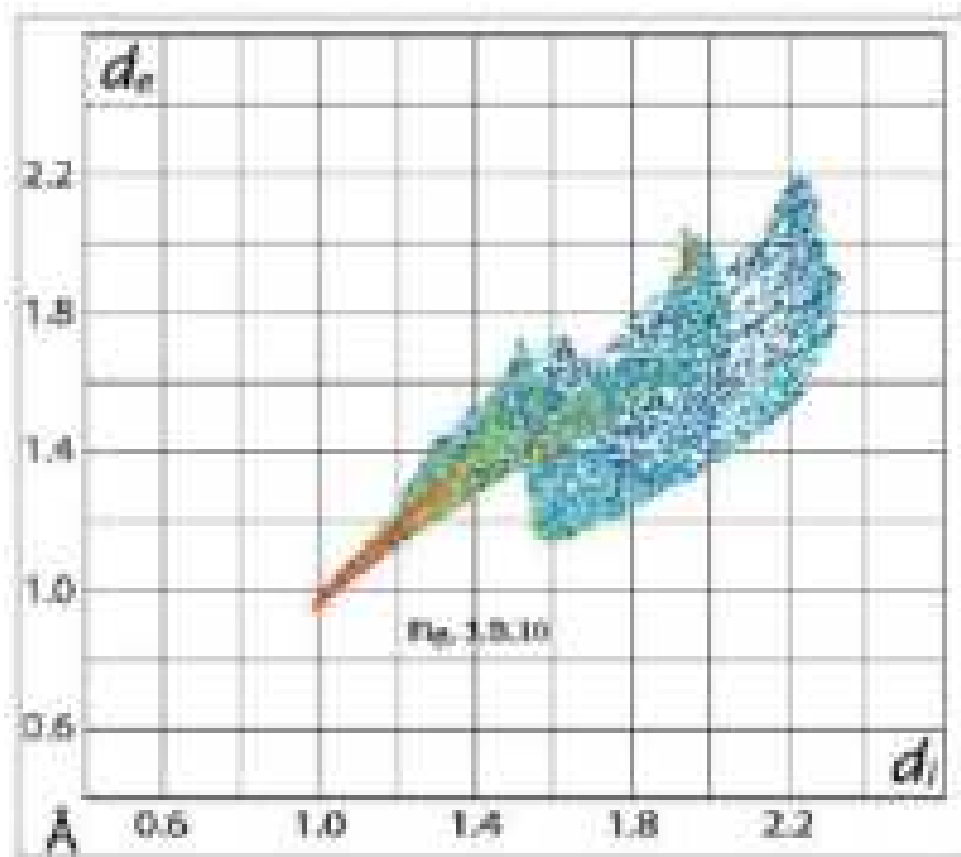


Fig. 3.B.10. The two-dimensional fingerprint plot taking into account only the Hirshfeld surface calculated about the copper(II) atom.

The overall two-dimensional fingerprint plot for (1), i.e. the entire asymmetric unit, Fig.3.B.11(a), and those delineated into H...H, O...H/H...O, C...H/H...C, C...C and C...O/O...C contacts are illustrated in Figs.3.B.11(b)–(f), respectively. The percentage contributions from different interatomic contacts to the Hirshfeld surfaces of the complex molecule and for overall (1) are summarized in Table 3.B.5. The presence of water molecules in the crystal of (1) increases the percentage contribution from O...H/H...O contacts (**Table 3.B.5**) to the Hirshfeld surface of the asymmetric unit compared with the complex molecule alone.

Table 3.B.5. Percentage contributions of interatomic contacts to the Hirschfeld surface for the complex in (I) and overall (II)

Contact	Percentage contribution	
	Complex molecule	(I)
H...H	41.3	41.0
O...H/H...O	25.6	27.1
C...H/H...C	19.8	19.6
C...C	3.5	3.3
C...O/O...C	3.4	3.2
C...N/N...C	2.8	2.7
N...H/H...N	2.2	2.1
O...O	0.6	0.5
N...O/O...N	0.2	0.2
Cu...O/O...Cu	0.0	0.3
Cu...C/C...Cu	0.3	0.0

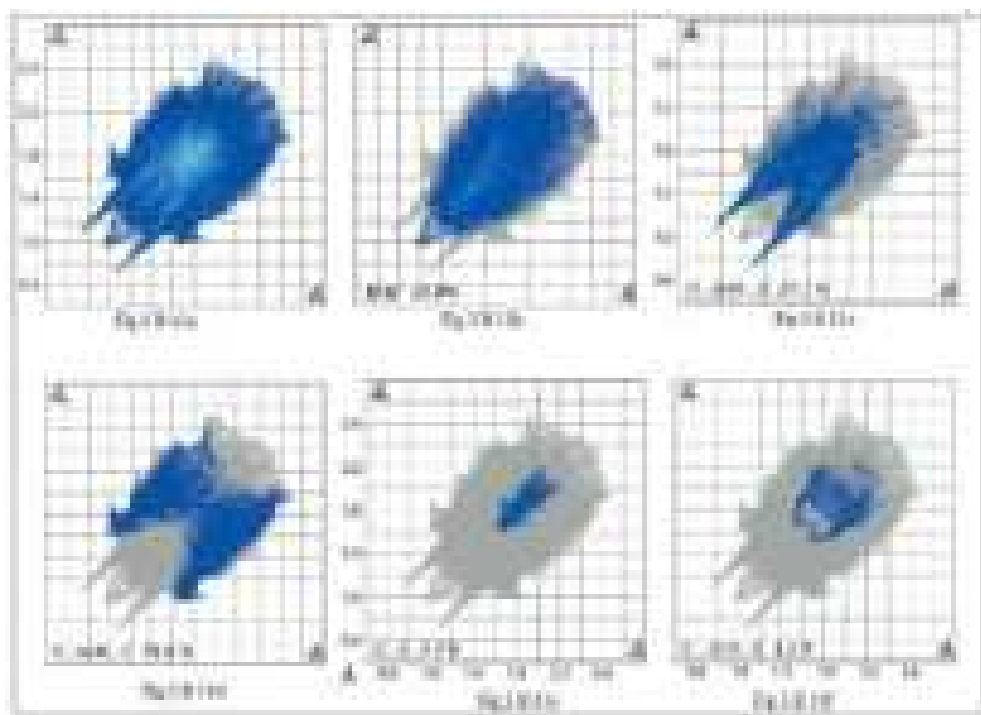


Fig. 3.B.11a-f. (a) A comparison of the full two-dimensional fingerprint plot for (1) and those delineated into (b) H...H, (c) O...H/H...O, (d) C...H/H...C, (e) C...C and (f) C...O/O...C contacts.

This results in slight decreases in the percentage contributions from other interatomic contacts for (1) (Table 3.B.5). A single conical tip at $d_e + d_i \approx 1.9 \text{ \AA}$ in the fingerprint plot delineated into H...H contacts shown in Fig.3.B.11 (b) is the result of the involvement of the H12 atom in a short interatomic H...H contact, Table 3.B.4. The points due to short interatomic contacts between amine hydrogen-H3N and water hydrogen atoms, H1W and H2W, Table 3.B.4 are merged within the plot. Although the molecular packing of (1) is influenced by several intermolecular O—H...O and C—H...O interactions, the presence of a pair of long spikes at $d_e + d_i \approx 1.8 \text{ \AA}$ in the plot delineated into O...H/H...O contacts, Fig.3.B.11(c), arise from the N—H...O hydrogen bond, while the merged points correspond to other interactions at greater interatomic distances. The significant contribution from interatomic C...H/H...C contacts (Table 3.B.5) to the Hirshfeld surface of (1) reflect the combined influence of intermolecular C—H... π interactions (Table 3.B.4) and the short interatomic C...H/H...C contacts, summarized in Table 3.B.4, and viewed as the distribution of points in the form of characteristic wings in Fig.3.B.11d. The presence of short interatomic C...C contacts are evident as the points near a rocket shape tip at $d_e + d_i \approx 3.2 \text{ \AA}$ in the respective delineated fingerprint plot, Fig.3.B.11e, while the points corresponding π - π stacking between the imidazole and nitrobenzene rings are distributed about $d_e = d_i = 1.7 \text{ \AA}$ in the plot. The small, i.e. 2.7%, contribution from C... N/N...C contacts to the surface is also due to these π - π stacking interactions (delineated plot not shown). The contribution of 3.2% from C...O/O...C contacts is due to the presence of short interatomic contacts involving nitro-O atoms, Table 3.B.4, and are apparent as the pair of parabolic tips at $d_e + d_i \approx 3.2 \text{ \AA}$ in the delineated plot of Fig.3.B.11f. The contribution from other interatomic contacts to the surface summarized in Table 3.B.5 has negligible influence on the molecular packing.

3. B.2.3.2 Crystal structure of Copper acetate monohydrate ($\text{Cu}_2\text{C}_8\text{H}_{16}\text{O}_{10}$) (2)

The compound copper acetate monohydrate (2) was obtained as a by-product of the reaction between the catalyst CuB_4O_7 and NH_4OAc during the synthesis of 2,4,5-triarylimidazole derivatives under the solvent free condition. After successful single crystal diffraction study, its structure has been compared with the reported structure²². A detail of crystallographic data (crystal parameters, data collection and refinements) of the Compound (2) is given in Table 3.B.6. The atomic numbering scheme along with the atom connectivity for compound (2) is shown in Fig.3.B.12a-12b. Single crystal X-ray analysis revealed that the compound (2) crystallizes in the monoclinic crystal system with space group C2/c and the crystallographic parameters are $a=13.0799(8) \text{ \AA}$, $[13.167 (4) \text{ \AA}]^{22}$, $b=8.5056(4)\text{\AA}$, $[8.563 (2) \text{ \AA}]^{22}$, $c=13.7429(7)\text{\AA}$, $[13.862 (7) \text{ \AA}]^{22}$, $\beta=116.887(7)^\circ$, $[117.019 (2)^\circ]^{22}$ $\alpha=\gamma=90^\circ$ and $Z = 4$.

Table. 3.B.6. Crystal data collection and structure refinement for compound (2)

Crystal data	
Moiety formula, Chemical formula	Cu ₂ C ₈ H ₁₆ O ₁₀ , Cu ₂ (O ₂ CCH ₃) ₄ . 2H ₂ O
Formula weight	399.31
Crystal system, Space group	Monoclinic, C 2/c
Colour, Size, mm	Blue, 0.24 × 0.22 × 0.20
Unit cell dimensions	
a, b, c	13.0799 (8) Å, 8.5056(4) Å, 13.7429(7) Å
α, β, γ	90°, 116.887(7)°, 90°
Volume Å ³ , Z	1363.65(13), 4
Density (calculated), Mg/m ³	1.945
Absorption coefficient, mm ⁻¹	3.164
F(000)	808
Data collection	
Temperature, K	119.98(10)
Theta range for data collection	2.96° to 29.01°
Index ranges	-17 ≤ h ≤ 17, -11 ≤ k ≤ 10, -18 ≤ l ≤ 17
Reflections collected	8716
Unique reflections	1660
Observed reflections (>2σ(I))	1438
R _{int}	0.0387
Completeness to θ, %	29.01°, 91.1
Absorption correction	Multi-scan (Rigaku Oxford Diffraction, 2017) $T_{\min} = 0.473$, $T_{\max} = 0.531$
Refinement	
Refinement method	Full-matrix least-squares on F^2
Data / restraints / parameters	1660 / 0 / 101
Goodness-of-fit on F^2	1.052
Final R indices [I > 2σ(I)]	$R_1 = 0.0266$, $wR_2 = 0.0582$
R indices (all data)	$R_1 = 0.0328$, $wR_2 = 0.0603$
Largest diff. peak and hole	0.532 and -0.566 e.Å ⁻³

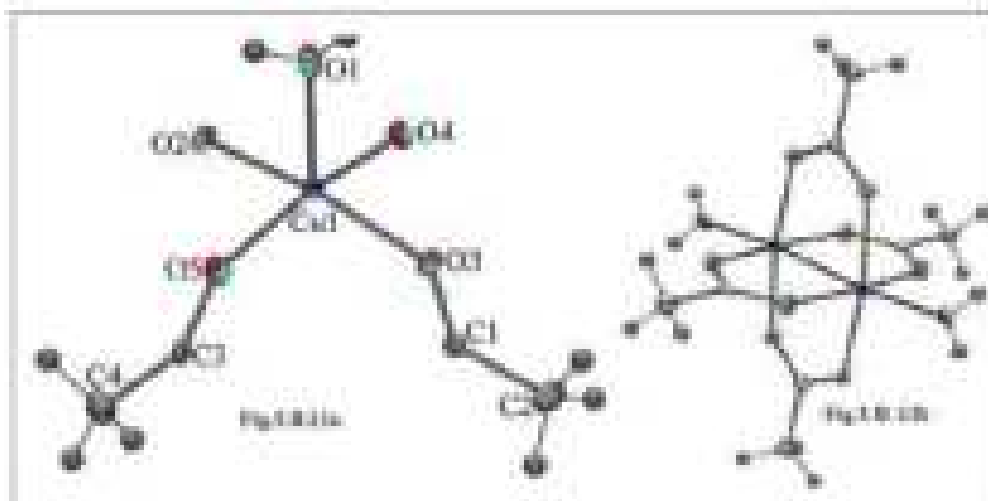


Fig. 3.B.12a-b. a) Asymmetric unit of compound (2) and b) ortep diagram of (2) with 50% probability

As evident from Fig.3.B.12b, The two copper ions are bridged symmetrically by four acetates in a centrosymmetric dimeric unit and two waters coordinate along the Cu-Cu axis and assumes paddle wheel structure in which the Cu-Cu distance is about 2.6118 (5) Å (Cu-Cu distance in metallic copper, 2.556Å). The selected bond lengths (Å) and bond angles (°) for compound (2) is listed in Table 3.B.7.

Table. 3.B.7. The selected bond lengths (Å) and bond angles (°) for compound (2)

Bond lengths (Å)			
Cu(1)-Cu(1) ⁱ	2.6118(5)	Cu(1)-O(3)	1.9847(15)
Cu(1)-O(1)	2.1411(17)	Cu(1)-O(4)	1.9415(15)
Cu(1)-O(2)	1.9907(15)	Cu(1)-O(5)	1.9559(15)
<i>Symmetry Code: (i) -x+1, -y+1, -z+1</i>			
Bond angles (°)			
O(2)-Cu(1)-O(1)	92.58(7)	O(4)-Cu(1)-O(2)	90.29(6)
O(3)-Cu(1)-O(1)	98.35(7)	O(5)-Cu(1)-O(2)	89.42(6)
O(4)-Cu(1)-O(1)	97.28(7)	O(4)-Cu(1)-O(3)	87.20(6)
O(5)-Cu(1)-O(1)	93.52(7)	O(5)-Cu(1)-O(3)	91.06(6)

The Cu(1)-O(1) and Cu(1)-O(2) bond distances in the complex (2) are 2.1411 (17) Å and 1.9907(15) Å respectively. Similarly, Cu(1)-O(3), Cu(1)-O(4) and Cu(1)-O(5) bond distances are 1.9847(15), 1.9415(15) and 1.9559(15) respectively. Hydrogen bonding pattern and hydrogen bonding geometrical parameters in compound (2) is shown in Fig.3.B.13 and Table 3.B.8 respectively.

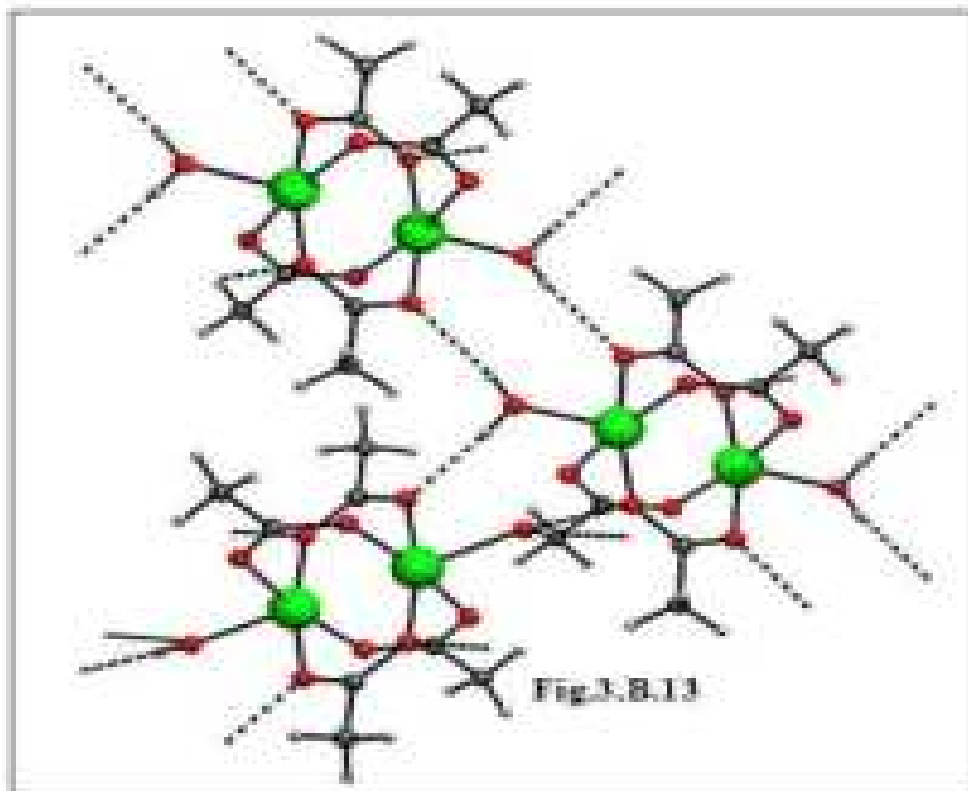


Fig. 3.B.13. Hydrogen bonding pattern in compound (2)

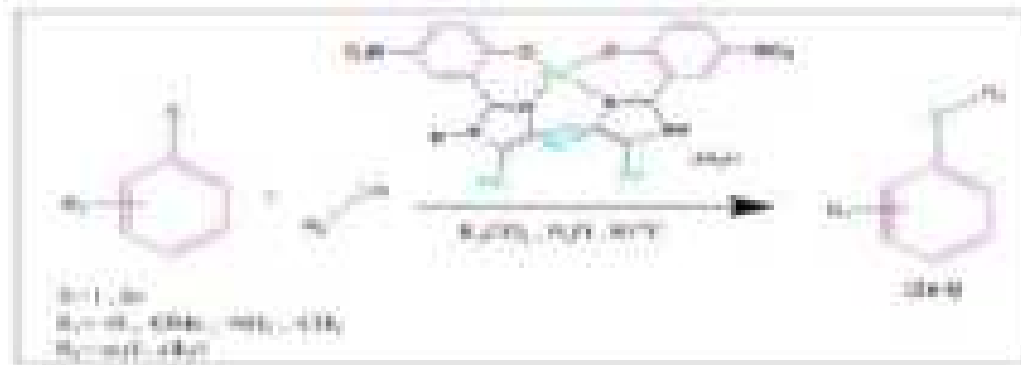
Table. 3.B.8. Hydrogen bonded geometries in compound (2)

Bond	D - H	H···A	D···A	D - H···A
O(1)-H(1A)···O(3) ⁱⁱⁱ	0.73(3)	2.16(3)	2.892(3)	171(3)
O(1)-H(1B)···O(2) ^{iv}	0.77(3)	2.02(3)	2.786(2)	175(4)
C(4)-H(4A)···O(5) ^v	0.96	2.58	3.522(3)	168

Symmetry Code: (iii) -1/2-x, 1/2-y, -z; (iv) -x, y, 1/2-z; (v) 1/2+x, 1/2+y, z

3.B.2.4 Catalytic activity of Bis[2-(4,5-diphenyl-1H-imizol-2-yl)-4-nitrophenolato] copper (II) dihydrate (1) towards C–S cross coupling reaction

We employed the complex (1) to study the efficacy for the C–S cross coupling reaction under the green condition as because C–S cross-coupling reaction is one of the most promising approaches for the synthesis of valuable pharmaceutical as well as industrially important compounds^{26,27}. Thus, we designed our reaction by employing aryl halides and aryl thiols under green condition using water as a reaction medium and complex (1) as a catalyst to synthesize C–S cross-coupled products (2a-t)²⁸(Scheme 3.B.2).



Scheme. 3.B.2. C-S cross-coupling between aryl halide and aryl thiols using complex (1) as a catalyst.


Initially, in order to explore the catalytic efficacy of newly synthesized complex (1), we set up a model reaction for C-S coupling by employing 4-iodoanisole (1mmol), thiophenol (1mmol), K₂CO₃ (1.2mmol) with different amount (mg) of catalyst (1) in different solvent medium under refluxing condition. The optimized result of the catalyst loading and selection of solvent for the model reaction is summarized in Table 3.B.9 and Table 3.B.10 respectively.

Table 3.B.9. Optimization of catalyst loading^a

Entry	Catalyst (mg)	Yield (%) ^b
1	2	60
2	4	65
3	6	72
4	8	85
5	10	96
6	12	97

^areaction condition: 4-iodoanisole (1mmol), thiophenol (1mmol), K₂CO₃ (1.2mmol) at 80°C.

^byield.

Table.3.B.10. Optimization of reaction parameters for the C-S coupling reaction^a


Entry ^a	Catalyst(mg)	Time (h)	Solvent (5ml)	Base	Temperature (°C)	Yield ^b (%)
1	10	10	DMF	K ₂ CO ₃	80	90
2	10	10	DMSO	K ₂ CO ₃	80	87
3	10	10	CH ₃ CN	K ₂ CO ₃	80	90
4	10	10	Toulene	K ₂ CO ₃	80	92
5	10	10	Ethanol	K ₂ CO ₃	80	91
6	10	10	H₂O	K₂CO₃	80	96
7	10	10	H ₂ O	K ₂ CO ₃	100	97
8	10	10	H ₂ O	K ₂ CO ₃	60	40
9	10	10	H ₂ O	K ₂ CO ₃	RT	Nil
10	Nil	24	H₂O	K₂CO₃	80	Nil
11	10	10	H ₂ O	Cs ₂ CO ₃	80	97
12	10	10	H ₂ O	KO ^t Bu	80	60
13	10	10	H ₂ O	Et ₃ N	80	62
14	10	10	H ₂ O	KOH	80	70

^areaction condition: 4-iodoanisole (1mmol), thiophenol (1mmol), K₂CO₃ (1.2mmol) at 80°C,

^byield, **Nil** stands for in absence of catalyst as well as no yield of the desired product.

From the optimized model reaction, it was evident that C-S coupled product formed efficiently (96%) when the amount of catalyst loading is 10 mg (0.09 mol %) in aqueous medium (Table 3.B.10, entry 6). Also, we carried out the control reaction under the same condition without catalyst and we observed that the C-S coupled product did not form in absence of the catalyst (Table 3.B.10,

entry 10). Therefore, it may be concluded that the reaction did not proceed in absence of the catalyst.

To check the generality and efficacy of catalyst (1) for C–S cross-coupling reaction, we extended this protocol with a variety of haloarenes and aliphatic as well as aromatic thiols and interestingly, we found that the C-S coupled product (2a-t) formed in excellent yield under the optimized reaction condition and it is depicted in Fig.3.B.13.

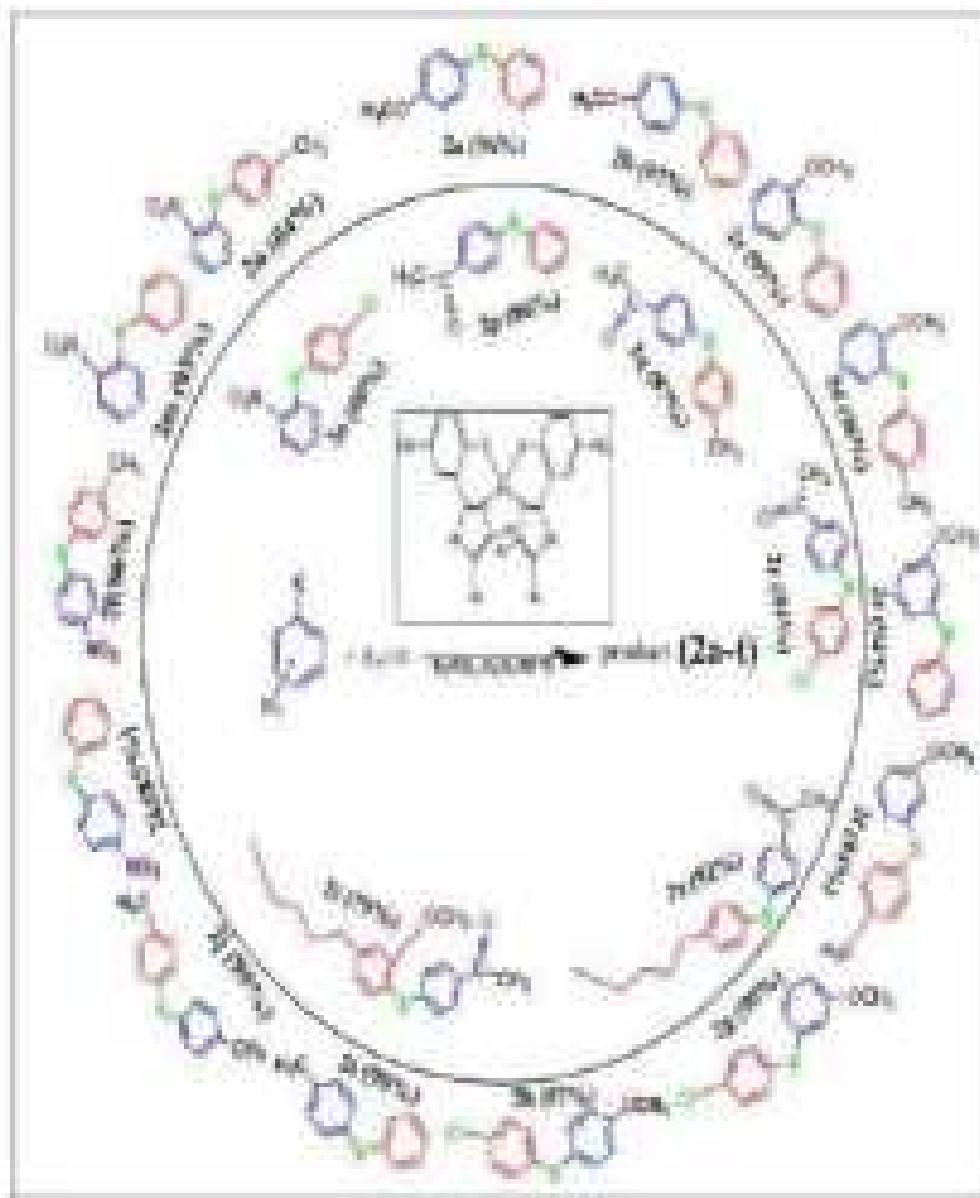


Fig. 3.B.14. C-S coupled product (2a-t)

Thus, from the present investigation, it was evident that the complex (1), Bis[2-(4,5-diphenyl-1H-imizol-2-yl)-4-nitro-phenolato] copper(II) dihydrate has shown excellent catalytic efficiency for the synthesis of C-S cross-coupled reaction under green reaction condition and therefore, giving an excellent yield of the desired C-S coupled product in water.

3. B.3. Experimental section

3. B.3.1 Materials and methods:

All the starting chemicals of high purity for the present investigation were procured commercially and were used as received. The FT-IR spectra of the synthesized products were recorded in Bruker Alpha III spectrophotometer operating in the wave number region 4000 to 400 cm^{-1} in dry KBr. Single crystal X-ray diffraction study was carried out with XtaLAB Synergy, Dualflex AtlasS2 diffractometre and Diffraction data was collected using monochromatic Cu $K\alpha$ radiation for complex (1) and Mo $K\alpha$ radiation for compound (2) respectively with the ω and ϕ scan technique (CrysAlis PRO, Rigaku OD, 2017 & 2018). The structure was solved by direct method and was refined by full matrix least squares based on F^2 using SHELXL 2014 & SHELXL 97^{29,30}. All the H atoms were localized from the difference electron-density map and refined isotropically. ORTEP-plot and packing diagram were generated with ORTEP-3 for Windows³¹ and PLATON³². The Hirshfeld surface calculations for complex (1) were performed with *CrystalExplorer17*³³.

3.B.3.2 Synthesis of Bis[2-(4,5-diphenyl-1H-imizol-2-yl)-4-nitro-phenolato] copper(II) dihydrate (1)

In a typical procedure, benzil (0.3 g, 1 mmol), ammonium acetate (0.19 g, 2.5 mmol), 2-hydroxy-5-nitrobenzaldehyde (0.167 g, 1 mmol) and copper (II) borate (0.218 mg, 1 mmol) were ground in an agate mortar with a pestle and the reaction mixture was ground again for 30 min. The whole reaction mixture was then transferred to a 100 ml round-bottomed flask and heated at 100°C with constant stirring for 4 h. The reaction mixture was then extracted with dry acetone and dried over MgSO_4 . After a few days, a dark-brown solid was obtained. The product was recrystallized from dry dimethylformamide and, after 5 d, light-blue crystals of (I) were obtained (yield 60%; m.p. >300°C). IR (cm^{-1}) ν_{max} =3430 (O-H Stretching of H_2O), 3065 (N-H Stretching), 1578 (C=N Stretching), 1487, 1135 (C-H Stretching), 466 (Cu-N Stretching).

3.B.4 Conclusion

The title copper (II) complex, Bis[2-(4,5-diphenyl-1H-imidazol-2-yl)-4-nitrophenolato] copper (II) dihydrate (1) was isolated during an ongoing research programme on the catalytic activity of copper borate (CuB_4O_7) for C—N heterocyclic bond formation reactions. Complex (1) was formed during the attempted synthesis of a triarylimidazole derivative using benzil and the respective aromatic aldehyde with copper borate, using ammonium acetate as a nitrogen source. The single-crystal analysis of the synthesized product revealed that in the copper (II) complex, the triarylimidazole moiety acts as a bidentate ligand for the copper atom. During the successful synthesis of the triarylimidazole, the desired product formed in good yield at a temperature in the range 80°C. However, when the reaction was conducted at and above 100 °C the title copper (II) complex formed instead of the targeted triarylimidazole. The crystal and molecular structures of (1) are described herein, along with a detailed analysis of the molecular packing via an analysis of the calculated Hirshfeld surfaces. Again, the transformation of catalyst CuB_4O_7 into the Copper acetate monohydrate in the presence of NH_4OAc during the synthesis of 2,4,5-triarylimidazole has been explored and this fact is supported from the single crystal x-ray analysis of the compound (2). Also, the catalytic efficiency of the complex (1) has been explored for the C-S coupling reaction using aryl halide and aryl thio compounds under green reaction condition.

3.B.5 References

- (1) B. Valeur, I. Leray., *Coordination Chemistry Reviews*, **2000**, 205 (1), 3–40.
- (2) Y. Gabe, Y. Urano, K. Kikuchi, H. Kojima, T. Nagano., *J Am Chem Soc*, **2004**, 126 (10), 3357–3367.
- (3) S. L. Wiskur, H. Ait-Haddou, J. J. Lavigne, E. v. Anslyn., *Accounts of Chemical Research*, **2001**, 34 (12), 963–972.
- (4) E. L. Que, D. W. Domaille, C. J. Chang., *Chemical Reviews*, **2008**, 108 (5), 1517–1549.
- (5) E. L. Que, D. W. Domaille, C. J. Chang., *Chemical Reviews*, **2008**, 108 (10), 4328.
- (6) B. Sarkar., In *Metal Ions in Biological Systems Vol. 12 (Chap. 6 - Transport of Copper)*; Siegel, H., Siegel, A., Dekker, M., Eds.; New York, **1981**; pp 233–281.
- (7) F. M. Raymo., *Advanced Materials*, **2021**, 14 (6), 401–414.
- (8) D. J. Faulkner., *Natural Product Reports*, **2000**, 17 (1), 7–55.
- (9) J. Z. Ho, R. M. Mohareb, J. H. Ahn, T. B. Sim, H. Rapoport., *Journal of Organic Chemistry*, **2003**, 68 (1), 109–114.
- (10) A. R. Katritzky, C. W. Rees, E. F. V. Scriven., In *Comprehensive Heterocyclic Chemistry II, Vol. 2 (Chap 4.02 - Imidazoles)*; Katritzky, A. R., Rees, C. W., Scriven, E. F. V., Eds.; Oxford: New York, Pergamom, **1996**; pp 77–220.
- (11) L. de Luca., *Current Medicinal Chemistry*, **2006**, 13 (1), 1–23.
- (12) P. M. Colman, H. C. Freeman, J. M. Guss, M. Murata, V. A. Norris, J. A. M. Ramshaw, M. P. Venkatappa., *Nature*, **1978**, 272 (5651), 319–324.
- (13) E. I. Solomon, D. E. Heppner, E. M. Johnston, J. W. Ginsbach, J. Cirera, M. Qayyum, M. T. Kieber-Emmons, C. H. Kjaergaard, R. G. Hadt, L. Tian., *Chemical Reviews*, **2014**, 114 (7), 3659–3853.
- (14) M. Andersson, J. Hedin, P. Johansson, J. Nordström, M. Nydén., *Journal of Physical Chemistry A*, **2010**, 114 (50), 13146–13153.
- (15) V. Pascanu, G. González Miera, A. K. Inge, B. Martín-Matute., *J Am Chem Soc*, **2019**, 141 (18), 7223–7234.
- (16) Y. Li, R. T. Yang., *Langmuir*, **2007**, 23 (26), 12937–12944.
- (17) Q. Wang, Q. Gao, A. M. Al-Enizi, A. Nafady, S. Ma., *Inorganic Chemistry Frontiers*, **2020**, 7 (2), 300–339.

- (18) C. Chen, W. Zhang, J. Cong, M. Cheng, B. Zhang, H. Chen, P. Liu, R. Li, M. Safdari, L. Kloo, L. Sun., *ACS Energy Letters*, **2017**, 2 (2), 497–503.
- (19) S. S. Nadar, V. K. Rathod., *International Journal of Biological Macromolecules*, **2018**, 120 (Part B), 2293–2302.
- (20) S. Charoensuk, J. Tan, M. Sain, H. Manuspiya., *Nanomaterials*, **2021**, 11 (9), 2281.
- (21) S. Chettri, D. Brahman, B. Sinha, M. M. Jotani, E. R. T. Tiekink., *Acta Crystallographica*, **2019**, E75 (11), 1664–1671.
- (22) G. M. Brown, R. Chidambaram., *Acta Crystallographica*, **1973**, B29 (11), 2393–2403.
- (23) L. Yang, D. R. Powell, R. P. Houser., *Dalton Transactions*, **2007**, Issue 9, 955–964.
- (24) S. L. Tan, M. M. Jotani, E. R. T. Tiekink., *Acta Crystallographica*, **2019**, E75 (3), 308–318.
- (25) C. B. Pinto, L. H. R. dos Santos, B. L. Rodrigues., *Acta Crystallographica*, **2019**, C75 (Part 6), 707–716.
- (26) D. Das., *ChemistrySelect*, **2016**, 1 (9), 1959–1980.
- (27) S. V. Ley, A. W. Thomas., *Angewandte Chemie International Edition*, **2003**, 42 (44), 5400–5449.
- (28) R. Singha, S. Chettri, D. Brahman, B. Sinha, P. Ghosh., *Molecular Diversity*, **2022**, 26 (1), 505–511.
- (29) G. M. Sheldrick., *Acta Crystallographica*, **2015**, C71 (1), 3–8.
- (30) G. M. Sheldrick., *SHELXS-97 and SHELXL-97, Program for Crystal Structure Solution and Refinement*; University of Gottingen, Gottingen, **1997**.
- (31) L. J. Farrugia., *Journal of Applied Crystallography*, **1997**, 30 (5), 565–565.
- (32) A. L. Spek., *Acta Crystallographica*, **2009**, D65 (2), 148–155.
- (33) P. R. Spackman, M. J. Turner, J. J. McKinnon, S. K. Wolff, D. J. Grimwood, D. Jayatilaka, M. A. Spackman., *Journal of Applied Crystallography*, **2021**, 54 (3), 1006–1011.

CHAPTER-III

Section-C

DFT, Molecular Docking and Pharmacokinetic study of some selected 2, 4, 5-triarylimidazole derivatives

3.C.1 Background of the present investigation

Imidazole scaffold, an important heterocyclic compound is ubiquitous in nature and found in many natural products¹. Among a large variety of organic compounds containing imidazole core, 2, 4, 5-triarylimidazole occupies a special position as these scaffolds are recognized to show a diverse range of biological and pharmacological properties². These five membered organic heterocyclic scaffolds not only find application in biological and medicinal field but also finds many applications in analytical and industrial fields³. Substituted imidazole derivatives have good binding affinity with different metals present in various biological active sites and also found to exhibit good inhibitory activity against glucagon receptor antagonists⁴, inhibitors of P38 MAP kinase⁵, B-Raf kinase⁶ etc. Apart from the biological activities, substituted imidazole derivatives found to possess several other applications such as corrosion inhibitors⁷, optoelectric⁸, metal sensing⁹, fluorescent probe¹⁰ and biological imaging¹¹. Because of the wide application of substituted imidazole derivatives, it has drawn a considerable attention of the synthetic, medicinal and theoretical chemist during the past few decades¹². Moreover, computational study now a days has reached a stage whereby new scientific information about the target molecule could be easily generated and may enable the researcher to explore the new properties of the compounds under investigation¹³. Interestingly, Density functional Theory (DFT) helps in analyzing and predicting the structures, dipole moment, vibration frequencies, optical properties and thermodynamic properties of organic compounds with high accuracy¹⁴. On the other hand, computer aided drug design process (Molecular docking and Molecular dynamics) may enable the chemist to determine the desired properties in the drug molecule for making the process and discovery of new therapeutic agents more efficient and economical^{15,16}. Basically, structure-based drug design and ligand-based drug design approaches are the two fundamental categories of Computer Aided Drug Design process and both approaches have been widely employed in the modern drug discovery processes for the identification of suitable and specific target drug molecules. Thus, Computer Aided Drug Design enables the researchers to understand the different types of interaction prevailing between the ligand and the active site of the protein¹⁷. Furthermore, Diabetes mellitus or hyperglycemia is a chronic metabolic disorder caused by either insulin deficiency or insulin resistance is a global concern now a days¹⁸. A numerous synthetic therapeutic measures are available for the treatment or management of diabetes yet they are not the permanent measure to cure the

diabetes as they have unwanted side effects¹⁹. Therefore, finding an excellent therapeutic agent for the treatment and cure of above mention disorder is a challenging task and during the past few decades researchers are engaged in testifying different therapeutic agents to cure for diabetes²⁰. In modern day drug designing, Molecular docking study is helpful in obtaining the information about different types of interactions prevailing between ligand and the receptor protein and therefore facilitating the process of drug discovery easier and economical²¹. Here, in this chapter a detailed theoretical study of some selected 2, 4, 5-triarylimidazole (Fig. 3.C.1) has been carried out using Density Functional Theory.

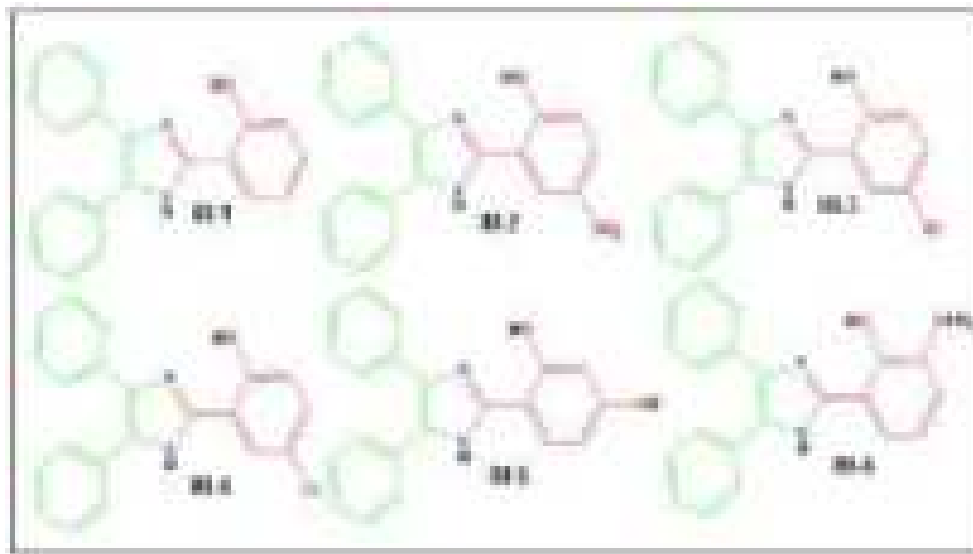


Fig. 3.C.1. Molecular structure of 2, 4, 5-triarylimidazole derivatives (IM-1 to IM-6)

The optimized molecular geometry, vibrational analysis (FT-IR and Raman), molecular orbital (HOMO, LUMO), nonlinear optical property, Global chemical descriptors and Molecular Electrostatic Potential (MEP) of the 2, 4, 5-triarylimidazole derivatives (IM-1 to IM-6) have been reported in this section. Also, an attempt has been made to recognize the inhibitory potential of these derivatives against the Diabetes mellitus protein (PDB ID: 1IR3) by employing molecular docking study and pharmacokinetic properties (ADME) have also been studied.

3.C.2 Results and discussion

3.C.2.1 Computational Study

The molecular geometry, molecular orbital (HOMO, LUMO), Nonlinear Optical property (NLO), Global chemical descriptors and Molecular Electrostatic Potential (MEP) of the selected 2, 4, 5-triarylimidazole derivatives namely, 2-(4,5-diphenyl-1H-imidazol-2-yl)phenol (IM-1), 2-(4,5-diphenyl-1H-imidazol-2-yl)-4-nitrophenol (IM-2), 4-bromo-2-(4,5-diphenyl-1H-imidazol-2-yl)phenol (IM-3), 4-chloro-2-(4,5-diphenyl-1H-imidazol-2-yl)phenol (IM-4), 4-(4,5-diphenyl-1H-imidazol-2-yl)benzene-1,3-diol (IM-5) and 2-methoxy-6-(4,5-diphenyl-1H-imidazol-2-yl)phenol (IM-6) has been optimized by Density Functional Theory (DFT) using Becke's three-parameter hybrid method (B3) with the Lee, Yang and Parr correlation functional methods (LYP) with B3LYP/6-31G+ (d, 2p) level of basis set^{22,23}. All the computational calculations were calculated by Gaussian 16, Revision A.03 programme package²⁴ and the results were visualized using GAUSSVIEW 6.0 software²⁵ on a hp-Z640 desktop P.C. with an Intel Xeon processor (Specifications: E5-2630 V4 @ 220GHz).

3.C.2.1.1 Optimization of Molecular geometry

To the best of our knowledge, the x-ray single crystal structure of the studied compounds (IM-1 to IM-6) have not been reported so far and therefore structure optimization using DFT method serves as a good alternative to ascertain the different geometrical parameters. Thus, the geometrical parameters of the studied compounds (IM-1 to IM-6) were calculated by DFT assay using B3LYP/6-31G+ (d, 2p) level of basis set. The optimized gas phase molecular geometry of the compounds (IM-1 to IM-6) with atom labelling scheme is shown in Fig. 3.C.2 and the structural parameters (bond lengths, bond angle and dihedral angle) are listed in Table 3.C.1. From the Table 3.C.1, the dihedral angles C23-C18-C17-N4, C19-C18-C17-N2 is close to 180° and C19-C18-C17-N4 and C23-C18-C17-N2 is close to 0° except IM-5 for the phenyl ring (2) and this suggest that the phenyl ring (2) is almost planar with the imidazole ring (Fig. 3. C.3.). However, it is evident from the table 3.C.1 that the dihedral angle of other phenyl rings (4 and 5) are far less than the dihedral angle for planar molecule and thus from this, we can infer that the phenyl ring 4 and 5 are not planar with the imidazole ring. Also, for the compound IM-5 all the phenyl rings are not planar to imidazole ring. From Table 3.C.1, it is clearly seen that the C-N bond lengths of imidazole ring in all the studied compounds (IM-1 to IM6) are in the range C1-N2=1.374 Å-1.389 Å, C3-N4=1.380 Å-1.390 Å, N4-C17=1.358 Å to 1.369Å and N2-C17=1.325 Å to 1.330 Å respectively. The shortening of the C-N bond lengths reveals the effect of resonance in this part of the molecule and this can be attributed to the difference in hybridization state of different carbon atoms in the imidazole ring²⁶.

Table. 3.C.1. Structural parameters (bond lengths, bond angle and dihedral angle) of the studied compounds (IM-1 to IM-6)

C-C bond length (Å)					
IM-1		IM-2		IM-3	
C6-C5	1.406	C6-C5	1.407	C6-C5	1.408
C7-C6	1.395	C7-C6	1.396	C7-C6	1.396
C8-C7	1.397	C8-C7	1.397	C8-C7	1.396
C9-C8	1.397	C9-C8	1.398	C9-C8	1.398
C10-C9	1.395	C10-C9	1.394	C10-C9	1.394
C10-C5	1.407	C10-C5	1.407	C10-C5	1.406
C12-C11	1.407	C12-C11	1.405	C12-C11	1.405
C13-C12	1.394	C13-C12	1.395	C13-C12	1.395
C14-C13	1.398	C14-C13	1.397	C14-C13	1.397
C15-C14	1.396	C15-C14	1.398	C15-C14	1.398
C16-C15	1.396	C16-C15	1.395	C16-C15	1.395
C16-C11	1.406	C16-C11	1.406	C16-C11	1.408
C19-C18	1.421	C19-C18	1.412	C19-C18	1.410
C20-C19	1.403	C20-C19	1.310	C20-C19	1.395
C21-C20	1.390	C21-C20	1.388	C21-C20	1.393
C22-C21	1.402	C22-C21	1.396	C22-C21	1.395
C23-C22	1.390	C23-C22	1.389	C23-C22	1.387
C23-C18	1.404	C23-C18	1.404	C23-C18	1.408
IM-4		IM-5		IM-6	
C6-C5	1.408	C6-C5	1.408	C6-C5	1.408
C7-C6	1.396	C7-C6	1.396	C7-C6	1.396
C8-C7	1.397	C8-C7	1.396	C8-C7	1.397
C9-C8	1.398	C9-C8	1.398	C9-C8	1.398
C10-C9	1.394	C10-C9	1.394	C10-C9	1.394
C10-C5	1.407	C10-C5	1.408	C10-C5	1.408
C12-C11	1.405	C12-C11	1.405	C12-C11	1.406
C13-C12	1.395	C13-C12	1.395	C13-C12	1.395
C14-C13	1.397	C14-C13	1.397	C14-C13	1.397
C15-C14	1.398	C15-C14	1.398	C15-C14	1.398
C16-C15	1.395	C16-C15	1.395	C16-C15	1.395
C16-C11	1.406	C16-C11	1.406	C16-C11	1.406
C19-C18	1.410	C19-C18	1.410	C19-C18	1.401
C20-C19	1.395	C20-C19	1.395	C20-C19	1.407
C21-C20	1.393	C21-C20	1.395	C21-C20	1.390
C22-C21	1.395	C22-C21	1.401	C22-C21	1.403
C23-C22	1.388	C23-C22	1.387	C23-C22	1.386
C23-C18	1.407	C23-C18	1.408	C23-C18	1.412
C-H, C-O, N-H, C-Cl, C-Br and O-H bond distances (Å)					
IM-1 (Å)		IM-2 (Å)		IM-3 (Å)	
C6-H26	1.084	C6-H31	1.085	C6-H31	1.085
C7-H27	1.085	C7-H35	1.085	C7-H35	1.085
C8-H28	1.085	C8-H34	1.084	C8-H34	1.084
C9-H29	1.085	C9-H33	1.085	C9-H33	1.085
C10-H30	1.084	C10-H32	1.083	C10-H32	1.083
C12-H31	1.083	C12-H29	1.084	C12-H39	1.084

C13-H32	1.085	C13-H28	1.085	C13-H28	1.085
C14-H33	1.084	C14-H27	1.085	C14-H27	1.085
C15-H34	1.085	C15-H26	1.085	C15-H26	1.085
C16-H35	1.086	C16-H25	1.083	C16-H25	1.083
C20-H36	1.084	C20-H38	1.086	C20-H38	1.082
C21-H37	1.085	C21-H36	1.081	C21-H36	1.082
C22-H38	1.084				
C23-H39	1.086	C23-H39	1.081	C23-H39	1.082
C24-H37		C24-H37	0.965	C24-H37	0.965
C19-O24	1.347	C19-O24	1.372	C19-O24	1.380
N2-H25	1.007	N4-H30	1.009	N4-H30	1.009
O24-H40	0.994	O24-H37	0.966	O24-H37	0.965

C22-
Br40 1.906

IM-4 (Å)		IM-5 (Å)		IM-6 (Å)	
C6-H31	1.085	C6-H31	1.085	C6-H33	1.086
C7-H35	1.085	C7-H35	1.085	C7-H37	1.085
C8-H34	1.084	C8-H34	1.084	C8-H36	1.085
C9-H33	1.085	C9-H33	1.085	C9-H35	1.085
C10-H32	1.083	C10-H32	1.083	C10-H34	1.084
C12-H29	1.084	C12-H29	1.084	C12-H31	1.084
C13-H28	1.085	C13-H28	1.085	C13-H30	1.086
C14-H37	1.085	C14-H27	1.085	C14-H29	1.085
C15-H26	1.085	C15-H26	1.085	C15-H28	1.086
C16-H25	1.084	C16-H25	1.083	C16-H27	1.084
C20-H38	1.086	C20-H38	1.085	C21-H40	1.083
C21-H36	1.082	C22-H40	1.083	C22-H39	1.084
C23-H39	1.082	C23-H39	1.083	C23-H38	1.083
C24-H37	0.965	C19-O24	1.375	C19-O24	1.375
C19-O24	1.380	C21-O36	1.367	C20-O25	1.377
N4-H30	1.009	N4-H30	1.010	N4-H32	1.010
O24-H37	0.965	O24-H37	0.967	O24-H44	0.970
C140-C22	1.759	O36-H41	0.965	O36-H41	0.965

Bond Angle (°)

IM-1		IM-2		IM-3	
C3-C1-N2	104.87	C1-C3-N2	109.73	C3-C1-N2	109.78
N4-C3-C1	109.19	N4-C3-C1	104.63	N4-C3-C1	104.58
C5-C3-C1	130.35	C5-C3-C1	134.54	C5-C3-C1	134.56
C6-C5-C3	119.66	C6-C5-C3	120.55	C6-C5-C3	120.54
C7-C6-C5	120.70	C7-C6-C5	120.80	C7-C6-C5	120.84
C8-C7-C6	120.29	C8-C7-C6	120.19	C8-C7-C6	120.21
C9-C8-C7	119.47	C9-C8-C7	119.50	C9-C8-C7	119.46
C10-C9-C8	120.32	C10-C9-C8	120.43	C10-C9-C8	120.45
C11-C1-N2	120.70	C11-C1-N2	120.14	C11-C1-N2	120.06
C12-C11-C1	121.00	C12-C11-C1	122.04	C12-C11-C1	122.09

C13-C12-C11	120.60	C13-C12-C11	120.68	C13-C12-C11	120.71
C14-C13-C12	120.44	C14-C13-C12	120.32	C14-C13-C12	120.33
C15-C14-C13	119.51	C15-C14-C13	119.45	C15-C14-C13	119.42
C16-C15-C14	120.18	C16-C15-C14	120.31	C16-C15-C14	120.32
C17-N4-C3	107.58	C17-N2-C1	106.79	C17-N2-C1	106.76
C18-C17-N4	124.52	C18-C17-N2	124.14	C18-C17-N2	124.47
C19-C18-C17	119.19	C19-C18-C17	124.05	C19-C18-C18	123.84
C20-C19-C18	119.51	C20-C19-C18	121.23	C20-C19-C18	120.71
C21-C20-C19	120.64	C21-C20-C19	120.63	C21-C20-C19	120.70
C22-C21-C20	120.43	C22-C21-C20	118.17	C22-C21-C20	118.78
C23-C22-C21	119.26	C23-C22-C21	121.97	C23-C22-C21	121.07
O24-C19-C18	122.50	O24-C19-C18	118.03	O24-C19-C18	118.34
H25-N2-C1	124.46	H25-C16-C15	120.39	H25-C16-C15	120.42
H26-C6-C5	119.15	H26-C15-C14	120.07	H26-C15-C14	120.04
H27-C7-C6	119.61	H27-C14-C13	120.24	H27-C14-C13	120.26
H28-C8-C7	120.27	H28-C13-C12	119.58	H28-C13-C12	119.57
H29-C9-C8	120.08	H29-C12-C11	119.81	H29-C12-C11	119.76
H30-C10-C9	119.59	H30-N4-C3	126.48	H30-N4-C3	126.78
H31-C12-C11	119.43	H31-C6-C5	119.67	H31-C6-C5	119.66
H32-C13-C12	119.51	H32-C10-C9	119.94	H32-C10-C9	119.92
H33-C14-C13	120.24	H33-C9-C8	120.04	H33-C9-C8	120.03
H34-C15-C14	120.15	H34-C8-C7	120.24	H34-C8-C7	120.26
H35-C16-C15	119.44	H35-C7-C6	119.65	H35-C7-C6	119.64
H36-C20-C19	117.92	H36-C21-C20	121.62	H36-C21-C20	120.32
H37-C21-C20	119.54	H37-C24-C19	110.05	H37-C24-C19	109.66

H38-C22-C21	120.57	H38-C20-C19	119.42	H38-C20-C19	119.58
H39-C23-C22	118.68	H39-C23-C22	120.56	H39-C23-C22	121.32
H40-O24-C19	108.35	N40-C22-C21	118.86	Br40-C22-C21	119.33
		O41-N40-C22	117.57		
		O42-N40-C22	118.01		
IM-4		IM-5		IM-6	
C3-C1-N2	109.78	C3-C1-N2	109.99	C3-C1-N2	109.85
N4-C3-C1	104.58	N4-C3-C1	104.57	N4-C3-C1	104.54
C5-C3-C1	134.55	C5-C3-C1	134.86	C5-C3-C1	134.58
C6-C5-C3	120.55	C6-C5-C3	120.67	C6-C5-C3	120.55
C7-C6-C5	120.84	C7-C6-C5	120.87	C7-C6-C5	120.87
C8-C7-C6	120.21	C8-C7-C6	120.20	C8-C7-C6	120.23
C9-C8-C7	119.47	C9-C8-C7	119.45	C9-C8-C7	119.43
C10-C9-C8	120.44	C10-C9-C8	120.47	C10-C9-C8	120.46
C11-C1-N2	120.10	C11-C1-N2	119.81	C11-C1-N2	120.01
C12-C11-C1	122.07	C12-C11-C1	122.12	C12-C11-C1	122.13
C13-C12-C11	120.71	C13-C12-C11	120.75	C13-C12-C11	120.75
C14-C13-C12	120.33	C14-C13-C12	120.33	C14-C13-C12	120.34
C15-C14-C13	119.42	C15-C14-C13	119.42	C15-C14-C13	119.39
C16-C15-C14	120.31	C16-C15-C14	120.32	C16-C15-C14	120.33
C17-N2-C1	106.76	C17-N2-C1	106.91	C17-N2-C1	106.69
C18-C17-N2	124.49	C18-C17-N2	125.92	C18-C17-N2	124.85
C19-C18-C17	123.91	C19-C18-C17	122.83	C19-C18-C17	122.93
C20-C19-C18	120.77	C20-C19-C18	121.03	C20-C19-C18	120.78
C21-C20-C19	120.76	C21-C20-C19	119.80	C21-C20-C19	120.60
C22-C21-C20	118.69	C22-C21-C20	120.35	C22-C21-C20	118.83
C23-C22-C21	121.07	C23-C22-C21	119.14	C23-C22-C21	120.76
O24-C19-C18	118.29	O24-C19-C18	122.70	O24-C19-C18	120.66

H25-C16-C15	120.42	H25-C16-C15	120.41	O25-C20-C19	113.36
H26-C15-C14	120.05	H26-C15-C14	120.04	C26-O25-C20	118.41
H27-C14-C13	120.26	H27-C14-C13	120.25	H27-C16-C15	120.45
H28-C13-C12	119.57	H28-C13-C12	119.58	H28-C15-C14	120.03
H29-C12-C11	119.76	H29-C12-C11	119.78	H29-C14-C13	120.27
H30-N4-C3	126.78	H30-N4-C3	123.78	H30-C13-C12	119.57
H31-C6-C5	119.64	H31-C6-C5	119.72	H31-C12-C11	119.72
H32-C10-C9	119.92	H32-C10-C9	119.92	H32-N4-C3	126.98
H33-C9-C8	120.03	H33-C9-C8	120.02	H33-C16-C5	119.63
H34-C8-C7	120.26	H34-C8-C7	120.26	H34-C10-C9	119.90
H35-C7-C6	119.64			H35-C9-C8	120.03
H36-C21-C20	120.61			H36-C8-C7	120.28
H37-C24-C19	109.72			H37-C7-C6	119.62
H38-C20-C19	119.54			H38-C23-C22	121.14
H39-C23-C22	121.02			H39-C22-C21	119.33
C140-C22-C21	119.37			H40-C21-C20	120.91
Selected dihedral angle (°)					
IM-1		IM-2		IM-3	
C23-C18-C17-N4	179.82	C23-C18-C17-N4	-179.26	C23-C18-C17-N4	-179.15
C19-C18-C17-N2	179.40	C19-C18-C17-N2	-179.19	C19-C18-C17-N2	-179.29
C19-C18-C17-N4	-0.13	C19-C18-C17-N4	0.98	C19-C18-C17-N4	0.95
C23-C18-C17-N2	-0.63	C23-C18-C17-N2	0.55	C23-C18-C17-N2	0.60
C10-C5-C3-N4	143.72	C10-C5-C3-N4	-136.48	C10-C5-C3-N4	-137.70
C12-11-C1-N2	136.82	C12-11-C1-N2	-145.75	C12-11-C1-N2	-145.51
C6-C5-C3-N4	-34.50	C6-C5-C3-N4	41.46	C6-C5-C3-N4	40.27
C16-C11-C1-N2	-41.19	C16-C11-C1-N2	32.26	C16-C11-C1-N2	32.45

C6-C5-C3- C1	147.34	C6-C5-C3- C1	-141.20	C6-C5-C3- C1	-142.26
C16-C11- C1-C3	141.25	C16-C11- C1-C3	-149.64	C16-C11- C1-C3	-149.45
C12-C11- C1-C3	-40.72	C12-C11- C1-C3	32.34	C12-C11- C1-C3	32.57
C10-C5-C3- C1	-34.42	C10-C5-C3- C1	40.83	C10-C5- C3-C1	39.75
IM-4		IM-5		IM-6	
C23-C18- C17-N4	-178.77	C23-C18- C17-N4	147.23	C23-C18- C17-N4	179.63
C19-C18- C17-N2	-178.14	C19-C18- C17-N2	147.76	C19-C18- C17-N2	179.99
C19-C18- C17-N4	1.46	C19-C18- C17-N4	-33.45	C19-C18- C17-N4	0.02
C23-C18- C17-N2	1.02	C23-C18- C17-N2	-31.54	C23-C18- C17-N2	-0.39
C10-C5-C3- N4	-137.16	C10-C5-C3- N4	60.73	C10-C5- C3-N4	143.49
C12-11-C1- N2	-145.31	C12-11-C1- N2	-145.86	C12-11- C1-N2	-136.97
C6-C5-C3- N4	40.80	C6-C5-C3- N4	39.14	C6-C5-C3- N4	-34.72
C16-C11- C1-N2	32.69	C16-C11- C1-N2	32.14	C16-C11- C1-N2	-41.66
C6-C5-C3- C1	-141.84	C6-C5-C3- C1	-143.52	C6-C5-C3- C1	-142.57
C16-C11- C1-C3	-149.25	C16-C11- C1-C3	-150.71	C16-C11- C1-C3	-149.20
C12-C11- C1-C3	32.73	C12-C11- C1-C3	31.26	C12-C11- C1-C3	32.83
C10-C5-C3- C1	40.18	C10-C5-C3- C1	38.85	C10-C5- C3-C1	39.46

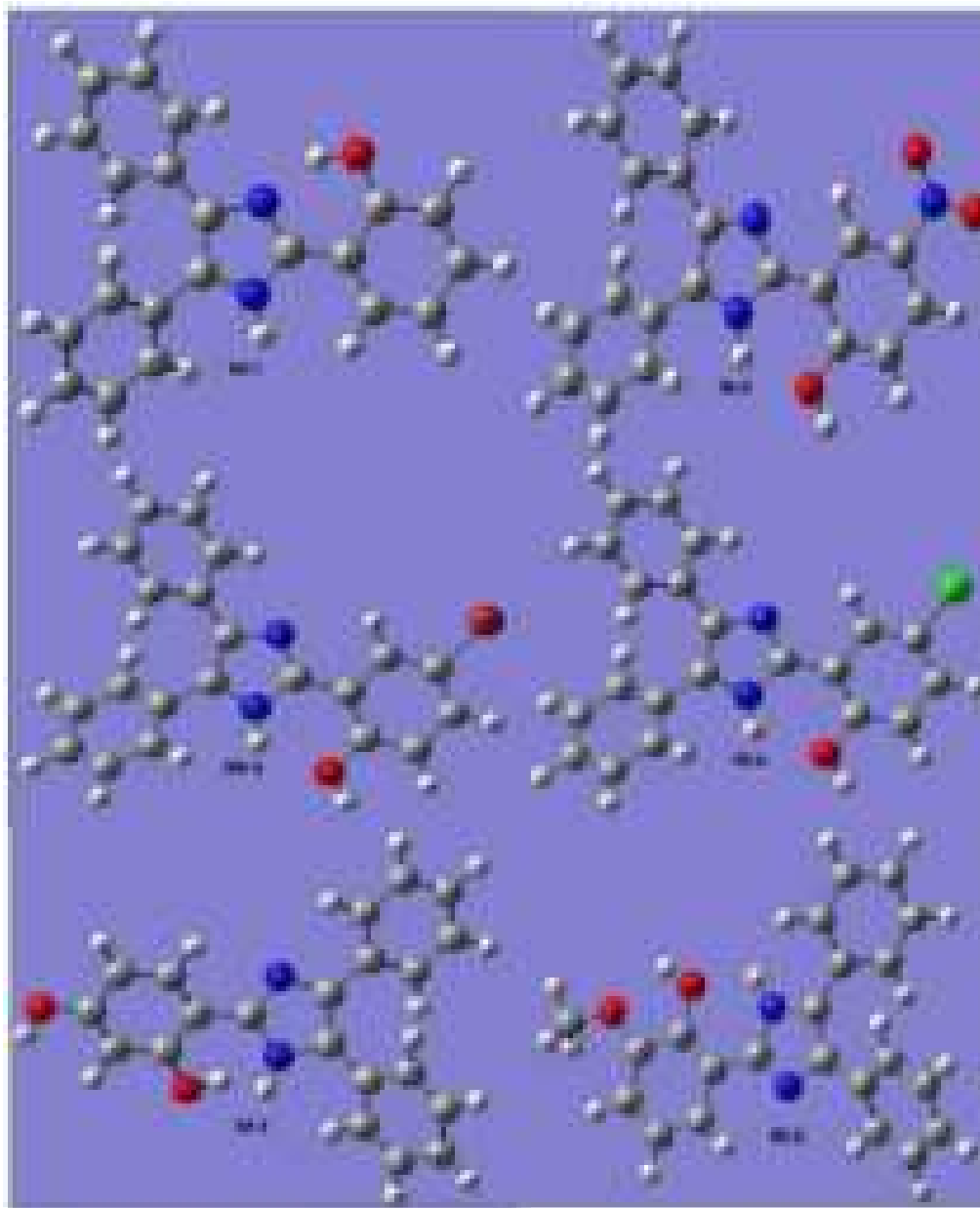


Fig. 3.C.2. Optimized gas phase molecular geometry of the compounds (IM-1 to IM-6) with atom labelling scheme

Again, from the optimized geometry, it is evident that the C-C bond distance of all the aryl groups (IM-1 to IM-6) are in the range 1.390 Å to 1.421 Å which suggests that the carbon atoms are highly conjugated and electrons are delocalized through resonance²⁷.

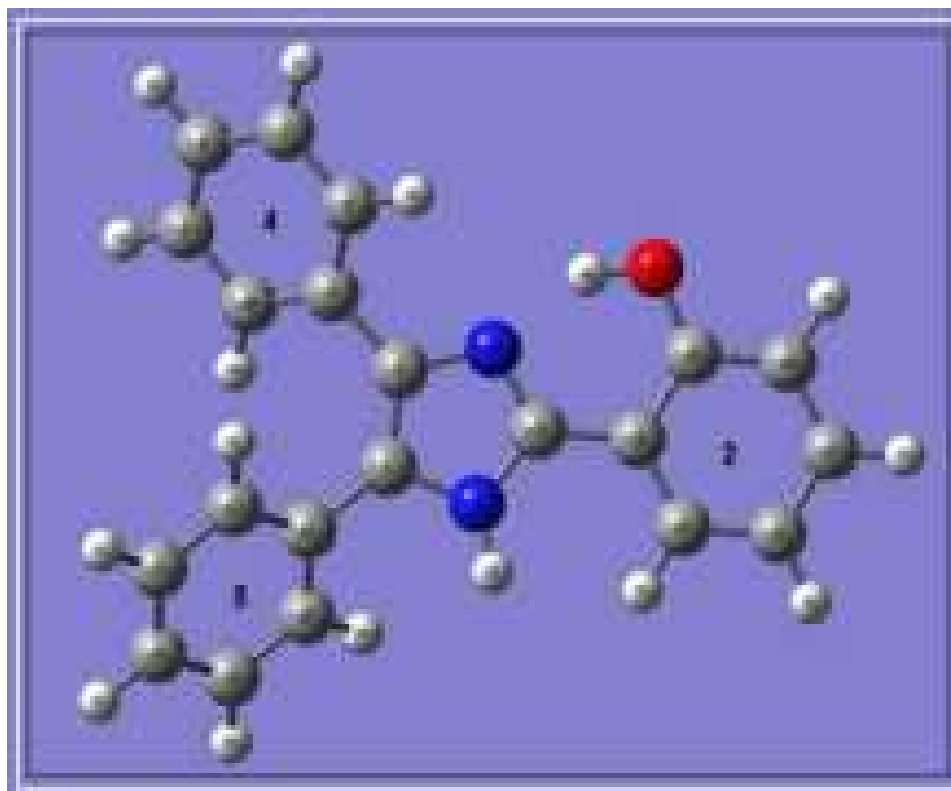


Fig. 3.C.3. Labelling of different phenyl ring attached to imidazole ring

The aromatic C-H, aliphatic C-H, C-O, O-H and N-H and C-halogen bond distances for the studied compounds are in the range 1.081 Å-1.095 Å, 1.089 Å-1.095 Å, 1.348 Å-1.380 Å, 0.960 Å-0.990 Å, 1.008 Å-1.011 Å and 1.795 Å-1.907 Å respectively.

3.C.2.1.2 Frontier Molecular Orbitals

The Highest Occupied Molecular Orbital (HOMO) and the Lowest Unoccupied Molecular Orbital (LUMO) constitutes the frontier molecular orbitals and the HOMO and LUMO are very important quantum mechanical parameter which determines the molecular reactivity. The frontier molecular orbital helps in predicting the excitation properties as well as electron transport quantitatively^{28,29}. Since HOMO is the higher energy orbital containing the outermost electron and therefore it acts as an electron donor whereas, LUMO is the lowest energy orbital that has vacant space to accept the electrons and thus it acts as an electron acceptor³⁰. The energies of HOMO and LUMO orbitals of the studied compounds (IM-1 to IM-6) are calculated using DFT/B3LYP method using 6-31G+ (d, 2p) level of basis set and shown in Fig. 3. C.4. The energy of HOMO and LUMO orbitals of the studied compounds (IM-1 to IM-6) are listed in Table 3.C.2

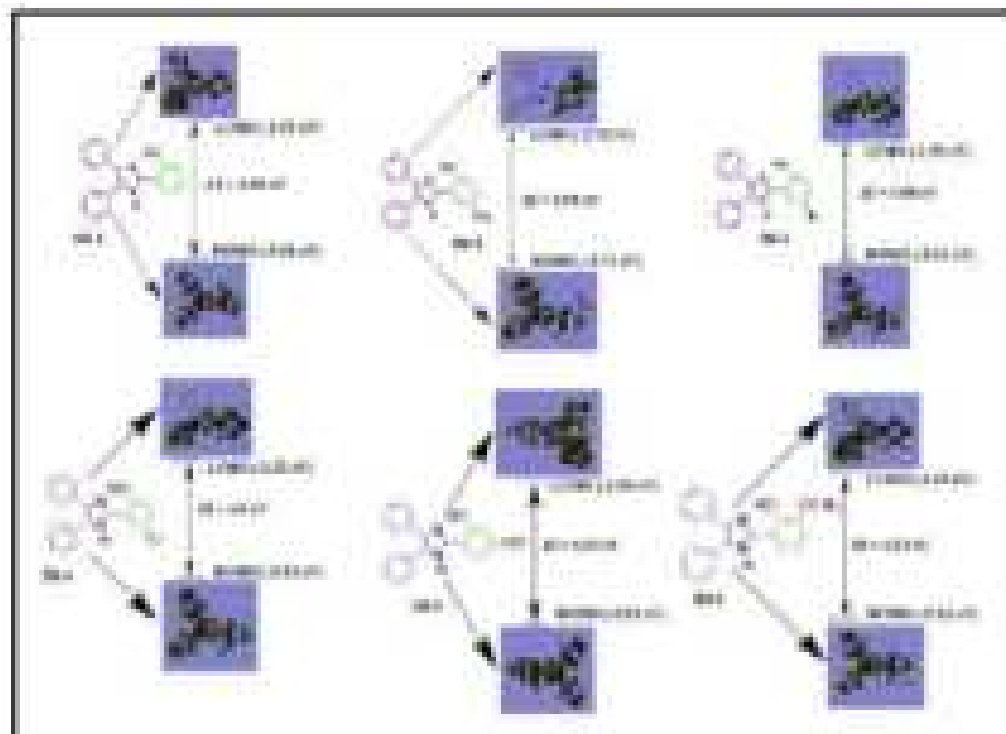


Fig. 3.C.4. Energies of HOMO and LUMO orbitals of the studied compounds (IM-1 to IM-6)

From the Table3.C.2 it is evident that the energy of HOMO and LUMO orbitals for all the compounds are negative and this infers that the compounds (IM-1 to IM-6) under investigation are relatively stable³¹ and the energy of HOMO and LUMO orbitals of the compounds -5.60 eV (IM-1), -5.71 eV (IM-2), -5.51 eV (IM-3), -5.52 eV (IM-4), -5.52 eV (IM-5) and -5.31 eV (IM-6) and -1.52 eV (IM-1), -2.72 eV (IM-2), -1.53 eV (IM-3), -1.52 eV (IM-4), -1.39 eV (IM-5), and -1.2 eV (IM-6), respectively. Interestingly, by employing HOMO-LUMO energy, it is possible to calculate the global chemical descriptors like chemical potential, global hardness and global electrophilicity which in turn are very much helpful in understanding the structure of molecule and their reactivity. Thus, these new chemical descriptors could help in understanding the various aspects of pharmacological properties of the molecule for the process of drug design³². The ionization energy (I) and electron affinity (A) can be express in terms of HOMO and LUMO orbital energies as follows;

$$I = -E_{\text{HOMO}} \text{ and } A = -E_{\text{LUMO}}$$

The chemical reactivity descriptors such as chemical potential (μ), Electronegativity (χ), Global hardness (η) and global electrophilicity power (ω) can be calculated with the help of following relation;

$$\text{Chemical potential } (\mu) = (E_{\text{HOMO}} + E_{\text{LUMO}})/2 = -(I+A)/2$$

$$\text{Electronegativity } (\chi) = (I+A)/2$$

$$\text{Global Hardness } (\eta) = (-E_{\text{HOMO}} + E_{\text{LUMO}})/2 = (I-A)/2$$

$$\text{electrophilicity power } (\omega) = \mu^2/2 \eta$$

Where I and A are the first ionization potential and electron affinity of the chemical species³³⁻³⁵. The ionization energy (I), electron affinity (A), Chemical potential (μ), Electronegativity (χ), Global hardness (η) and Global electrophilicity power (ω) of the studied compounds (IM-1 to IM-6) are listed in Table 3.C.

Table. 3.C.2. Energies of HOMO and LUMO orbitals, ionization energy (I), electron affinity (A), Chemical potential (μ), Electronegativity (χ), Global hardness (η) and Global electrophilicity power (ω) of the studied compounds (IM-1 to IM-6)

Parameters (eV)	IM-1	IM-2	IM-3	IM-4	IM-5	IM-6
E_{HOMO}	-5.60	-5.71	-5.51	-5.52	-5.52	-5.31
E_{LUMO}	-1.52	-2.72	-1.53	-1.52	-1.39	-1.2
ΔE	4.08	2.99	3.98	4.0	4.13	4.11
Ionization Energy (I)	5.60	5.71	5.51	5.52	5.52	5.31
Electron Affinity (A)	1.52	2.72	1.53	1.52	1.39	1.2
Chemical potential (μ)	-3.56	-4.21	-3.52	-3.52	-3.40	-3.25
Electronegativity (χ)	3.56	4.21	3.52	3.52	3.40	3.25
Global hardness (η)	2.04	1.49	1.99	2.0	2.06	2.05
Electrophilicity power (ω)	3.10	5.96	3.11	3.09	2.80	2.57

It is seen that the chemical potential of all the studied molecules are negative and it suggest that they do not decompose spontaneously into its elements they are made up of.

Apparently, it is seen that the hard molecule has large HOMO-LUMO gap and soft molecule has small HOMO-LUMO gap³⁶. Thus, from the Table 3.C.2 it is evident that the hardness of the studied molecule follows the order IM-5 > IM-6 > IM-1 > IM-4 > IM-3 > IM-2. Moreover, the hardness signifies the resistance towards the deformation of electron cloud of chemical systems under small perturbation that occur during the chemical reaction. Thus, hard system is less polarisable than soft system²³⁷. Again, a large value of electrophilicity is assigned for good electrophile whereas nucleophile is described by low value of nucleophilicity³⁸.

3.C.2.1.3 FT-IR analysis

Study of the molecular vibrations of organic compounds has become an important area of interest for both the experimental and theoretical chemist. DFT method provides an avenue for the theoretical calculation of molecular vibrations of the studied system and therefore, it is possible to correlate the experimental and theoretical FT-IR spectra of the studied compounds to ascertain the different type of structural features in the molecules. Thus, we calculated the theoretical vibrational spectra of 2, 4, 5-triarylimidazole derivative (IM-1 to IM-6) using DFT at the B3LYP/6-31G+ (d, 2p) level of theory on optimized geometry of the molecules in the gas phase. The experimental and theoretical vibrational frequencies of the compounds (IM-1 to IM-6) are given in Table 3.C.3 with the proper assignment of the observed peaks.

Table. 3.C.3. Experimental and theoretical vibrational frequencies of compounds (IM-1 to IM-6) (with B3LYP/6-31G+(d,2p)) with proposed assignments.

IM-1				
Unscaled frequency (cm ⁻¹) (theoretical)	IR _i	R _A	IR Frequency (cm ⁻¹) (Experimental)	Assignments
3658	48.42	41.924		νNH stretch
3232	788.36	41.92	3474	νOH, Ar-H stretch
3210.38	12.79	412.3	3242	ν(s)Ar-H stretch
3210.13	10.63	173.5		ν(s)Ar-H stretch
3207	5.99	252.96		ν(s)Ar-H stretch
3203	15.59	10.53		ν(as)Ar-H stretch
3202.69	18.27	127.8		ν(as)Ar-H stretch
3202.38	25.25	191.27		ν(as)Ar-H stretch
3195	28.92	119.46		ν(as)Ar-H stretch
3190	14.55	115.89		ν(as)Ar-H stretch
3184	11.35	84.24		ν(as)Ar-H stretch
3183	5.81	145.3		ν(as)Ar-H stretch
3181	0.03	82.33		ν(as)Ar-H stretch
3174	1.35	37.83		ν(as)Ar-H stretch
3171	6.61	27.66		ν(as)Ar-H stretch
3165	7.91	23.38	3060	ν(as)Ar-H stretch
1667	40.73	1053.19		νAr C-C stretch
1651	11.3085	485.91		νAr C-C stretch
1649	24.92	911.16		νAr C-C stretch
1620	3.78	20.55	1622	νAr C-C stretch
1600	22.71	297.28	1604	νC-N stretch
1566	95	599.49	1540	νC-N stretch
IM-2				
3641.38	96.29	58.99	3472	νNH Stretch
3818.57	103.21	149.09		νOH Stretch
3245.02	10.7009	15.8316		νAr-H Stretch
3242.89	9.6	77.38		νAr-H Stretch

Chapter-III C

3210.27	5.55	194.82		vAr-H, Stretching
3209.76	6.88	181.62		vAr-H, Stretching
3204.4	11.18	74.42		vAr-H, Stretching
3201.73	24.08	209.41		v(s)Ar-H stretch
3195.78	29.7	141.34		v(as)Ar-H stretch
3183.01	9.03	139.87		v(as)Ar-H stretch
3173.62	0.89	38.95		v(as)Ar-H stretch
3190.47	15.81	116.5		v(as)Ar-H stretch
3181.28	0.1676	85.0583		v(as)Ar-H stretch
3172.01	5.86	27.03	3114	v(as)Ar-H stretch
3172.56	11.23	173.41	3074	v(as)Ar-H stretch
1601.4	208.7869	690.64	1633	vAr C-C stretch
1589.21	87.99	491.21	1582	v(C-N)
1557.33	15.84	2333.06	1542	v(C-N)
1497.57	17.92	1378.67	1521	vAr C-C stretch
1489	14.61	11.26	1486	v(as)Ar C-C stretch
IM-3				
3827.08	86.96	136.75	3442	vOH stretch
3634.83	788.36	41.92	3291	vNH stretch
3231.07	4.2	21.86	3135	vAr-H stretch
3219.75	0.4123	123.25	3226	vAr-H stretch
3209.7	6.76	309.08	3076	vAr-H stretch
3209.56	5.4	54.34	3056	v(as)Ar-H stretch
3204.22	11.0532	64.22		v(as)Ar-H
1651.52	12.58	681.24	1644	vAr C-C stretch
1649.41	21.27	1360.38	1604	vAr C-C stretch
1646.76	41.32	1580.4		vAr C-C stretch
1630.5	20.72	5.08	1632	vAr C-C stretch
1622.25	0.0707	111.5005		vAr C-C stretch
1620.15	4.37	33.26		vAr C-C stretch
1590.39	11.6654	396.9559	1578	C-N stretch
1556.97	17.1555	2615.621	1567	C-N stretch
IM-4				
3827.32	85.7726	133.9766		vOH stretch
3634.43	106.0925	57.1155	3418	vNH stretch
3229.9	3.9093	26.2057	3251	vAr-H stretch
3220.4	0.2948	147.3086	3242	vAr-H stretch
3209.54	7.252	318.69		vAr-H stretch
3209.41	5.1044	50.3604	3209	v(as)Ar-H stretch
3203.97	11.3212	66.8154		v(as)Ar-H stretch
3201.19	25.63	219.486	3201	v(as)Ar-H stretch
3194.92	31.52	149.25	3114	v(as)Ar-H stretch
3189.81	17.09	110.6403		v(as)Ar-H stretch
3181.62	9.84	142.99		v(as)Ar-H stretch
3180.59	0.414	90.1		v(as)Ar-H stretch
3172.33	1.116	41.03		v(as)Ar-H stretch
3171.93	5.66	26.12		v(as)Ar-H stretch
3166.56	13.56	154.75	3061	v(as)Ar-H stretch
1651.54	11.81	718.24	1651	vAr C-C stretch
1649.53	17.79	1524.32		vAr C-C stretch

1647.47	48.77	1257.07	1644	vAr C-C stretch
1631.68	18.44	68.34	1634	vAr C-C stretch
1622.58	0.137	112.94	1622	vAr C-C stretch
1620.09	4.105	34.3	1614	vAr C-C stretch
1590.66	13.006	386.67	1595	v(C-N) stretch
1557.07	19.22	2502.51	1556	v(C-N) stretch

IM-5

3773.49	111.57	108.6881		vOH stretch
3619.13	47.1489	49.9262	3425	vNH stretch
3220.43	4.1185	152.5289		vAr-H stretch
3210.31	5.9372	204.4215		vAr-H stretch
3209.86	6.2675	170.2552		vAr-H, v(as)Ar-H
3206.14	1.3545	66.4073		v(as)Ar-H stretch
3204.36	10.288	69.6803		v(as)Ar-H stretch
3202	23.7868	211.9301		v(as)Ar-H stretch
3195.43	30.8886	150.7853		v(as)Ar-H stretch
3190.52	16.7916	106.2932		v(as)Ar-H stretch
3185.34	9.1487	153.3553		v(as)Ar-H stretch
3182.19	9.6808	143.7116		v(as)Ar-H stretch
3181.11	0.2736	85.9813		v(as)Ar-H stretch
3172.94	1.1981	41.401		v(as)Ar-H stretch
3172.28	6.8368	27.2422	3072	v(as)Ar-H stretch
1671.12	253.3	970.9654	1719	vAr C-C stretch
1651.49	17.3527	554.8251		vAr C-C stretch
1648.56	35.9852	860.9897		vAr C-C stretch
1632.65	55.6989	24.6022		vAr(as) C-C stretch
1624.93	7.7909	70.4983		vAr(as) C-C stretch
1619.8	4.8628	40.5719	1619	vAr(as) C-C stretch
1598.7	12.1418	348.9312	1606	v(C-N) stretch
1571.67	4.4461	2693.2735	1504	v(C-N) stretch

IM-6

3748.11	166.697	79.0223		vOH stretch
3625.93	116.3687	55.5652	3472	vNH stretch
3224.9	5.8139	105.2289		vAr-H stretch
3218.13	4.0713	123.0545		v(as)Ar-H stretch
3209.12	7.4102	309.2013		vAr-H stretch
3208.97	5.0436	54.2279		vAr-H stretch
3203.78	11.3706	61.8553		vAr-H stretch
3200.59	26.48	222.2055		v(as)Ar-H stretch
3194.17	34.5723	164.4011		v(as)Ar-H stretch
3193.13	8.8803	100.0075		v(as)Ar-H stretch
3189.17	18.3066	101.4483		v(as)Ar-H stretch
3180.41	10.6102	151.1789		v(as)Ar-H stretch
3179.8	1.1344	94.3466		v(as)Ar-H stretch
3171.75	5.3497	26.4064		v(as)Ar-H stretch
3171.08	1.3653	41.0078		v(as)Ar-H stretch
3151.36	17.9877	129.9481	3113	v(as)C-H stretch
3089.03	29.3834	70.125	3095	v(as)C-H stretch

3022.44	65.2015	202.1064	3057	v(as)C-H stretch
1665.15	44.6263	1988.7348		v Ar C-C stretch
1651	22.0456	535.5365		vAr C-C stretch
1648	34.9659	781.8783		vAr C-C stretch
1634	1.1624	16.2312	1632	vAr C-C stretch
1623	9.1141	56.3615		vAr C-C stretch
1619	2.9154	30.9688	1616	vAr C-C stretch
1592	47.7744	316.3398	1604	v(C-N) stretch
1561	34.8924	2702.0752	1539	v(C-N) stretch

3. C.2.1.3.1 C-H stretching vibration.

For the studied compounds (IM-1 to IM-6), C-H functional group is present at a number of positions. The characteristics region of C-H stretching vibration of aromatic ring falls in the range 3100-3000 cm^{-1} ³⁹. In the present investigation, theoretically calculated bands in the range 3210-3165 cm^{-1} , 3245-3172 cm^{-1} , 3231-3204 cm^{-1} , 3229-3166 cm^{-1} , 3220-3172 cm^{-1} and 3224-3151 cm^{-1} were assigned to aromatic C-H stretching vibrations for compounds IM-1, IM-2, IM-3, IM-4, IM-5 and IM-6 respectively. Pure symmetric bands were calculated at 3210 and 3207 cm^{-1} in IM-1, 3245, 3242, 3210, 3209, 3204 and 3201 cm^{-1} in IM-2, 3231, 3219 and 3209 cm^{-1} in IM-3, 3229, 3220 and 3209 cm^{-1} in IM-4, 3220, 3210 and 3209 cm^{-1} in IM-5 and 3224, 3209, 3208 and 3203 cm^{-1} in IM-6 respectively. Experimentally, symmetric bands were observed at 3242 cm^{-1} in IM-1, 3135 and 3126 cm^{-1} in IM-3 and 3251 and 3242 cm^{-1} in IM-4 respectively. Asymmetric vibrational bands were calculated with stretching frequencies 3203, 3202, 3195, 3190, 3184, 3183, 3181, 3174, 3171 and 3165 cm^{-1} in IM-1, 3195, 3183, 3181, 3173, and 3172 cm^{-1} in IM-2, 3209 and 3204 cm^{-1} in IM-3, 3209, 3203, 3201, 3194, 3189, 3180, 3172 and 3166 cm^{-1} in IM-4, 3206, 3204, 3202, 3195, 3190, 3185, 3182, 3181 and 3172 cm^{-1} in IM-5 and 3194, 3193, 3189, 3180, 3179, 3151, 3089 and 3022 cm^{-1} in IM-6 respectively. Experimentally, Asymmetric vibrational bands were observed at 3060 cm^{-1} in IM-1, 3114 and 3074 cm^{-1} in IM-2, 3056 cm^{-1} in IM-3, 3201, 3114 and 3061 cm^{-1} in IM-4, 3072 cm^{-1} in IM-5 and 3113, 3095 and 3057 cm^{-1} in IM-6 respectively (Table 3.C.3).

3. C.2.1.3.2 Aromatic C-C stretching vibrations

Generally, the bands observed in the range 1650-1400 cm^{-1} are assigned to C-C stretching mode of aromatic derivatives⁴⁰. In our present study, the range for theoretically calculated C-C stretching vibrational mode showing sharp bands are in the range 1667-1620 cm^{-1} , 1497-1489 cm^{-1} , 1651-1620 cm^{-1} , 1651-1620 cm^{-1} , 1671-1619 cm^{-1} and 1665-1619 cm^{-1} for IM-1, IM-2, IM-3, IM-4, IM-5 and IM-6 respectively (Table 3.C.3). Experimentally, the aromatic C-C stretching frequencies for the studied compounds observed in the range 1622-1540 cm^{-1} in IM-1, 1521-1486 cm^{-1} in IM-2, 1644-1632 cm^{-1} in IM-3, 1651-1614 cm^{-1} in IM-4, 1619 cm^{-1} in IM-5 and 1632-1616 cm^{-1} in IM-6 respectively.

3. C.2.1.3.3 C-N bond stretching vibrations

C-N stretching vibration is an important stretching vibration for the compounds containing N-atom in the ring structure. Since we are focusing our study on the 2, 4, 5-trisubstituted imidazole derivatives and therefore, C-N stretching vibration of such molecule is fundamentally important to ascertain their structure. Because of the integration of several bands, it is very difficult to detect the C-N stretching vibration in a molecule. Theoretically we observed the C-N stretching frequency of the studied compound at 1600 and 1566 cm^{-1} in IM-1, 1589 and 1557 cm^{-1} in IM-2, 1590 and 1556 cm^{-1} in IM-3, 1590 and 1557 cm^{-1} in IM-4, 1598 and 1571 cm^{-1} in IM-5 and 1592 and 1561 cm^{-1} in IM-6 respectively. 1604 and 1540 cm^{-1} in IM-1, 1582 and 1542 cm^{-1} in IM-2, 1578 and 1562 cm^{-1} in IM-3, 1595 and 1556 cm^{-1} in IM-4, 1606 and 1504 cm^{-1} in IM-5 and 1604 and 1539 cm^{-1} in IM-6 respectively.

Thus, from the above discussion it is evident that the theoretically calculated vibrational frequency matched well with the experimental results for the studied compounds (Fig. 3.C.5).

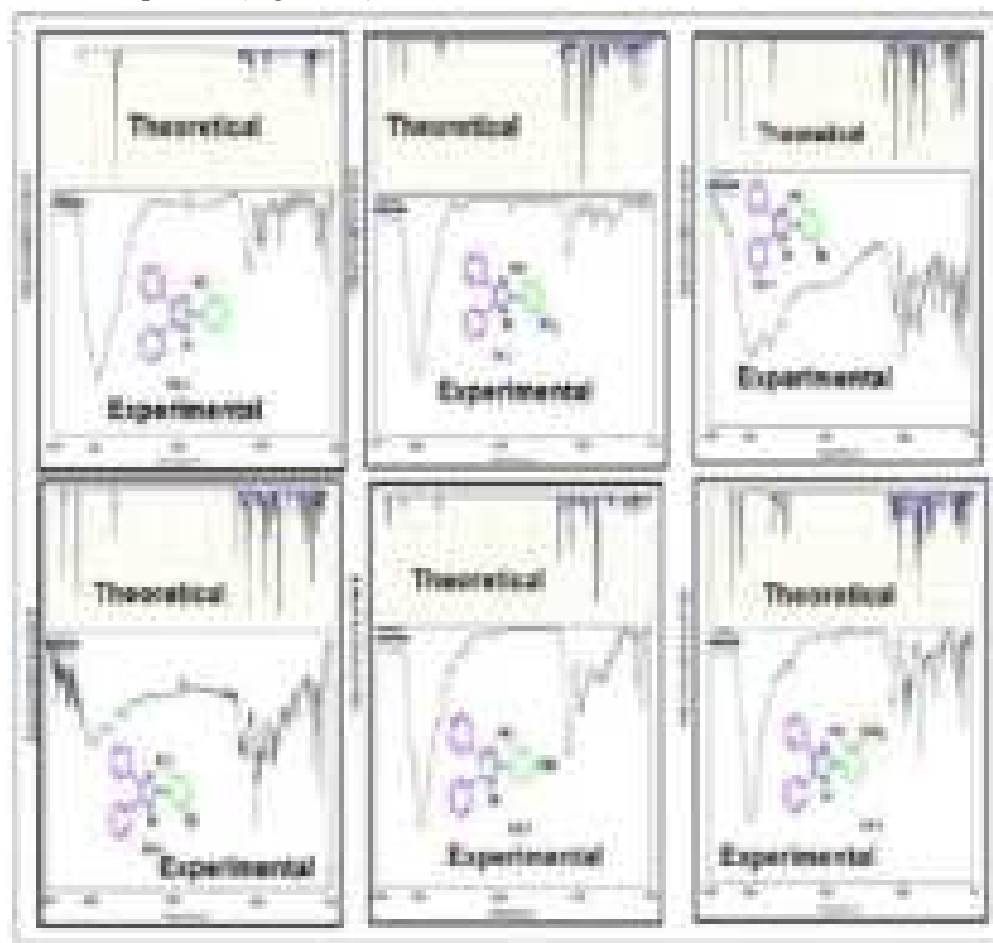


Fig. 3.C.5. Theoretical and experimental FT-IR spectra of IM-1 to IM-6

3.C.2.1.4 Molecular Electrostatic Potential (MEP)

A chemical system always creates an electrostatic potential around itself and Molecular electrostatic potential is an important parameter to ascertain and correlate between the molecular structure and the physicochemical properties of molecules⁴¹. MEP is also useful in understanding the sites for electrophilic and nucleophilic reactions along with the hydrogen bonding interactions⁴². To predict the reactive sites of electrophilic and nucleophilic attack for the investigated molecules (IM-1 to IM-6), MEP at B3LYP/6-31G+ (d, 2p) optimized geometry was calculated. The significance of MEP provides a visual method to understand the relative polarity of the given molecule and the different values of the electrostatic potential at the MEP surface are given by different colours such as red, blue and green. Red, blue and green colour represents the region of most negative, most positive and zero electrostatic potential respectively. Thus, the electrostatic potential increases in the order blue > green > yellow > orange > red. The most negative electrostatic potential (red, orange and yellow region) in the MEP surface is assigned for the electrophilic reaction sites and the positive (blue region) corresponds to nucleophilic reaction site^{43,44}. The MEP surface of the studied compounds (IM-1 to IM-6) is depicted in Fig. 3.C.6.

A detailed description of the MEP surface indicating the region of negative/electrophilic reaction sites and positive/nucleophilic reaction site for the studied compounds (IM-1 to IM-6) are listed in Table 3.C.4.

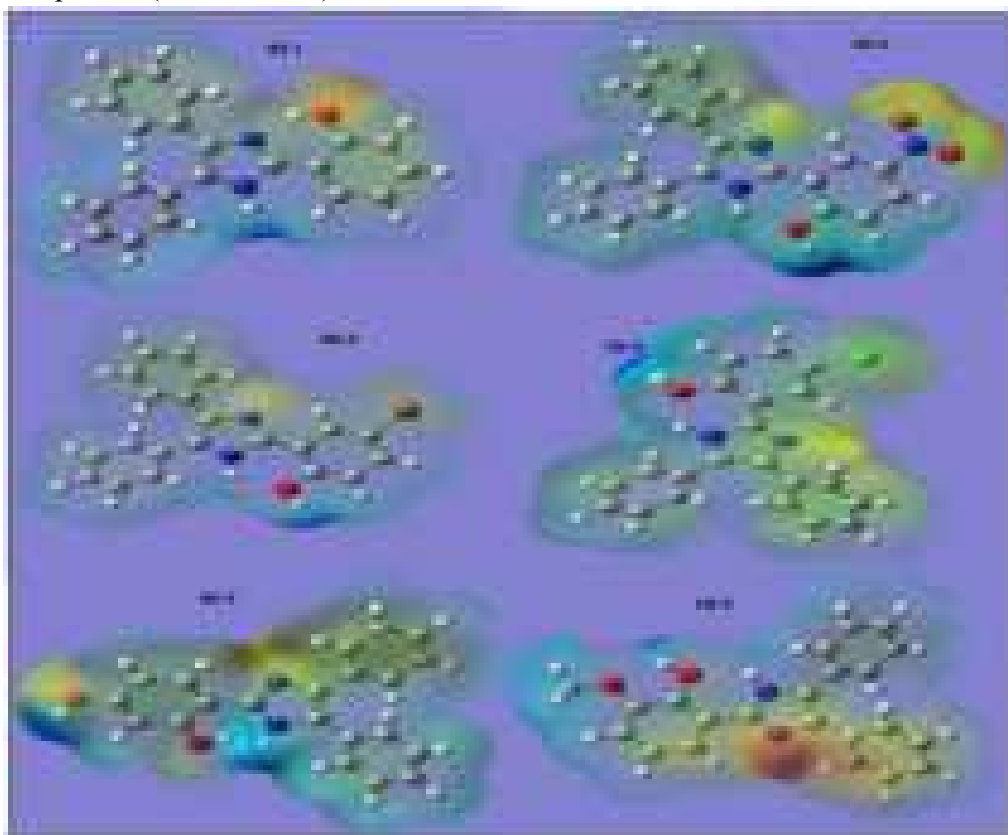
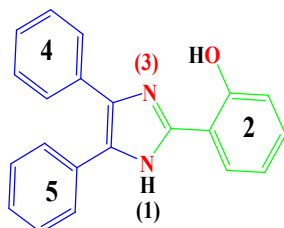


Fig. 3.C.6. MEP plot of studied compounds (IM-1 to IM-6)

Table 3.C.4. Detailed description of MEP surface for compounds IM-1 to IM-6

Entry	Negative region (red, orange, yellow)/Electrophilic reaction site	Positive region (blue)/Nucleophilic reaction site
IM-1	-OH group of 2-phenyl ring and N(3) of imidazole core	NH(1) of imidazole ring and 5-phenyl ring
IM-2	NO ₂ group of 2-phenyl ring and N(3) of imidazole core	-OH group of 2-phenyl ring and NH(1) region of imidazole core
IM-3	N(3) of imidazole ring and Br group of 2-phenyl ring	-OH group of 2-phenyl ring and NH (1) region of imidazole core
IM-4	N(3) of imidazole ring and Cl group of 2-phenyl ring	-OH group region of 2-phenyl ring and NH (1) region of imidazole core
IM-5	N(3) of imidazole ring and both the -OH group of 2-phenyl ring	NH (1) region of imidazole core and 5-phenyl ring
IM-6	N(3) of imidazole ring and 4-phenyl ring.	-OH and -OCH ₃ group of 2-phenyl ring, NH (1) region of imidazole core and 5-phenyl ring.



3.C.2.1.5 NLO properties

Nonlinear optical phenomenon is generally associated with the generation of new electromagnetic fields, altered in wave number, phase or other physical properties by the interaction of various materials with the applied electromagnetic field⁴⁵. Interestingly, organic molecules consisting of delocalized electron density with π - conjugation is known to exhibit relatively strong NLO properties⁴⁶. Thus, the NLO properties of the organic molecules are due to the delocalization of electrons and the intra-molecular charge transfer from donor orbital to acceptor orbital through π -spacer⁴⁷. Organic molecule based NLO materials are gaining lot of interest during last few decades because of their facile synthesis and structural modification. Structural modifications of such organic NLO materials could easily be achieved either by suitably positioning the donor-acceptor groups or simply by lengthening the chain of the π -spacer⁴⁸. Thus, organic nonlinear optical materials are at the centre of attention because of its application in optical communications, optical computing, dynamic image processing, optical modulation and signal processing⁴⁹. The second order nonlinear optical properties in the molecule arise due to the absence of centre of symmetry in the molecule and this phenomenon is largely exploited in the field of telecommunications and optical switches⁵⁰. Theoretically, the NLO properties of the given compound is calculated by determining the parameters such as magnitude of dipole moment (μ), polarizability (α), anisotropy of polarizability ($\Delta\alpha$), first hyperpolarizability (β) and second order hyperpolarizability (γ). The polarizability tensors are calculated using the following relations:⁵¹

$$\text{Dipole moment } \mu = (\mu_x^2 + \mu_y^2 + \mu_z^2)^{1/2} \dots\dots\dots (1)$$

$$\alpha(\text{total}) \text{ or } \langle \alpha \rangle = \frac{1}{3} (\alpha_{xx} + \alpha_{yy} + \alpha_{zz}) \dots\dots\dots (2)$$

$$\Delta\alpha = 1/\sqrt{2} [(\alpha_{xx} - \alpha_{yy})^2 + (\alpha_{yy} - \alpha_{zz})^2 + (\alpha_{zz} - \alpha_{xx})^2 + 6(\alpha_{xy}^2 + \alpha_{xz}^2 + \alpha_{yz}^2)]^{1/2} \dots\dots\dots (3)$$

$$\beta_x = \beta_{xxx} + \beta_{xyy} + \beta_{xzz} \dots\dots\dots (4)$$

$$\beta_y = \beta_{yyy} + \beta_{yzz} + \beta_{yxx} \dots\dots\dots (5)$$

$$\beta_z = \beta_{zzz} + \beta_{zxx} + \beta_{yyz} \dots\dots\dots (6)$$

$$\beta_{\text{total}} = (\beta_x^2 + \beta_y^2 + \beta_z^2)^{1/2} \dots\dots\dots (7)$$

$$\langle \gamma \rangle \text{ or } \gamma_{\text{total}} = 1/5 (\gamma_{xxxx} + \gamma_{yyyy} + \gamma_{zzzz} + 2(\gamma_{xxyy} + \gamma_{yyzz} + \gamma_{xxzz})) \dots\dots\dots (8)$$

Table. 3.C.5. Dipole moments, dipole polarizabilities, anisotropic polarizabilities and First order hyperpolarizabilities of the studied compounds (IM-1 to IM-6)

Dipole moments, dipole polarizabilities and anisotropic polarizabilities							
Entry	IM-1	IM-2	IM-3	IM-4	IM-5	IM-6	Ref.
μ_x	-2.23	-3.40	-0.96	-0.40	0.47	-0.03	0
μ_y	-3.82	-7.76	-5.33	-5.46	-3.22	3.83	-4.06
μ_z	0.22	-0.27	-0.24	-0.26	0.06	-0.22	0.0018
μ	4.43	8.48	5.42	5.48	3.25	3.84	4.06
α_{xx}	-130.17	-168.1	-148.8	-141.5	-130.7	-122.2	-16.62
α_{yy}	-129.16	-138.0	-134.4	-133.3	-138.1	-147.6	-24.64
α_{zz}	-144.20	-157.7	-162.3	-156.1	-147.8	-155.6	-27.03
α_{xy}	-5.86	-25.3	-9.28	-14.22	4.66	2.55	-0.0003
α_{xz}	0.14	-0.63	-0.80	-0.62	3.74	0.89	-0.07
α_{yz}	4.37	-4.16	-4.00	-4.06	5.21	4.40	0.01
$\alpha_{tot} \times 10^{-24}(\text{esu})$	-19.93	-22.91	-22.01	-21.29	-20.58	-21.01	-3.37
$\Delta\alpha \times 10^{-24}(\text{esu})$	2.86	7.66	4.42	4.82	2.99	4.67	1.39
First order hyperpolarizabilities							
β_{xxx}	9.65	-206.5	104.05	-12.63	-68.75	178.34	-0.0026
β_{xyy}	-29.5	5.42	81.60	26.13	19.42	-36.02	-0.0004
β_{xzz}	-10.0	22.01	56.70	4.90	-9.85	5.37	0.001
β_{yyy}	-15.4	-79.68	43.75	-58.45	-9.91	39.65	-16.94
β_{xxy}	-27.9	-152.5	-49.38	-88.01	-66.01	17.55	-0.63
β_{yzz}	1.60	-0.55	6.41	-4.14	-5.56	4.36	2.05
β_{zzz}	0.32	-0.72	-0.38	-0.60	-5.49	-0.57	-0.01
β_{xxz}	3.53	-4.61	-2.71	-4.87	-26.53	-4.12	-0.09
β_{yyz}	-1.46	1.04	1.31	0.37	8.19	-0.76	-0.03
β_{xyz}	1.65	3.03	5.15	2.68	-9.19	-0.34	0.05
$\beta_{total} \times 10^{-30}(\text{esu})$	0.44	2.53	2.22	1.31	0.89	1.38	0.13

Encouragingly, 2, 4, 5-triarylimidazole derivatives also consists of extended π -conjugated system carrying three phenyl rings in conjugation with imidazole core and therefore, it was thought worthwhile to study the NLO properties of this type molecules. The nonlinear optical properties such as dipole moments, dipole polarizabilities, first- and second order hyperpolarizabilities of the studied compounds (IM-1 to IM-6) were calculated by B3LYP/ 6-31G + (d, 2p) basis set and the computed results are listed in Table 3.C.5

A comparative study of the dipole moment in the studied system indicates that they have different charge distributions for different directions. The theoretically calculated dipole moments of the studied compounds are 4.433 D (IM-1), 8.485 D (IM-2), 5.426 D (IM-3), 5.485 D (IM-4), 3.257 D (IM-5) and

3.845 D (IM-6) respectively and the dipole moment increases in the order IM-2 > IM-4 > IM-3 > IM-1 > IM-6 > IM-5.

The compounds IM-2, IM-3 and IM-4 have dipole moment value greater than that of urea (4.06 D) whereas the compounds IM-1, IM-5 and IM-6 have dipole moment value less than that of urea reference. Also, the total dipole polarizabilities value of the studied compounds along all three directions is listed in Table 3.C.5. From the Table 3.C.5 it is evident that the dipole polarizability of the studied compounds follows the order IM-2 (-2.291×10^{-25} esu) > IM-3 (-2.201×10^{-25}) > IM-4 (-2.129×10^{-25}) > IM-6 (-2.101×10^{-25}) > IM-5 (-2.058×10^{-25}) > IM-1 (-1.993×10^{-25}).

The theoretically computed first-order hyperpolarizabilities and their individual components for the studied compounds (IM-1 to IM-6) are listed in Table 3.C.5. From the table, it is evident that the first-order hyperpolarizability of the studied compounds are 0.44×10^{-30} esu, 2.53×10^{-30} esu, 2.22×10^{-30} esu, 1.31×10^{-30} esu, 0.89×10^{-30} esu and 1.38×10^{-30} esu for compounds IM-1, IM-2, IM-3, IM-4, IM-5 and IM-6 respectively. A comparison of the first-order hyperpolarizability value of the studied compounds with the standard reference urea (0.13×10^{-30} esu) have shown that the studied compounds have far greater value of first-order hyperpolarizability value than urea. Thus, the order for the first-order hyperpolarizability of the studied compounds are IM-2 > IM-3 > IM-6 > IM-4 > IM-5 > IM-1 and the large value of first-order hyperpolarizability of compounds IM-2 and IM-3 may be attributed to the presence of on strongly activating -OH group and one weakly deactivating -NO₂ and -Br group on the same ring of IM-2 and IM-3 respectively. The smallest first-order hyperpolarizability of compound IM-1 is due to the presence of only one activating group (-OH) which in turn do not favour the long-range charge transfer.

The second order hyperpolarizabilities of the compounds IM-1 to IM-6 are given in Table. 3.C.6. The second order hyperpolarizability of the studied compounds are -2.09×10^{-36} esu, 2.90×10^{-36} esu, 2.81×10^{-36} esu, 2.58×10^{-36} esu, 2.35×10^{-36} esu and 2.54×10^{-36} esu for IM-1, IM-2, IM-3, IM-4, IM-5 and IM-6 respectively and the order of second-hyperpolarizability of the studied compounds is given by IM-2 > IM-3 > IM-4 > IM-6 > IM-5 > IM-1. From the table it is evident that the second-hyperpolarizability of the studied compounds are much greater than the reference NLO material urea (Table 3.C.6).

Table. 3.C.6. Second order hyperpolarizabilities of studied compounds IM-1 to IM-6

Second order hyperpolarizabilities							
Entry	γ_{xxxx}	γ_{yyyy}	γ_{zzzz}	γ_{xxyy}	γ_{yyzz}	γ_{xxzz}	γ_{total} (X 10^{-36}) esu
IM-1	-7820.16	-3932.39	-390.80	-1949.79	-790.72	-1563.42	-2.09
IM-2	-13028.6	-4271.77	-391.77	-2623.38	-892.70	-2053.87	-2.90
IM-3	-11965.2	-4234.85	-402.27	-2554.67	-911.54	-2198.72	-2.81
IM-4	-10704.9	-4204.68	-395.87	-2314.38	-878.58	-1968.24	-2.58
IM-5	-9278.62	-3865.49	-529.51	-2209.55	-806.84	-1832.3	-2.35
IM-6	-9718.89	-4378.68	-408.31	-2470.13	-853.66	-2057.45	-2.54
Urea	-120.668	-117.90	-29.39	-44.0275	-28.019	-39.86	-0.049

From the above discussion, it is evident that the studied molecule IM-1 to IM-6 have shown greater value of nonlinear optical parameters than the reference urea molecule and we may infer that this set of molecules could act as a better nonlinear optical material.

3.C.2.2 Molecular Docking Study

Molecular docking now a day have become an essential technique in structure-based drug design and can be employed in facilitating and speed up the process of development of drugs^{52,53}. Molecular docking provides a useful insight into the different types of interactions prevailing between the ligand and the target protein as well as helps in predicting the binding confirmations and affinities of any ligand to the target protein. Diabetes mellitus which is caused either by insulin deficiency or insulin resistance is a chronic metabolic disorder and have become a global concern now a day⁵⁴. Since, insulin is an essential component in human body which maintain blood glucose and regulates carbohydrate mechanism. Any disruption in blood glucose level in human body leads to hyperglycemia and other metabolic abnormalities of the disease. Basically, there are two types of diabetes, type I usually associated with the autoimmune of beta cells of the pancreas which leads to insulin deficiency and type II which usually involves insulin resistance or decreased insulin secretion⁵⁵. For the regulation of blood sugar level in our body, Tyrosine Kinase beta subunit gets activated by the conformational change of the receptor through the binding of insulin to the alpha subunit of insulin Receptor (IR) and helps in insulin signal pathway and this activation. In diabetes mellitus, Insulin

signaling including activation of IR tyrosine kinase activity is impaired. Several human proteins such as glucokinase, AMP-activated protein kinase, 11 β -hydroxysteroid dehydrogenases (11 β -HSD), insulin receptor substrate, interleukin1 beta, dipeptidyl peptidase IV, glutamine-fructose-6-phosphate amidotransferase (GFAT), peroxisome proliferator-activated receptor-gamma (PPAR-gamma), tyrosine phosphatases, tyrosine kinase insulin receptor, protein kinase B, and insulin receptor have been identified as key regulators in the development of diabetes. Interestingly, among the many types of tyrosine kinase receptor, protein kinase (PDB ID: 1IR3) is a protein receptor that are highly regulated enzyme⁵⁶. Therefore, any compound or drugs which augment insulin receptor tyrosine kinase activity would be useful in the treatment of diabetes mellitus. The 1IR3 protein kinase receptor consists of two lobes, the N-terminal lobe and the C-terminal lobes that are connected to each other by hinge region and features a deep cleft bound by the two lobes. This cleft contains the ATP binding pocket in the protein kinase domain (Fig 3.C.7).

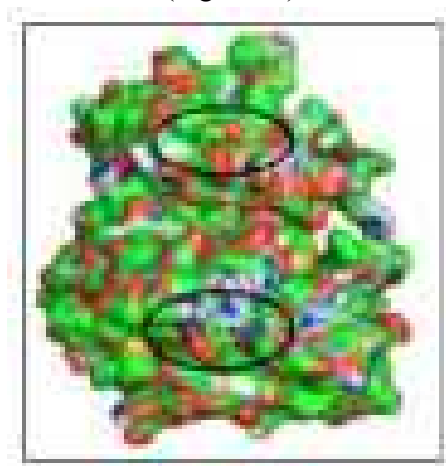


Fig. 3.C.7. The N-terminal and C-terminal lobe in the protein 1IR3.

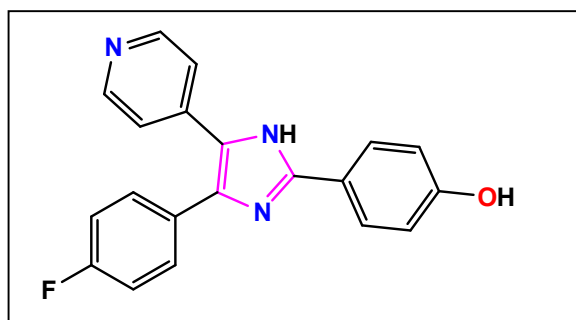


Fig. 3.C.8. Molecular structure of SB202190

A numerous therapeutic agents have been developed and reported to treat and manage diabetes, including dietary modifications, exercise, and anti-diabetic agents. However, many of the reported anti-diabetic agents are usually associated with severe side effects⁵⁷. Moreover, tri-arylimidazole drug SB202190 or 4-(4-Fluorophenyl)-2-(4-hydroxyphenyl)-5-(4-pyridyl)-1H-imidazole (Fig.3.C.8) have been used as an inhibitor of MAP kinase P38² by SmithKline Beechman scientists and they found that this drug could block the cytokine production⁵⁸. Therefore, we were interested to explore the inhibitory efficacy of some of the selected 2, 4, 5-triarylimidazole derivatives against the insulin receptor protein 1IR3. Interestingly, studies on the phosphorylate of tyrosine complex (1IR3) have shown that the Activation (A-) loop of the kinase goes through major conformational change due to the autophosphorylation of amino acid residues Tyr1158, Try1162 and Tyr1163⁵⁹. Thus, in this section we are reporting the molecular docking study of the selected 2, 4, 5-triaryimidazole derivatives against the insulin receptor protein (PDB ID: 1IR3).

3.C.2.2.1 Visualization of the Docking result

Molecular docking study of the compounds (IM-1 to IM-6) against the insulin receptor protein (1IR3) has been carried out using GUI interface programme of Autodock Tools (MGL tool or Molecular Graphics Laboratory tool developed by Scripps research Institute⁶⁰). The docking results have been visualized with the help of Biovia Discovery Studio 2020 (DS), version 21.1.0.20298 and Edu Pymol version 2.5.2.

After successful docking of the compounds (IM-1 to IM-6) with the protein 1IR3, the docking result showed different types of protein-ligand interactions with particular binding energies. For better understanding of fitting of the ligand into the binding pocket of the protein, ligands are shown as blue green stick. The hydrogen bonding interactions between ligands and protein are shown by green dash line, the Pi-sulfur interaction as yellow dash line, π -anion/ π -cation interactions as orange dash line, π -sigma interactions as purple dash line, π - π stacking/ π - π T-shaped interactions as dark pink dash line and π -alkyl interactions as light pink dash line respectively. The binding energy (ΔG) and the predicted inhibitory constant (**pKi**) of the studied compounds (IM-1 to IM-6) are found to be -8.7 Kcal/mole (IM-1), -8.4 Kcal/mole (IM-2), -8.8 Kcal/mole (IM-3), -8.0 Kcal/mole (IM-4), -8.9 Kcal/mole (IM-5) and -7.8 Kcal/mole (IM-6) respectively and 0.307 μ M, 0.515 μ M, 0.258 μ M, 1.027 μ M, 0.217 μ M and 1.451 μ M respectively (Table 3.C.7).

Table. 3.C.7. Summary of docking of the compound (IM-1 to IM-6) against insulin receptor protein IIR3 with corresponding binding energy (ΔG), predicted inhibitory constant (**pKi**), interacting amino acid residues and type of interactions.

Compounds	Binding Energy (kcal/mol)	Predicted inhibitory constant (pKi) μM	Amino Acid residues	Type of interactions
IM-1	-8.7	0.307	His1268, Asp1143 and Phe1144	π - Cation, H-bonding and π - π stacked
IM-2	-8.4	0.515	His1057, His1058, Gln1111, Asp1143, His1268, Phe1144 and Met1112	H-bonding, Carbon H-bond, π -donor H-bond, π - π stacked, π - π T-shaped, π - π stacked and π - Alkyl
IM-3	-8.8	0.258	Glu1115 and His1268	H-bonding, π - π T-shaped and π - Cation
IM-4	-8.0	1.027	Arg1092, Pro1103, Leu1205, Glu1207, Asp1232 and Thr1203	Alkyl, π - Alkyl, π -Sigma, Alkyl, π - Alkyl π - Anion, H-bonding and π - Anion
IM-5	-8.9	0.217	His1268, Glu1115 and Gln1111	π - Cation, Unfavorable Acceptor-Acceptor and H-bonding
IM-6	-7.8	1.451	Thr1145, Glu1115, Asp1143, Glu1108, Met1112, Ser1270, Phe1144, His1268, His1057 and Val1274	H-bonding, π - Anion, π -Sulphur, π - Donor π - π stacked, Alkyl and π - Alkyl

The visualization of the docking result of compound IM-1 against the protein IIR3 revealed that the ligand IM-1 fits in the vicinity of C-lobe inside a pocket region of the receptor protein. A detailed analysis of the docking result of IM-1 with protein IIR3 showed that the ligand IM-1 binds to the protein with binding energy (ΔG) -8.7 Kcal/mole and the predicted inhibitory constant (**pKi**) found to be 0.307 μM . The important interactions prevailing between the ligand IM-1 and the protein IIR3 have been characterized by a conventional hydrogen bonding between carboxyl group (-COOH) of the amino acid residue Asp1143 and the H atom of -OH group of the ligand present at the 2-phenyl ring (Fig 3.C.9) at a distance 2.32 Å. Also, the amino acid residue Phe1144 interacts with the ligand IM-1 through π - π stacked interactions between two phenyl ring of the Phe1144 and the 5-phenyl ring of the ligand at a distance 5.90 Å. Furthermore, the amino acid residue His1268 interacts with the ligand via π -cation interaction involving the π -

electron of the amino acid residue and 4-phenyl ring of the ligand at a distance 4.92 Å.

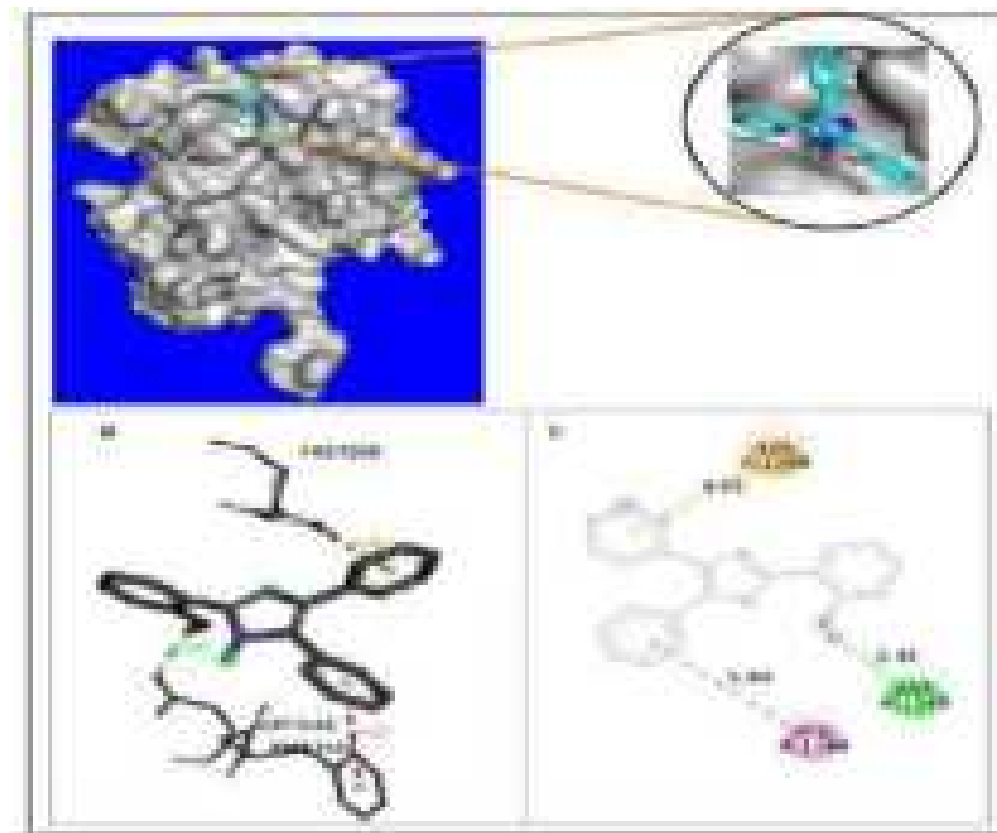


Fig. 3.C.9. Visualisation of docking results of ligand IM-1 within protein kinase 1IR3: (A) Optimal binding mode of the protein kinase with IM-1 ligand (Ligand IM-1 shown as blue and green stick model). (B) Amino acid residues involved in different interactions (green dash lines show H-bonding, pink lines show π - π stacked interaction, and orange dash line shows π -cation interactions). (C) 2D representation of binding interaction of ligand IM-1 with different amino acid residues of the protein 1IR3.

A close visualization of the docking result of ligand IM-2 with the receptor protein 1IR3 revealed that the ligand also fits in the vicinity of C lobe of the protein with binding energy (ΔG) -8.4 Kcal/mole and predicted inhibitory constant (**pKi**) 0.515 μM . The major interactions between the ligand IM-2 and the receptor protein 1IR3 have been characterized by five hydrogen bonding interactions namely, (i) first hydrogen bonding occurs between H atom of NH group of Imidazole ring of amino acid residue His 1057 and O atom of NO_2 group of ligand IM-2 at a distance 2.83Å, (ii) second H-bonding interaction exist between H atom of NH group of imidazole ring of amino acid residue His 1058 and O atom of NO_2 group of ligand IM-2 at a distance 1.89 Å, (iii) Third hydrogen bonding exist between the O atom of C=O group of amino acid residue Asp1143 and H atom of NH group of imidazole core of ligand IM-2 at a distance 1.89 Å and (iv) fourth and

fifth hydrogen bonding interactions occurs between both the H atom of NH₂ group of amino acid residue Gln 1111 and O atom of NO₂ group of ligand IM-2 at a distance 2.84 Å and 2.91 Å respectively (Fig 3.C.10). Apart from conventional hydrogen bonding interactions, other type of interactions between the ligand IM-2 and protein 1IR3 includes, π - π stacking between the π -electrons of the 2-phenyl ring and 4-phenyl ring of ligand IM-2 and π -electron of imidazole ring of the amino acid residue His1268 at a distance 4.83 Å and 5.44 Å respectively.

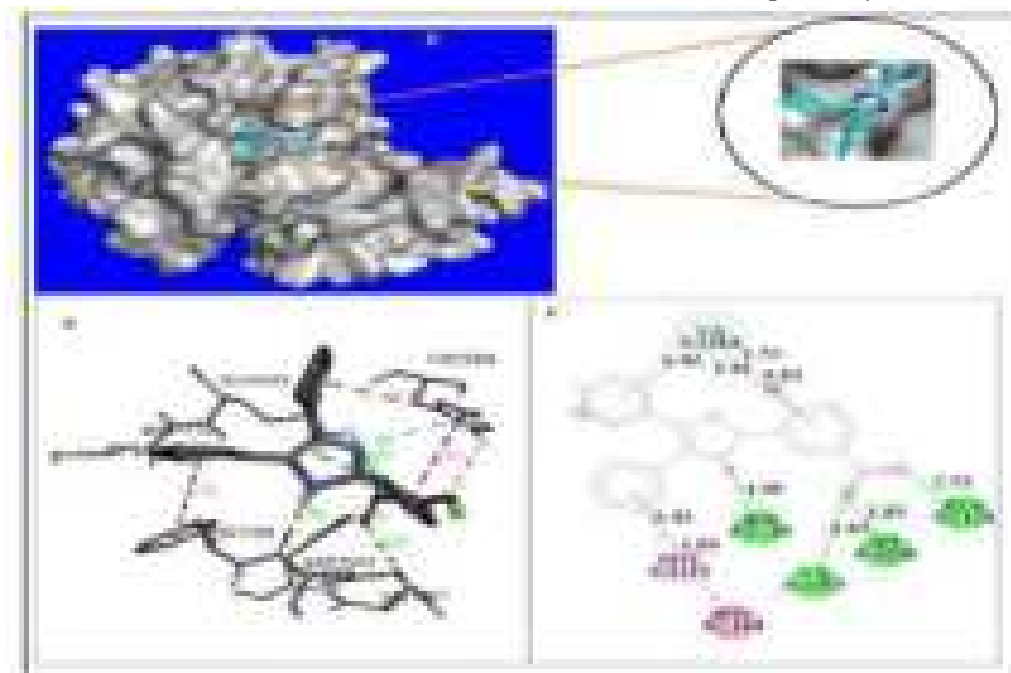


Fig. 3.C.10. Visualisation of docking results of ligand IM-2 with the protein kinase 1IR3: (A) Optimal binding mode of the protein kinase with IM-2 ligand (Ligand IM-2 shown as blue and green stick model). (B) Amino acid residues involved in different interactions (green dash lines show H-bonding, pink lines show π - π stacked, π - π T-shaped interactions and light-pink lines show π -alkyl interactions). (C) 2D representation of binding interaction of ligand IM-2 with different amino acid residues of the protein 1IR3

Another π - π T shaped interaction occur between the π -electron of phenyl ring of amino acid residue Phe1144 and π -electron of 5-phenyl ring of ligand IM-2 at a distance 5.89 Å. Other interactions such as carbon-hydrogen bond (between CH group of imidazole moiety of amino acid residue His1268 and O-atom of OH group of ligand IM-2 at a distance 3.70 Å), π -alkyl interaction (between π -electron of 5-phenyl ring of ligand IM-2 and alkyl group of amino acid residue Met 1122 at a distance 5.43 Å) and π -donor hydrogen bond (between π -electron of imidazole ring of residue His 1268 and N atom of imidazole core of ligand IM-2 at a distance 3.94 Å) respectively have also been observed.

Docking of ligand IM-3 with protein 1IR3 revealed that the ligand IM-3 interacts with the protein through three major type of interactions namely

conventional hydrogen bonding, π - π T-shaped and π -cation interactions respectively with binding energy (ΔG) -8.8 Kcal/mole and predicted inhibitory constant (**pKi**) 0.258 μ M. The conventional hydrogen bonding interaction occurs between the O atom of COOH group of amino acid residue Glu 1115 and H-atom of OH group present at 2-phenyl ring of ligand IM-3 at a distance 1.91 Å (Fig 3.C.11). π - π T shaped interaction occurs between π -electron of imidazole ring of amino acid residue His 1268 and π -electron of imidazole core of the ligand IM-3 at a distance 5.03 Å. Also, π -cation interaction is exhibited between the NH group of imidazole moiety of amino acid residue His 1268 and π -electron of 4-phenyl ring of the ligand IM-3 at a distance 4.77 Å.

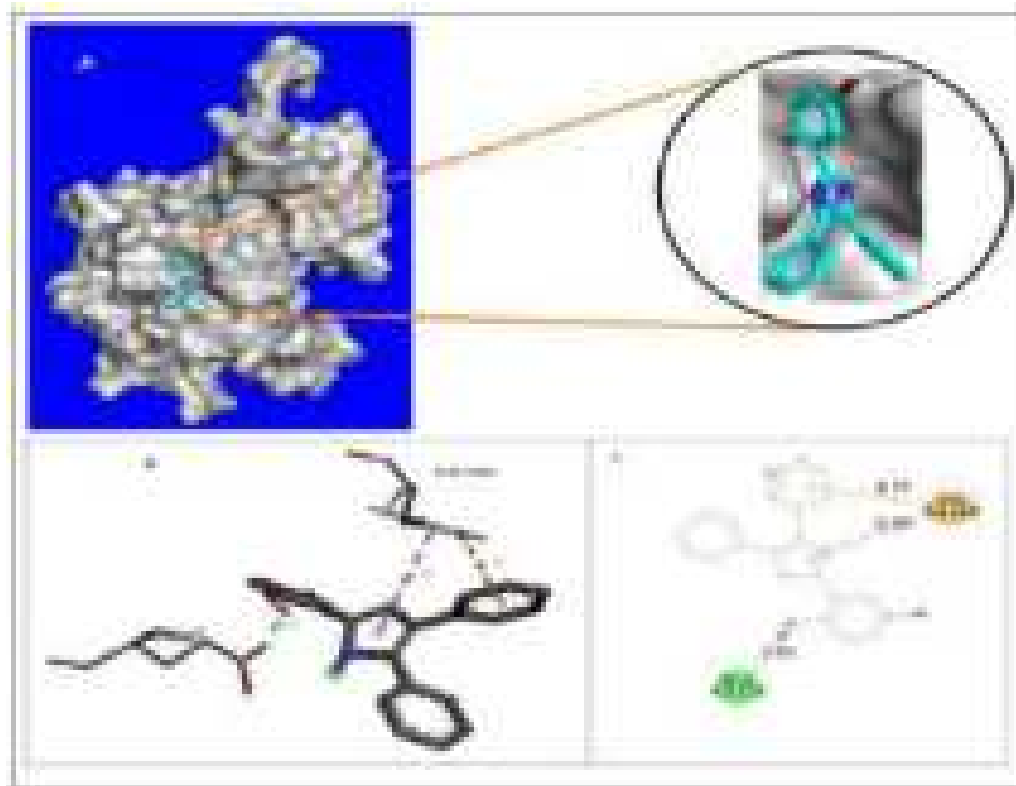


Fig. 3.C.11. Visualisation of docking results of ligand IM-3 with the protein kinase 1IR3: (A) Optimal binding mode of the protein kinase with IM-3 ligand (Ligand IM-3 shown as blue and green stick model). (B) Amino acid residues involved in different interactions (green dash lines show H-bonding, pink lines show π - π T-shaped interactions and orange lines show π -cation interactions). (C) 2D representation of binding interaction of ligand IM-3 with different amino acid residues of the protein 1IR3.

The analysis of docking result of ligand IM-4 with the protein 1IR3 revealed that the ligand binds to the protein inside the pocket region present at the C-lobe with binding energy (ΔG) -8.0 Kcal/mole and predicted inhibitory constant (**pKi**) 1.027 μ M. The ligand IM-5 forms four major hydrogen bonding interactions with the protein 1IR3. Among the four hydrogen bonding interactions, two of the

hydrogen bonds are formed between the O atom of C=O group of amino acid residue Asp 1232 and H-atom of OH group present at 2-phenyl ring and H atom of NH group of imidazole core of ligand IM-4 at a distance 2.76 Å and 2.61 Å respectively. The other two hydrogen bonds are formed between O atom of C=O group of amino acid residue Thr 1203 and H atom of OH group present at 2-phenyl ring and H atom of NH group of imidazole core of ligand IM-4 at a distance 2.51 Å and 2.35 Å respectively (Fig 3.C.12). Other interactions are characterized as π -anion (between π -electron of 5-phenyl ring of ligand IM-4 and COO⁻ group of amino acid residue Glu 1207 and Asp 1232 at a distance 4.56 Å and 3.79 Å respectively), π -sigma interaction (between π electron of 4 phenyl ring of ligand IM-4 and sigma electron of amino acid residue Leu 1205 at a distance 3.56 Å) and π -alkyl interaction (between π -electron of 4-phenyl ring of ligand IM-4 and alkyl group of amino acid residue Arg 1092 at a distance 4.60 Å).

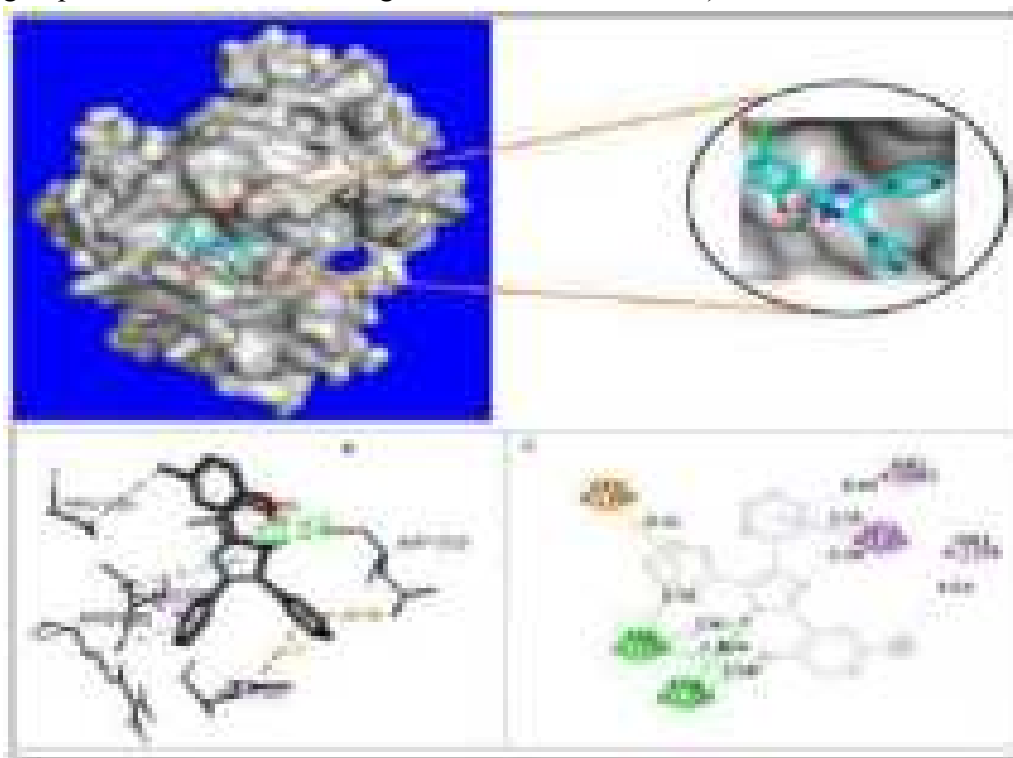


Fig. 3.C.12. Visualisation of docking results of ligand IM-4 with the protein kinase 11R3: (A) Optimal binding mode of the protein kinase with IM-4 ligand (Ligand IM-4 shown as blue and green stick model). (B) Amino acid residues involved in different interactions (green dash lines show H-bonding, pink lines show π -sigma interactions, light-pink lines show alkyl and π -alkyl interactions, and orange lines show π -anion interactions). (C) 2D representation of binding interaction of ligand IM-4 with different amino acid residues of the protein 11R3.

A close inspection of the docking result of ligand IM-5 with the protein 1IR3 revealed that the ligand IM-5 displayed highest binding affinity among all the studied ligands (IM1-IM-6) with binding energy (ΔG) -8.9 Kcal/mole and predicted inhibitory constant (**pKi**) 0.217 μM . The ligand IM-5 also fits in a similar pocket region present at the C-lobe of the protein. A conventional hydrogen bonding was found to exist between the H atom of amide group ($\text{NH}_2\text{-C=O}$) of the amino acid residue Gln 1111 and the O atom of OH group present at 2-phenyl ring of the ligand IM-5 at a distance 2.21 Å. The other interaction is π -cation interaction which exist between NH group of imidazole ring of amino acid residue His 1268 and π -electron of 4-phenyl ring of ligand IM-5 at a distance 4.83 Å. An unfavourable acceptor-acceptor interaction has also been observed between O atom of COO- group of amino acid residue Glu1115 and O atom of OH group present at 2-phenyl ring of ligand IM-5 at a distance 2.72 Å (Fig 3.C.13).

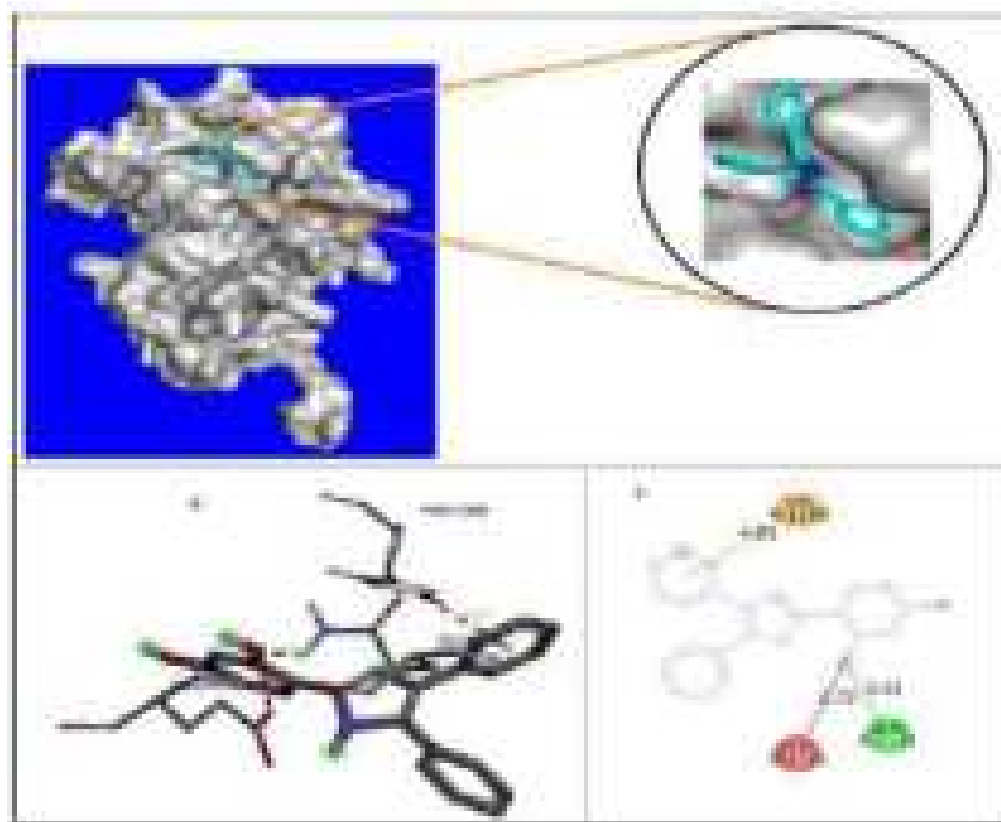


Fig. 3.C.13. Visualisation of docking results of ligand IM-5 with the protein kinase 1IR3: (A) Optimal binding mode of the protein kinase with IM-5 ligand (Ligand TI5 shown as blue and green stick model). (B) Amino acid residues involved in different interactions (green dash lines show H-bonding, red lines show unfavourable acceptor-acceptor interactions, and orange lines show π -cation interactions). (C) 2D representation of binding interaction of ligand IM-5 with different amino acid residues of the protein 1IR3.

The analysis of docking result of ligand IM-6 with the protein 1IR3 showed that the ligand IM-6 binds with the protein at the same binding pocket present at

the C-lobe of the protein with binding affinity (ΔG) -7.8 Kcal/mole and predicted inhibitory constant (**pKi**) 1.45 μM . The interactions between ligand IM-6 and the protein 1IR3 have been characterized by three major hydrogen bonding interactions. The first two hydrogen bonds occurs between the H atom of OH group present at 2-phenyl ring of ligand IM-6 and O atom of COO- group of amino acid residue Glu1115 and O atom of OH group of amino acid residue Thr 1145 at a distance 2.66 Å and 2.36 Å respectively. The other hydrogen bond exists between H atom of NH (imidazole core) of ligand IM-6 and O atom of C=O group of amino acid residue Asp 1143 at a distance 2.36 Å (Fig. 3.C.14).

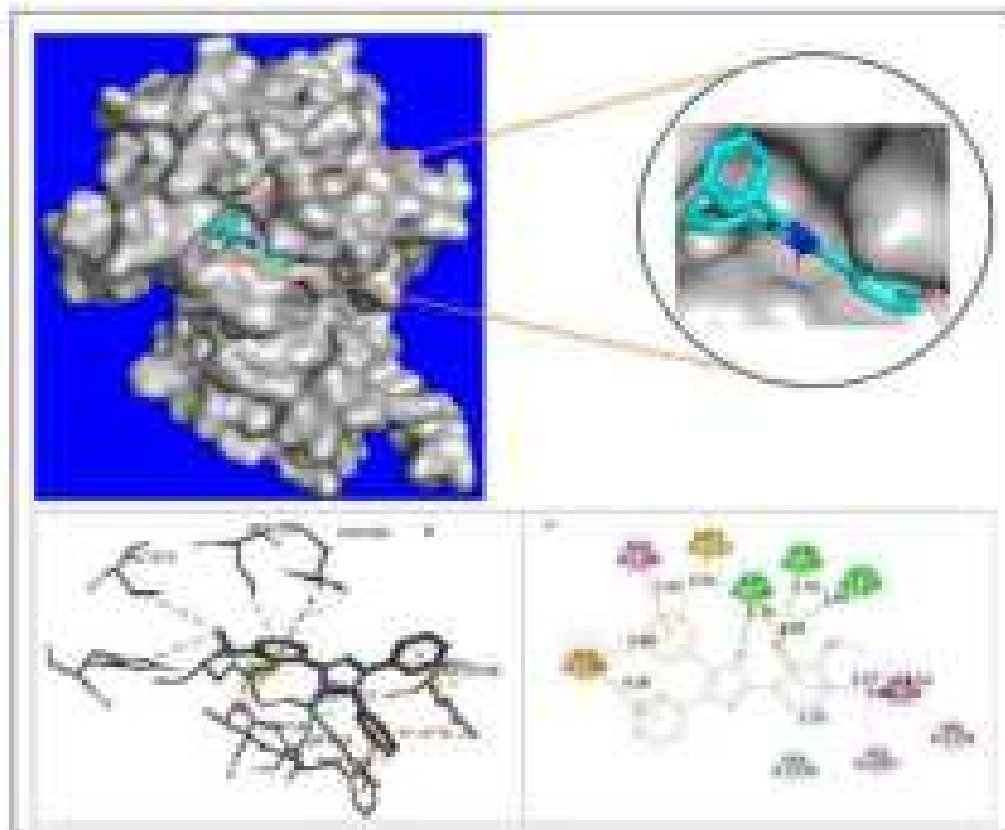


Fig. 3.C.14 Visualisation of docking results of ligand IM-6 with the protein kinase 1IR3: (A) Optimal binding mode of the protein kinase with IM-6 ligand (Ligand TI6 shown as blue and green stick model). (B) Amino acid residues involved in different interactions (green dash lines show H-bonding, light-green lines show π -donor hydrogen bond, yellow lines show π -sulfur interactions, orange lines show π -anion interactions, pink lines show π - π stacked interactions, and light-pink lines show alkyl and π -alkyl interactions). (C) 2D representation of binding interaction of ligand IM-6 with different amino acid residues of the protein 1IR3.

The other type of interactions between ligand IM-6 and protein have been characterized by π -anion (between π electron of 4 and 5-phenyl ring of ligand IM-6 and O atom of COO- group of amino acid residue Glu 1108 at a distance 4.18 Å and 4.89 Å respectively), π -donor hydrogen bond (between π electron of 2-phenyl ring of ligand IM-6 and H atom of OH group of amino acid residue Ser 1270 at a distance 3.26 Å), π -sulfur (between π electron of 5-phenyl ring of ligand IM-6 and S-atom of amino acid residue Met 1112 at a distance 5.81 Å), π - π stacking (between π electron of 2-phenyl ring of ligand IM-6 and π electron of imidazole ring of amino acid residue His1268 at 4.47 Å and π electron of 5-phenyl ring of ligand IM-6 and π electron of phenyl ring of Phe1144 at 5.43 Å respectively) and π -alkyl interaction (between OCH₃ group of 2-phenyl ring of IM-6 and π electron of imidazole ring of amino acid residue His1057 at a distance 4.68 Å). Therefore, it is evident from the docking study that the studied molecules IM-1 to IM-6 could act as a potential inhibitor for the insulin receptor protein IIR3 and the binding affinity of the studied ligands towards the protein IIR3 follows the order IM-5 > IM-3 > IM-1 > IM-2 > IM-4 > IM-6.

3.C.2.3 In silico Pharmacokinetics analysis of IM-1 to IM-6

The pharmacokinetic properties like absorption, distribution, metabolism, excretion and toxicity (ADMET) are fundamental properties in determining the drug likeness of any compounds prior to its clinical and animal studies. Therefore, ADMET property of the studied compounds plays an important role in categorizing them as a drug candidate as well as their activity inside the body⁶¹. The ADMET parameters provide useful information about the concentrations of the drug in the different parts of the body with respect to time⁶². ADMET properties such as gastrointestinal absorption (GI), water soluble capability (Log s), lipophilicity (Log Po/W), CYP1A2 inhibitor and Blood-Brain Barrier (BBB) are fundamentally important for any studied compounds to be considered them as a drug candidate⁶³. Therefore, the pharmacokinetic properties of the selected 2, 4, 5-triarylimidazole derivatives (IM-1 to IM-6) have been computed with the help of computer aided online SwissADME database (<http://www.swissadme.ch>) and the result of the pharmacokinetic properties along with the Lipinski's property are listed in Table 3.C.8.

From the Table 3.C.8 it is evident that all the studied compounds (IM-1 to IM-6) with bioavailability in the range 55 % have lipophilicity value (LogPo/W) in the range 3.48-4.82 and has high gastrointestinal absorption. The high and positive value of lipophilicity (LogPo/w) for the studied compounds indicated that the compounds are more lipophilic and these compounds could easily pass through the lipid bilayer of most cellular membrane. Except compound IM-2 and IM-3, all other compounds have shown promising Blood-Brain Barrier properties and therefore, these compounds could be test for the treatment of disease related to central nervous system as they have BBB crossing ability⁶³. However, the solubility value (LogS) of the studied compounds falls in the range -5.09 to -6.14

and it indicates that the compounds are moderately and poorly soluble in water. Interestingly, all the studied compounds are found to be potential CYP1A2 inhibitors. Thus, the pharmacokinetic parameters suggest that the studied compounds (IM-1 to IM-6) could serve as a potential drug candidate with no violation of Lipinski's rule of five and hence the compounds qualify the criteria of drug likeness.

Table. 3.C.8. Lipinski's properties and pharmacokinetic properties (ADME) of 2, 4, 5-triarylimidazole derivatives (IM-1 to IM-6)

Compounds						
Properties	IM-1	IM-2	IM-3	IM-4	IM-5	IM-6
Molecular weight (gm/mole)	312.36	357.36	391.26	346.81	328.36	342.39
Rotatable bonds	3	4	3	3	3	4
H-bond acceptor	2	4	2	2	3	3
H-bond donor	2	2	2	2	3	2
Violations	0	0	0	0	0	0
Log Po/W	4.26	3.48	4.82	4.73	3.89	4.19
Log S	-5.24(MS)	-5.27(MS)	-6.14(PS)	-5.82(MS)	-5.09(MS)	-5.29(MS)
GI	High	High	High	High	High	High
BBB	Yes	No	No	Yes	Yes	Yes
CYP1A2	Yes	Yes	Yes	Yes	Yes	Yes
Bioavailability Score	0.55	0.55	0.55	0.55	0.55	0.55
Topological Surface Area (A^{o2})	48.91	94.73	48.91	48.91	69.14	58.14

*MS: Moderately soluble, PS: Partially soluble, BBB: Blood-Brain Barrier, CYP: Cytochrome P450, GI: Gastrointestinal absorption

3.C.2.4 Computational details

3.C.2.4.1 DFT study

All Quantum Mechanical calculations were carried out on a hp-Z640 desktop P.C. with an Intel Xeon processor (Specifications: E5-2630 V4 @ 220GHz) using Gaussian 16 W package. Density functional theory (DFT) with Becke's (B) three parameter hybrid model, Lee, Yang and Parr's (LYP) using 6-31 G +(d,2p) basis set has been employed to optimize the geometry of the 2, 4, 5-triarylimidazole derivatives (IM-1 to IM-6).

A set of theoretical calculations of selected compounds (IM-1 to IM-6) were performed with Gaussian 16W, Revision A.03 programme package using B3LYP/6-31 G +(d,2p) basis sets to optimize geometry and minimize energy for faster and accurate calculations. With the optimized geometry, theoretical Raman and IR spectra were also calculated from the so chosen basis set. From the optimized geometry, the energy of HOMO and LUMO molecular orbitals along with the energy of HOMO-LUMO gap has also been measured. For analyzing the results of the theoretical calculations, a visual representation was obtained by Gauss View program 6 and it has been used to construct the molecular electrostatic potential surface (MESP) as well as the shape of HOMO and LUMO molecular orbitals. Also, the nonlinear Optical property (NLO) of the selected 2, 4, 5-triarylimidazole have also been calculated taking urea as a reference NLO material.

3.C.2.4.2 Preparation of Protein and ligand for docking Study

The X-ray crystallographic structures of phosphorylated insulin receptor tyrosine kinase protein (PDB ID 1IR3) has been downloaded from the Protein Data Bank (PDB) (<http://www.pdb.org>) database. Graphical User Interface program "Auto Dock Tools (ADT) 1.5.6" from Molecular Graphics Laboratory (MGL) developed by Scripps Research Institute has been used for the preparation of protein for docking study⁶⁰. Input file of receptor protein for the blind docking study were created by taking specific chain (Chain A) of the protein (1IR3). In a typical receptor protein preparation, water molecules and hetero atoms along with the co-crystallised ligands in PDB crystal structure was removed and subsequently, the receptor. pdbqt file has been prepared by adding polar hydrogen atoms and Kollman united atom charges⁵²⁻⁵³. The three-dimensional (3D) structures of ligands (IM-1 to IM-6) were drawn using Chems sketch (ACD/Structure Elucidator, version 12.01, Advanced Chemistry Development, Inc., Toronto, Canada, 2014, <http://www.acdlabs.com>) and geometry optimization of the ligands (IM-1 to IM-6) were carried out using MM2 program incorporated in Chem. Draw Ultra 8.0 and further optimization of geometry of each molecule were carried out with the MOPAC 6 package using the semi-empirical AM1 Hamiltonian⁶⁴. The input .pdbqt file of the ligands was generated using Auto Dock Tools (ADT). As the ligand molecules (IM-1 to IM-6) were non peptides, therefore, Gasteiger charge was assigned and then non-polar hydrogen was merged.

3.C.2.4.3 Molecular docking study using Autodock vina

All molecular docking calculations of the studied ligands (IM-1 to IM-6) with protein IIR3 were carried out in the AutoDock Vina programme 1.1.2 developed by Scripps Research institute^{65,66} and the results of the docking study and the intermolecular interactions between receptors protein and the ligand molecules were analyzed using BIOVIA Discovery Studio 2020 (DS), version 20.1.0.0 (Dassault Systèmes BIOVIA, Discovery Studio Modeling Environment, Release 2017, San Diego: Dassault Systèmes, 2016) and Edu pymol version 1.7.4.4⁶⁶. The three-dimensional (3D) affinity (grid) maps and electrostatic a grid boxes of 80×80×80 Å grid points and grid centre (X, Y, Z) of -24.099, 39.015, 11.431 with a spacing of 1.00 Å generated by AutoGrid auxiliary program for each of the receptor protein for blind docking were generated to cover the entire active site of the receptor protein in order to eliminate biasness arising during the docking simulation⁶⁷. Lamarckian genetic algorithm and a standard protocol with default setting of other run parameters were used for docking simulation. For each docking experiments, several runs were performed by the program with one predicted binding mode with each run. All the torsions were allowed to rotate. The predicted inhibitory constant (**pK_i**) has been calculated using the following standardized equation.⁶⁸

$$pK_i = 10^{\frac{\text{Binding Energy Score}}{1.336}}$$

3.C.2.4.4 Pharmacokinetic study

The pharmacokinetic properties like like absorption, distribution, metabolism, excretion and toxicity (ADMET) of the compounds (IM-1 to IM-6) have been studied using the computer aided online SwissADME database (<http://www.swissadme.ch>).

3.C.3 References

- (1) M. Waheed, N. Ahmed, M. A. Alsharif, M. I. Alahmdi, S. Mukhtar., *ChemistrySelect*, **2017**, 2 (26), 7946–7950.
- (2) T. S. Rajasekar, P. Navamani, K. Jayamoorthy, N. Srinivasan., *Journal of Inorganic and Organometallic Polymers and Materials*, **2017**, 27 (4), 962–967.
- (3) S. Chauhan, V. Verma, D. Kumar, A. Kumar., *Synthetic Communications*, **2019**, 49 (11), 1427–1435.
- (4) A. Z. al Munsur, H. N. Roy, M. K. Imon., *Arabian Journal of Chemistry*, **2020**, 13 (12), 8807–8814.
- (5) S. H. Gebre., *Synthetic Communications*, **2021**, 51 (11), 1669–1699.
- (6) M. A. Zayed, M. A. Abdallah., *Egyptian Journal of Chemistry*, **2019**, 62 (11), 2143–2162.
- (7) D. Gustinčić, A. Kokalj., *Physical Chemistry Chemical Physics*, **2015**, 17 (43), 28602–28615.
- (8) A. P. Kulkarni, C. J. Tonzola, A. Babel, S. A. Jenekhe., *Chemistry of Materials*, **2004**, 16 (23), 4556–4573.
- (9) L. Fabbrizzi, F. Foti, S. Patroni, P. Pallavicini, A. Taglietti., *Angewandte Chemie International Edition*, **2004**, 43 (38), 5073–5077.
- (10) Z. Li, X. Lou, H. Yu, Z. Li, J. Qin., *Macromolecules*, **2008**, 41 (20), 7433–7439.
- (11) Z. Song, W. Zhang, M. Jiang, H. H. Y. Sung, R. T. K. Kwok, H. Nie, I. D. Williams, B. Liu, B. Z. Tang., *Advanced Functional Materials*, **2016**, 26 (6), 824–832.
- (12) S. Suresh, N. Bhuvanesh, A. Raman, P. Sugumar, D. Padmanabhan, S. Easwaramoorthi, M. N. Ponnuswamy, S. Kavitha, R. Nandhakumar., *Journal of Photochemistry and Photobiology A: Chemistry*, **2019**, 385, 112092.
- (13) Y. H. Lam, Y. Abramov, R. S. Ananthula, J. M. Elward, L. R. Hilden, S. O. Nilsson Lill, P. O. Norrby, A. Ramirez, E. C. Sherer, J. Mustakis, G. J. Tanoury., *Organic Process Research and Development*, **2020**, 24 (8), 1496–1507.
- (14) M. Evecen, H. Tanak., *Materials Science- Poland*, **2016**, 34 (4), 886–904.
- (15) S. Gümüş, L. Türker., *Heterocyclic Communications*, **2012**, 18 (1), 11–16.
- (16) P. Lienard, J. Gavartin, G. Boccardi, M. Meunier., *Pharmaceutical Research*, **2015**, 32 (1), 300–310.

- (17) H. J. Huang, H. W. Yu, C. Y. Chen, C. H. Hsu, H. Y. Chen, K. J. Lee, F. J. Tsai, C. Y. C. Chen., *J Taiwan Inst Chem Eng*, **2010**, *41* (6), 623–635.
- (18) D. Giugliano, A. Ceriello, K. Esposito., *The American Journal of Clinical Nutrition*, **2008**, *87* (1), 217S-222S.
- (19) G. S. Mohiuddin, S. Palaian, P. R. Shankar, K. G. Sam, M. Kumar., *International Journal of Pharmaceutical Sciences and Research*, **2019**, *10* (9), 4145–4148.
- (20) J. Ganugapati, A. Baldwa, S. Lalani., *Bioinformation*, **2012**, *8* (5), 220.
- (21) N. Satheesha Rai, B. Kalluraya, B. Lingappa, S. Shenoy, V. G. Puranic., *European Journal of Medicinal Chemistry*, **2008**, *43* (8), 1715–1720.
- (22) A. D. Becke., *The Journal of Chemical Physics*, **1993**, *98* (7), 5652.
- (23) C. Lee, W. Yang, R. G. Parr., *Physical Review B*, **1988**, *37* (2), 789.
- (24) M. J. Frisch, G. W. Trucks, H. B. Schlegel, G. E. Scuseria, M. A. Robb, J. R. Cheeseman, G. Scalmani, V. Barone, G. A. Petersson, H. Nakatsuji, X. Li, M. Caricato, A. v Marenich, J. Bloino, B. G. Janesko, R. Gomperts, B. Mennucci, H. P. Hratchian, J. v Ortiz, A. F. Izmaylov, J. L. Sonnenberg, D. Williams-Young, F. Ding, F. Lipparini, F. Egidi, J. Goings, B. Peng, A. Petrone, T. Henderson, D. Ranasinghe, V. G. Zakrzewski, J. Gao, N. Rega, G. Zheng, W. Liang, M. Hada, M. Ehara, K. Toyota, R. Fukuda, J. Hasegawa, M. Ishida, T. Nakajima, Y. Honda, O. Kitao, H. Nakai, T. Vreven, K. Throssell, J. A. Montgomery Jr., J. E. Peralta, F. Ogliaro, M. J. Bearpark, J. J. Heyd, E. N. Brothers, K. N. Kudin, V. N. Staroverov, T. A. Keith, R. Kobayashi, J. Normand, K. Raghavachari, A. P. Rendell, J. C. Burant, S. S. Iyengar, J. Tomasi, M. Cossi, J. M. Millam, M. Klene, C. Adamo, R. Cammi, J. W. Ochterski, R. L. Martin, K. Morokuma, O. Farkas, J. B. Foresman, D. J. Fox., *Gaussian, Inc., Wallingford CT, Gaussian 16 Revision C.01*, **2016**.
- (25) R. Dennington, T. A. Keith, J. M. Millam., *GaussView Version 6, Semichem Inc., Shawnee Mission, KS*, **2016**.
- (26) G. Varvounis, V. Gkalpinos, P. Theodorakopoulou, E. Tsemperlidou., In *Comprehensive Heterocyclic Chemistry IV (Chap 4.02 - Imidazoles)*; Black, D. S., Cossy, J., Stevens, C. V., Eds.; Elsevier: Oxford, **2022**; Vol. 4, pp 113–307.
- (27) P. Sykes., *A Guidebook to Mechanism in Organic Chemistry*, 6th ed.; Pearson Education: New Delhi, India, **2004**.
- (28) M. Belletête, J. F. Morin, M. Leclerc, G. Durocher., *Journal of Physical Chemistry A*, **2005**, *109* (31), 6953–6959.
- (29) D. Zhenming, S. Heping, L. Yufang, L. Diansheng, L. Bo., *Spectrochimica Acta Part A: Molecular and Biomolecular Spectroscopy*, **2011**, *78* (3), 1143–1148.

- (30) K. B. Benzon, H. T. Varghese, C. Y. Panicker, K. Pradhan, B. K. Tiwary, A. K. Nanda, C. van Alsenoy., *Spectrochimica Acta Part A: Molecular and Biomolecular Spectroscopy*, **2015**, *151*, 965–979.
- (31) S. W. Xia, X. Xu, Y.-L. Sun, Y.-H. Fan, C.-F. Bi, D. M. Zhang, L.-R. Yang., *Chinese Journal of Structural Chemistry*, **2006**, *25* (2), 197–203.
- (32) M. Snehalatha, C. Ravikumar, I. Hubert Joe, N. Sekar, V. S. Jayakumar., *Spectrochimica Acta Part A: Molecular and Biomolecular Spectroscopy*, **2009**, *72* (3), 654–662.
- (33) T. A. Koopmans., *Physica*, **1934**, *1* (1–6), 104–113.
- (34) R. G. Parr, R. G. Pearson., *J Am Chem Soc*, **1983**, *105* (26), 7512–7516.
- (35) R. G. Parr, L. V. Szentpály, S. Liu., *J Am Chem Soc*, **1999**, *121* (9), 1922–1924.
- (36) R. G. Pearson., *Journal of Chemical Sciences*, **2005**, *117* (5), 369–377.
- (37) S. Mandal, D. K. Poria, D. K. Seth, P. S. Ray, P. Gupta., *Polyhedron*, **2014**, *73*, 12–21.
- (38) P. Jaramillo, P. Pérez, R. Contreras, W. Tiznado, P. Fuentealba., *Journal of Physical Chemistry A*, **2006**, *110* (26), 8181–8187.
- (39) N. P. G. Roeges., *A Guide to the Complete Interpretation of Infrared Spectra of Organic Structures*; John Wiley and Sons Inc.: New York, **1994**.
- (40) B. C. Smith., *Infrared Spectral Interpretation*, 1st ed.; CRC Press: Washington, DC, **1999**; Vol. 2.
- (41) P. Politzer, D. G. Truhlar., *Chemical Applications of Atomic and Molecular Electrostatic Potentials*; Plenum Press: New York, **1981**.
- (42) E. Scrocco, J. Tomasi., *Advances in Quantum Chemistry*, **1978**, *11* (C), 115–193.
- (43) P. Politzer, J. S. Murray., In *Theoretical Biochemistry and Molecular Biophysics: A Comprehensive Survey*; Beveridge, D. L., Lavery, R., Eds.; Adenine Press: Schenectady, New York.
- (44) E. Scrocco, J. Tomasi., *Topics in Current Chemistry* , **1973**, *42*, 95–170.
- (45) *Principles and Applications of Nonlinear Optical Materials*, 1st ed.; Munn, R. W., Ironside, C. N., Eds.; Springer Dordrecht: Netherlands, **1993**.
- (46) A. Migalska-Zalas, K. el Korchi, T. Chtouki., *Optical and Quantum Electronics*, **2018**, *50*(11) (Article no. 389), 1–10.

- (47) M. U. Khan, M. Khalid, S. Asim, Momina, R. Hussain, K. Mahmood, J. Iqbal, M. N. Akhtar, A. Hussain, M. Imran, A. Irfan, A. Ali, M. F. ur Rehman, Y. Jiang, C. Lu., *Frontiers in Materials*, **2021**, 8 (Article 719971), 287.
- (48) M. R. S. A. Janjua., *Journal of the Iranian Chemical Society*, **2017**, 14 (9), 2041–2054.
- (49) V. M. Geskin, C. Lambert, J. L. Brédas., *J Am Chem Soc*, **2003**, 125 (50), 15651–15658.
- (50) M. Beytur, F. Kardaş, O. Akyıldırım, A. Özkan, B. Bankoğlu, H. Yüksek, M. L. Yola, N. Atar., *Journal of Molecular Liquids*, **2018**, 251, 212–217.
- (51) S. Muthu, T. Rajamani, M. Karabacak, A. M. Asiri., *Spectrochimica Acta Part A: Molecular and Biomolecular Spectroscopy*, **2014**, 122, 1–14.
- (52) L. G. Ferreira, R. N. dos Santos, G. Oliva, A. D. Andricopulo., *Molecules*, **2015**, 20 (7), 13384–13421.
- (53) X.-Y. Meng, H.-X. Zhang, M. Mezei, M. Cui., *Current Computer-Aided Drug Design*, **2011**, 7 (2), 146–157.
- (54) A. T. Kharroubi, H. M. Darwish., *World J Diabetes*, **2015**, 6 (6), 867.
- (55) A. B. Olokoba, O. A. Obateru, L. B. Olokoba., *Oman Medical Journal*, **2012**, 27 (4), 269–273.
- (56) S. A. Ashraf, A. E. O. Elkhalfa, K. Mehmood, M. Adnan, M. A. Khan, N. E. Eltoun, A. Krishnan, M. S. Baig., *Molecules*, **2021**, 26 (19), 5957.
- (57) R. Chaturvedi, C. Desai, P. Patel, A. Shah, R. K. Dikshit., *Perspectives in Clinical Research*, **2018**, 9 (1), 15–22.
- (58) J. C. Lee, J. T. Laydon, P. C. McDonnell, T. F. Gallagher, S. Kumar, D. Green, D. McNulty, M. J. Blumenthal, J. R. Keys, S. W. Land Vatter, J. E. Strickler, M. M. McLaughlin, I. R. Siemens, S. M. Fisher, G. P. Livi, J. R. White, J. L. Adams, P. R. Young., *Nature*, **1994**, 372 (6508), 739–746.
- (59) K. L. Binns, P. P. Taylor, F. Sicheri, T. Pawson, S. J. Holland., *Molecular and Cellular Biology*, **2000**, 20 (13), 4791–4805.
- (60) R. Huey, G. M. Morris., *Using AutoDock 4 with AutoDocktools: A Tutorial.*; The Scripps Research Institute, Molecular Graphics Laboratory, pp. 54-56: La Jolla, CA, USA, **2008**.
- (61) S. Hari., *Journal of Applied Pharmaceutical Science*, **2019**, 9 (7), 18–26.
- (62) K. Boussery, F. M. Belpaire, J. van de Voorde., In *The Practice of Medicinal Chemistry*; Wermuth, C. G., Ed.; Elsevier Science, **2008**; pp 635–654.

- (63) F. Ntie-Kang, L. L. Lifongo, J. A. Mbah, L. C. Owono Owono, E. Megnassan, L. M. Mbaze, P. N. Judson, W. Sippl, S. M. N. Efange., *In Silico Pharmacology*, **2013**, *1(1)* (Article 12), 1–11.
- (64) K. Ohtawara, H. Teramae., *Chemical Physics Letters*, **2004**, *390* (1–3), 84–88.
- (65) J. Eberhardt, D. Santos-Martins, A. F. Tillack, S. Forli., *Journal of Chemical Information and Modeling*, **2021**, *61* (8), 3891–3898.
- (66) O. Trott, A. J. Olson., *Journal of Computational Chemistry*, **2010**, *31* (2), 455–461.
- (67) G. M. Morris, D. S. Goodsell, R. S. Halliday, R. Huey, W. E. Hart, R. K. Belew, A. J. Olson., *Journal of Computational Chemistry*, **1998**, *19* (14), 1639–1662.